OPTOFLUIDIC RING RESONATOR: A VERSATILE MICROFLUIDIC PLATFORM FOR CHEMICAL VAPOR DETECTION AND INTRA-CAVITY BIOMOLECULAR ANALYSIS

by

Yuze Sun

A dissertation submitted in partial fulfillment
of the requirements for the degree of
Doctor of Philosophy
(Biomedical Engineering)
in The University of Michigan
2011

Doctoral Committee:

Associate Professor Xudong Fan, Chair
Professor L. Jay Guo
Professor Shuichi Takayama
Associate Professor Cheri X. Deng
Associate Professor Jinsang Kim

To Mom and Dad

Acknowledgements

First and foremost, I would like to express my deepest gratitude to my advisor, Professor Xudong (Sherman) Fan, for his guidance, inspiration, trust, and support throughout my Ph.D. study. His insights and expert advice are crucial to the success in the many projects I worked on. I have been benefited tremendously from his intelligence, creativity, and rigorous approach to science. His enthusiasm in and dedication to research will always inspire me to expect more from myself.

I would also like to thank other members of my doctoral committee: Professor Cheri X. Deng, Professor L. Jay Guo, Professor Jinsang Kim, and Professor Shuichi Takayama, for their useful comments and suggestions for the work included in this thesis.

The work on chemical vapor sensing described herein could never have been possible without the support and fruitful discussion with my collaborators, Dr. Greg Frye-Mason, Dr. Shiou-jyh Ja, and Aaron Thompson, at FLIR. Additionally, I am grateful to Professor Stephen Arnold at the Polytechnic Institute of New York University for his help on the study of energy transfer in the OFRR microlaser and his impressive understanding in physics. I am also indebted to Dr. Misha Sumetsky, who supervised my research and shared many stimulating ideas on ring resonator when I was at OFS Laboratories.

I thank my fellow group members who offered help, time, and friendship over the years in the Fan lab: Dr. Ian White, Dr. Siyka Shopova, Hongying Zhu, Jonathan Suter, Jay Cupps, Chung-Shieh Wu, John Gohring, Daniel Howard, Dr. Gilmo Yang, Dr. Xiang

Wu, Dr. Xiaoyun Pu, Luxing Wang, Dr. Yunbo Guo, Dr. Maung Kyaw Khaing Oo, Dr. Yunhan Luo, Dr. Xiangwei Zhao, Hao Li, Karthik Reddy, Jing Liu, Wonsuk Lee, and Chia-Fang Chang. I am especially indebted to Dr. Ian White for his mentorship when I joined the Fan lab. I am fortunate enough to learn experimental skills and the attitude towards research from him, and to observe closely his management skills and leadership in lab. I also appreciate his long-list of advice on my career planning. I further thank Siyka and Jon for their discussion on microfluidic lasers, Chung-Shieh for his help on quantum dots and FRET measurement, and Hongying for her generous help in the lab.

I cannot imagine my life without my closest friends. I thank Zhenzhen Fan and Peter Tai in making Ann Arbor more like home, Hongying and Shaohui for their help and care in Columbia, Xiaoling Su and Zhangshuang Deng for their encouragement that always comes at the right time, Chuanfu Zhang for his sharp views on many aspects of life, and Jianjun Chen for his sincere help to my research work.

Finally, I am most grateful to my beloved parents. I cannot fully express my gratitude to them for the lifelong unconditional love and support every step of the way.

Table of Contents

List of Figures

List of Tables

ABSTRACT

Optofluidic Ring Resonator: a Versatile Microfluidic Platform for Chemical Vapor Detection and Intra-Cavity Biomolecular Analysis

by

Yuze Sun

Chair: Xudong Fan

Starting from initial idealization in 1995 and subsequent ground-breaking work in early 2000s, the optical ring resonator has quickly emerged in the past few years as a new sensing technology that has a wide range of applications in healthcare, biomedical research, homeland security, and environmental monitoring to detect target analytes in either liquid or vapor phase rapidly and sensitively.

The optical ring resonator sensor relies on the whispering gallery mode (WGM) to carry out the sensing. The WGM forms due to total internal reflection of light at the curved ring resonator surface. It circulates along the ring resonator and repetitively interacts with the analyte near the ring resonator surface. Due to the extremely high Q-

factor (>10^6), the effective interaction length between the WGM and the analyte can be as long as a few tens of centimeters, despite small physical size of the ring resonator (a few tens of micrometers in diameter). Therefore, highly sensitive detection can be achieved.

Although a number of optical ring resonator configurations have been explored, there is still a great need for a synergistic configuration that integrates optical and fluidic components. To meet this challenge, the optofluidic ring resonator (OFRR) is developed in this thesis. The OFRR is a thin-walled glass capillary whose circular cross section forms the ring resonator with an ultra-high Q-factor (>10^7). It naturally integrates the highly sensitive ring resonator sensing technology and the superior fluidic handling capability of the capillary. The WGM circulating along the OFRR wall interacts with the analyte near the inner surface of the capillary, thus providing quantitative and temporal information of the analyte flowing through the capillary. Based on this versatile optofluidic platform, chemical vapor detection and microfluidic laser intra-cavity biodetection are extensively investigated in the thesis.

In the chemical vapor detection, the OFRR gas sensing platform is built by coating a vapor sensitive polymer layer on the OFRR capillary inner surface. The polymer-vapor interaction results in a change in the polymer thickness and refractive index, which in turn causes a spectral shift in the WGM that has the electric field present in the polymer layer. To improve the gas sensing specificity, the OFRR sensing technique is further integrated with micro-gas chromatography (μGC) separation technology, and the OFRR-based μGC system is thus developed. The dual use of the OFRR capillary as a separation column and an optical detector renders the OFRR-based μGC system unique multi-point on-column detection capability. In this thesis, the OFRR vapor sensing

feasibility is first demonstrated with detection of representative gas analytes, followed by the theoretical analysis using a four-layer Mie model, which provides guidelines to the sensor design. Then, experimental studies are carried out on the OFRR-μGC system, where rapid and sensitive detection of dinitrotoluene vapor out of interfering background at room temperature is demonstrated. Finally, a tandem-column setting of the OFRR-μGC system is investigated to enhance the chromatographic resolution. A vapor mixture of twelve analytes of different volatilities and polarities are separated and detected within four minutes.

In the microfluidic laser intra-cavity biodetection, the OFRR platform is studied for active biosensing. In this thesis, a bio-compatible optofluidic laser is developed based on the OFRR. DNA scaffolds are incorporated into the laser gain medium and control the lasing emission properties through efficient fluorescence resonant energy transfer. This platform is further used to explore highly selective intra-cavity DNA detection. Two orders of magnitude improvement in detection selectivity is achieved over the conventional fluorescence detection method in differentiating the target and the single-base mismatched DNA sequences.

Chapter 1

Introduction

1.1 Motivation of developing an optofluidic ring resonator platform

Starting from initial idealization and subsequent ground-breaking work [1-3], the optical ring resonator has quickly emerged in the past few years as a new sensing technology. There are over 300 papers published in the last decade that are related to ring resonator bio/chemical sensing, most of which are from the recent 5 years [4]. Intensive research in this field is motivated by broad applications of ring resonator sensors in healthcare, environmental monitoring, homeland security, food industry, and pharmaceuticals, which require sensitive and rapid analytical tools. Meanwhile, due to the circulating nature of the light guided by the optical ring resonator, it has long been an interesting and convenient platform to study nonlinear optical processes, such as lasing [5-11]. In recent years, research on developing optofluidic lasers has drawn significant attention in the optical community [12-19]. Optofluidic lasers are the realization of old-time dye lasers with microfluidics and microscale optics. The successful development of optofluidic lasers will not only facilitate the implementation of complete "Micro-Total Analysis Systems" (μTAS), but also enable the dynamic control of laser properties through liquid manipulation.

In both ring resonator sensor and optofluidic laser applications, two most important features that a device must have are a high quality factor (Q-factor) cavity and

efficient microfluidics. The high Q-factor results in a low limit of detection (LOD) in optical ring resonator sensors and a low lasing threshold in optofluidic lasers. Efficient microfluidics is the key to many practical aspects of an optofluidic device, such as efficient and controlled sample delivery, reduced sample consumption volume, reduced flow dead volume, fast sensor response, and compact device design. Although a number of high-Q optical ring resonator configurations have been explored, there is still a great need for a synergistic configuration that integrates optical and fluidic components [20, 21]. To address the challenge, in this thesis we will develop a new ring resonator platform named optofluidic ring resonator (OFRR), which is an integration of a high Q-factor micro-cavity and a glass capillary with inherently efficient microfluidics. Based on the OFRR platform, we will investigate chemical vapor detection and microfluidic laser intra-cavity biodetection, respectively.

1.2 Roadmap to this Thesis

The flow of this thesis is as follows. In Chapter 2, the development, fabrication, and characterization of the OFRR are presented. This chapter further shows the OFRR is a powerful and versatile microfluidic platform, which can be developed into gas sensors and microfluidic dye lasers, respectively. The refractive index (RI) sensing principle and lasing principle are explained accordingly. Chapter 3 and Chapter 4 focus on the study of the OFRR in gas sensing applications, where the OFRR is operated as a passive optical microcavity. Chapter 3 begins by describing the OFRR gas sensing principle, followed by experimental demonstration of static gas detection and theoretical study of the OFRR gas sensing performance. In Chapter 4, to improve gas sensing selectivity, the integration of

OFRR sensing technology and micro-gas chromatography (μGC) is discussed. An OFRR-based micro-GC system is proposed and studied. Tandem-column OFRR micro-GC is also investigated to improve the chromatographic resolution. Chapter 5 and Chapter 6 are dedicated to the study of the OFRR as an active optical microcavity. Chapter 5 covers the work performed on the development of a biocompatible microfluidic laser based on the OFRR. In Chapter 6, the biocompatible OFRR microlaser is used for highly selective intra-cavity DNA detection. The thesis is concluded in Chapter 7 with a brief summary and outlook towards future research directions.

Chapter 2

Optofluidic Ring Resonator

2.1 Overview of optical ring resonators

The optical ring resonator sensor relies on the light-analyte interaction to convert the presence of chemical or biological analytes into a quantitatively measurable optical signal. As illustrated in Fig 2.1, an optical ring resonator can be regarded as a ring-shaped waveguide. Due to total internal reflection of light at the curved boundary, a resonant optical mode called whispering gallery mode (WGM) forms. The resonant wavelength, λ, is given by:

$$\lambda = 2\pi r n_{eff} / m , \tag{2.1}$$

where r is the resonator radius, n_{eff} is the effective RI experienced by the optical resonant mode, and m is an integer number. The resonant light circulates along the ring resonator and has the evanescent field several hundred nanometers into the surrounding medium (*e.g.*, liquid, gas, and polymer coatings) to interact repetitively with the analytes near the resonator surface. Likewise, in the ring resonator based optofluidic lasers, the lasing properties are also determined by light-analyte interaction, in which case, the analyte becomes dye molecules or other gain materials.

As a new sensing/lasing technology, the ring resonator has a number of distinctive advantages. In contrast to the traditional linear waveguide or fiber based sensor/laser

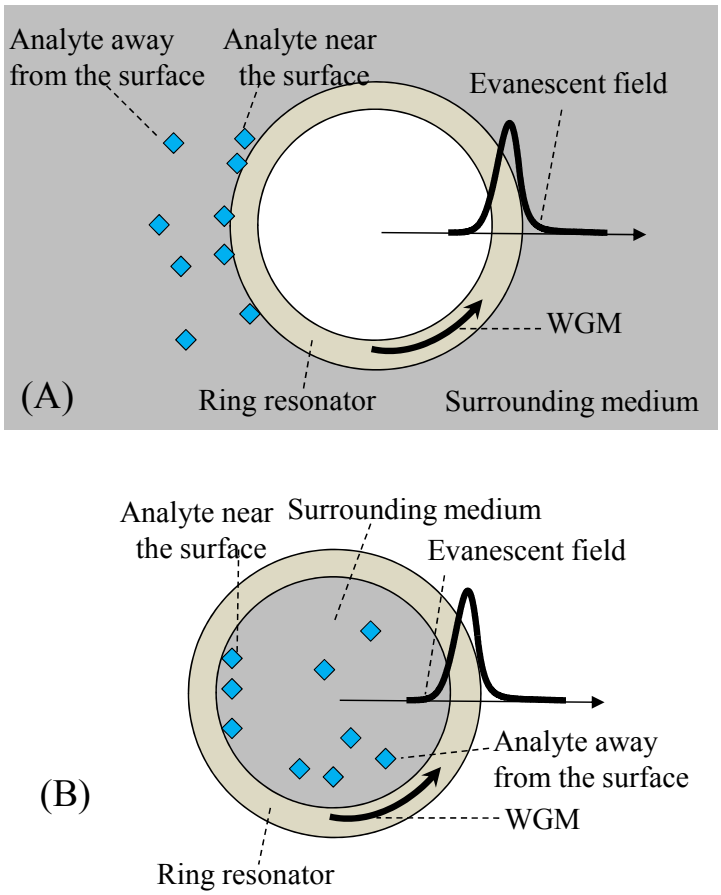

Fig. 2.1 Conceptual illustrations of an optical ring resonator sensor. The resonant light circulates along the resonator and its evanescent field is present in the surrounding medium outside (A) or inside (B) the ring resonator, interacting with the analyte on the resonator exterior surface (A) or interior surface (B), as well as in the surrounding medium. Reprinted from Ref. [4] with permission.

where the light-analyte interaction length is essentially the physical length of the device, the circulating nature of the resonant mode creates extremely long effective interaction length, which is determined by $L_{eff} = Q\lambda/(2\pi n)$, where Q is the resonator quality factor, representing the number of round trips that the resonant light can circulate along the ring resonator. Depending on the ring resonator configurations, as described later, the Q-factor usually ranges from 10^4 to 10^8. Therefore, despite small physical size, the ring resonator has an effective interaction length of a few tens of centimeters or even longer, which

renders the ring resonator better sensing performance, smaller footprint, and higher multiplexing capability while using less amount of analyte. Another benefit that the ring resonator offers is the significantly enhanced light intensity near its surface with the enhancement being proportional to the Q-factor, which is due once again to the circulating nature of the resonant light. This phenomenon can also be exploited for sensing applications.

After nearly 10 years of investigation, a variety of chemical and biological species have been detected using ring resonators, including DNA, protein, virus, nanoparticle, bacterium, heavy metal, pesticide, volatile organic compounds (VOCs) in liquid or gaseous phase [2, 22-40]. Different types of ring resonators have been designed to carry out those detections. As illustrated in Fig 2.2, optical ring resonator sensors have been implemented in a number of configurations. These configurations are also being explored in the development of optofluidic lasers.

(1) Microspheres made of liquid [10, 40-44], fused silica [2, 23, 45-49], and polymers [50-54]. They are cost-effective and easy to fabricate. The fused silica based microsphere and liquid based microsphere (also known as microdroplet) have extremely high Q-factors. A Q-factor over 10^9 has been reported when the fused silica microsphere is in air [45]. When immersed in water, the silica microsphere has a Q-factor in excess of 10^7 [48, 49], which results in a high spectral resolution and hence a low LOD for sensing. Microdroplets offer the best surface quality of any ring resonators available, resulting in negligible surface scattering induced loss. Consequently, the Q-factor of a microdroplet is usually as high as 10^8, mainly determined by the optical absorption of the solvent. Despite being a good platform for the purpose of rapid proof-of-concept and basic

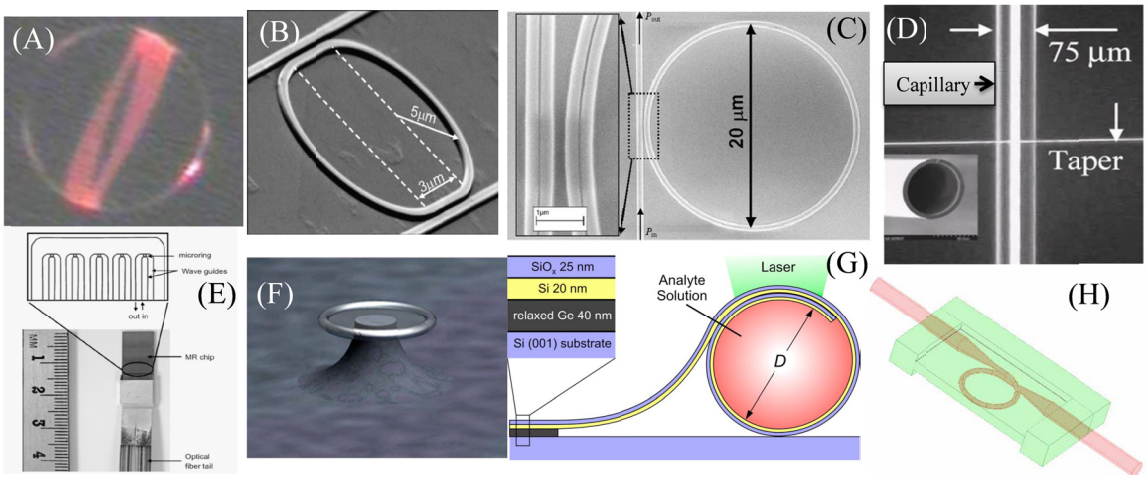

Fig. 2.2 Various ring resonator configurations. (A) Microsphere. (B) Silicon-on-insulator planar ring resonator. (C) Slot waveguide ring resonator. (D) Capillary based ring resonator fabricated by the drawing method. (E) Planar ring resonator array. (F) Microtoroid. (G) Capillary based ring resonator fabricated by the rolled-up method. (H) Microfiber coil based ring resonator. Reprinted from Ref. [4] with permission.

research, it is challenging to mass produce and integrate microspheres into an array format for most practical applications. The integration with microfluidics for efficient sample delivery continues to be very difficult. Additionally, the polymer based ring resonator suffers from relatively low Q-factor, which may limit their sensing performance.

(2) Ring, disk, or toroid-shaped resonators fabricated with dielectric materials (such as silicon-on-insulator and polymers) on a silicon wafer [22, 24, 33, 34, 37, 54-64]. They can be mass-produced using micro/nanofabrication technologies and scaled up to an array format for multiplexed detection. One challenging task for this kind of on-chip ring resonator sensors/lasers is the fluidic integration. Often, the solution to this requires building a fluidic channel or flow chamber on top of the ring resonator and controlling the sample flow via a peristaltic pump [56, 65]. Usually, these on-chip ring resonators suffer from low Q-factors, with the best Q-factor around 10^5, except the microtoroid ring

resonator, which undergoes the laser reflow process during the fabrication to a smooth surface and hence a high Q-factor up to 10^8.

(3) Capillary based ring resonators [66-73]. The resonators are naturally integrated with capillary based microfluidics for convenient sample delivery. Besides the OFRR (Fig. 2(D)) that will be discussed in detail later, there is another capillary based ring resonator design that uses microtubes composed of rolled up semiconductor materials (Fig. 2(G)) [68-74]. While these tubes are much better suited for on-chip integration, their performance is limited by its low Q-factor, which is usually lower than 10^3 [68].

(4) Micro/nano fiber coil based ring resonators [75-86]. They take advantage of convenience in optical fiber coupling and support moderately good Q-factors (on the order of 10^5) at diameters below 200 μm [84], even down to 15 μm [76]. However, they are delicate and difficult to handle. Mass production and integration of micro/nanofiber ring resonators into a device have yet to be demonstrated.

2.2 Optofluidic ring resonator

2.2.1 Configuration

The OFRR platform is illustrated in Fig. 2.3. The OFRR is a micro-sized fused-silica glass capillary that acts simultaneously as a microfluidic channel for sample delivery and as a ring resonator for sample detection (sensor) or provide optical feedback (laser). The diameter of the capillary is typically around 100 μm. The ring resonator is formed in the circular cross section of the capillary, where WGMs are guided through

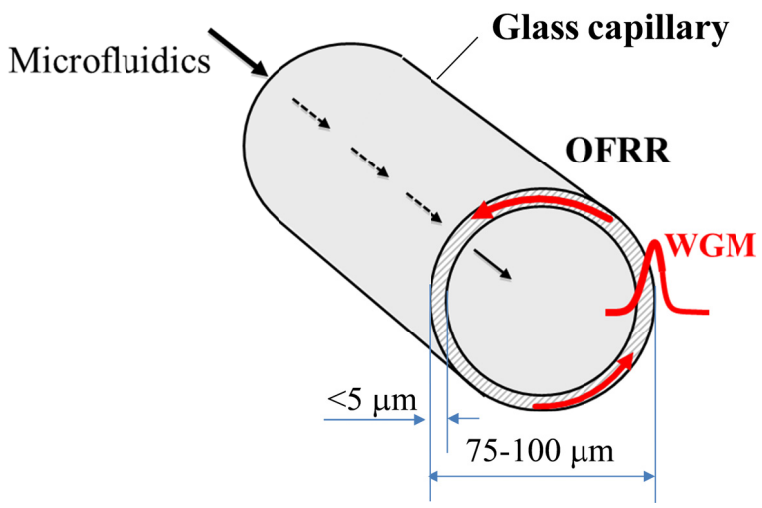

Fig. 2.3 Schematic illustration of the OFRR platform.

total internal reflection by the capillary inner and outer surface. What makes OFRR special as compared to other glass capillaries is that its wall thickness is sufficiently thin (*i.e.*, <5 μm) so that WGM has an evanescent field that extends beyond both inner and outer wall (see Fig. 2.1(B)). The WGM evanescent field near the inner surface is repeatedly interacting with the liquid/gas analyte that flows through the OFRR capillary. When OFRR is used as a gas sensor, the presence of the gas molecules in the optical field changes the effective RI experienced by the WGM. According to Eq. (2.1), this causes the resonant wavelength to shift spectrally. The WGM spectral shift over time as the gas sample passes through the OFRR capillary is the sensor signal. Therefore, by monitoring the WGM shift, both kinetic and quantitative information on the analyte can be acquired. In case of the optofluidic laser, the gain medium (*i.e.*, organic dye solution) is flowed into the OFRR capillary and evanescently interacts with the WGM that provides optical feedback.

2.2.2 Fabrication

Since the thin-walled glass capillary is not commercially available, we have assembled a computer-controlled pulling station in our lab (Fig. 2.4(A)) capable of fabricating an OFRR up to 50 centimeters in length by rapidly stretching a fused silica pre-form under CO_2 laser irradiation. Specifically, two CO_2 lasers (25 W, Synrad, Inc.) are used on opposite sides to provide more evenly distributed heating. Two ends of the capillary pre-form are mounted on the feed-in and pulling stage, respectively. Under CO_2

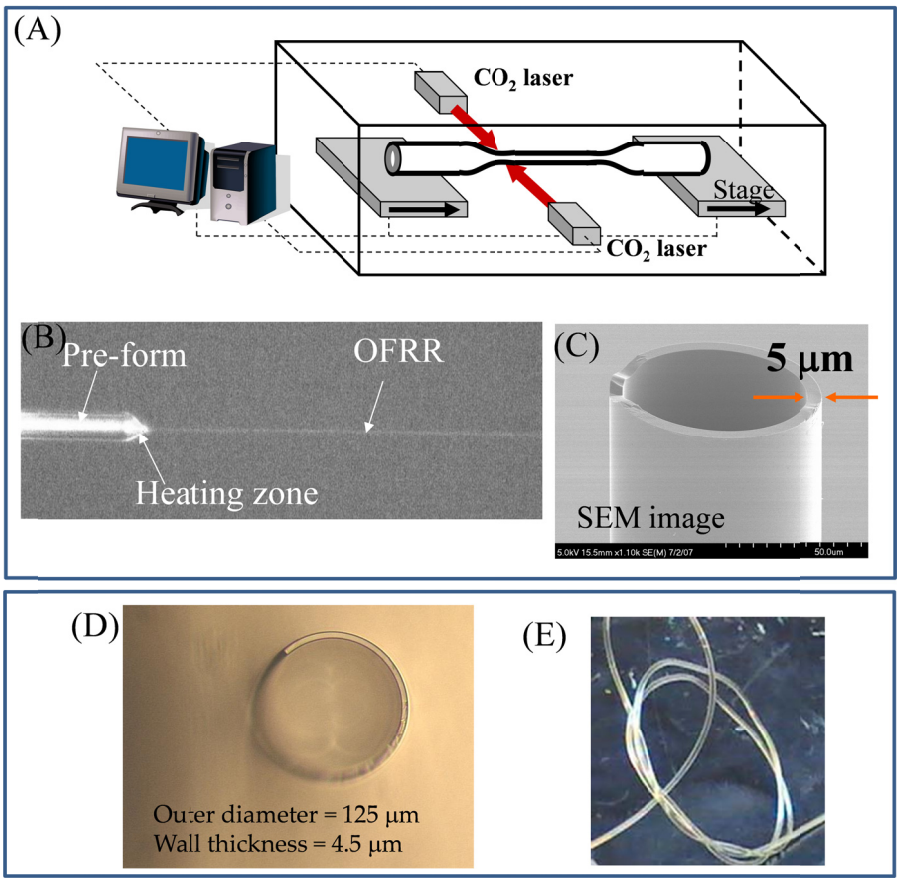

Fig. 2.4 (A) OFRR fabrication setup. (B) Microscope image of an OFRR made from a capillary pre-form. (C) SEM image of an OFRR. (D) Cross section image of tens of meters of OFRR made at OFS using a commercial optical fiber draw tower. (E) The OFRR made at OFS. Polymer coating outside of the OFRR capillary adds flexibility and mechanical strength.

laser irradiation, the pulling stage is moved quickly away from the heating zone while the feed-in stage is slowly pushed toward the heating zone, keeping constant mass of glass in the heating zone. The laser power and stage moving speed can be adjusted in computer codes developed using LabView software (National Instruments). The whole apparatus is enclosed in an acrylic box to reduce the air fluctuation to the laser heating zone on the capillary during pulling. Fig. 2.4(B) shows a microscope image of an OFRR capillary being drawn from a glass capillary pre-form.

As the OFRR wall thickness is critical to its optical properties, attention must be given to the temperature and pulling speed, as these parameters determine the final diameter and wall thickness after pulling. Therefore, the optimized CO_2 power, feed-in speed, and pulling speed are obtained by error and trial for different pre-forms. With different geometries of capillary pre-forms, we can fabricate OFRR in a variety of sizes (outer diameter (OD) in the range of 50-150 μm). After direct pulling using this setup, a typical 100 μm OD OFRR has a wall thickness of 5 μm, as verified by SEM characterization in Fig. 2.4(C).

The OFRR can also be fabricated using an industrial fiber draw tower for mass production, similar to the way in which commercial optical fiber cable is fabricated. Currently this method is being explored through the collaboration with OFS Laboratories (Somerset, NJ). With OFS facilities, the OFRRs of kilometers can be fabricated. Fig. 2.4(D) shows the cross-sectional view of an OFRR fabricated by the fiber draw tower, which has an OD of 125 μm with the wall thickness of 4.5 μm. During the drawing process, OFRR is simultaneously coated with polymer for mechanical protection. Therefore, the OFRR is flexible and easy to handle (see Fig. 2.4(E)).

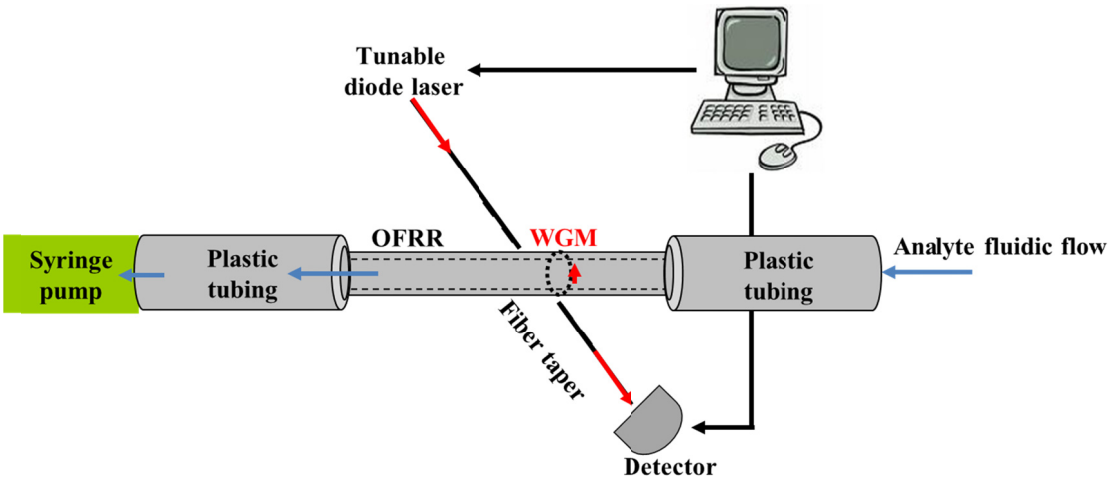

Fig. 2.5 The experimental setup for OFRR characterization.

2.2.3 Characterization

2.2.3.1 Creating characterization setup

In order to characterize the OFRR, we assemble the experimental setup as illustrated in Fig. 2.5. The OFRR is connected to plastic tubing so that the liquid solution can be flowed through the OFRR using a syringe pump at the withdrawal mode. The optical fiber taper is connected to a tunable diode laser (JDS Uniphase, center wavelength 1550 nm) on one end and to a photodetector on the other. Both OFRR capillary and fiber taper are mounted on individual three-dimensional optical stages. The tunable diode laser is periodically scanned across a small wavelength range of 110 pm while the photodector measures the optical intensity. The OFRR is brought into contact with the fiber taper (see Fig. 2.6(A)) and the transmission spectrum collected by a data acquisition (DAQ) card is monitored and displayed in LabView in real-time. During each scan, when the laser wavelength matches the WGM resonant condition (Eq. (2.1)), the light evanescently

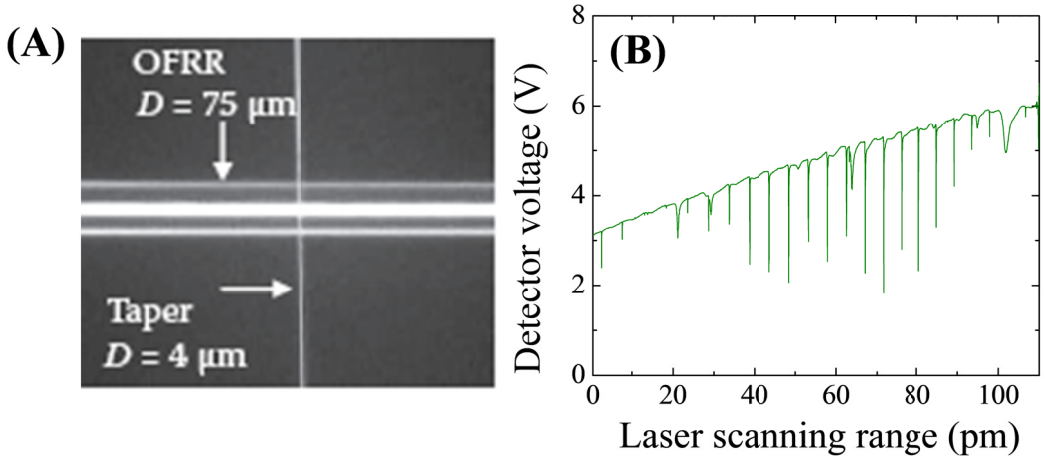

Fig. 2.6 (A) Microscope image of OFRR capillary in contact with the optical fiber taper for WGM excitation. (B) Typical OFRR transmission spectrum. Tunable diode laser central wavelength is around 1550 nm and is scanned over 110 pm range at a frequency of 5 Hz.

couples into the OFRR and causes the measured transmission intensity to drop, leaving a spectral dip at the photodetector, as shown in Fig. 2.6(B).

2.2.3.2 Q-factors

The loss of an optical cavity is an important parameter, as it determines the number of round trips of the light supported by the ring resonator before it dissipates out. Cavity loss is commonly expressed in terms of quality factor, Q, through the following equation:

$$Q=\lambda/\Delta\lambda=\omega\tau, \tag{2.2}$$

where λ is the WGM resonant wavelength, $\Delta\lambda$ is the full width measured at half maximum (FWHM) of the intensity, ω is the optical angular frequency ($\omega=2\pi c/\lambda$), and τ is photon lifetime. From the intrinsic relationship between tge Q-factor and photon lifetime, we know that a high Q-factor will lead to a low LOD in sensing and a low

threshold in lasing. There are many loss mechanisms in an optical cavity. For OFRR gas sensing, the total Q-factor can be decomposed into following equation:

$$Q_{total}^{-1} = Q_{rad}^{-1} + Q_{wall}^{-1} + Q_{sca}^{-1} + Q_{polymer}^{-1} + Q_{coupling}^{-1}, \quad (2.3)$$

where Q_{rad}, Q_{wall}, and Q_{sca} are the radiation loss caused by a curved dielectric cavity, material loss caused by the capillary wall medium, and the loss resulting from the OFRR surface scattering. These three types of losses combined are usually called cavity intrinsic loss. In OFRR gas sensing, a polymer layer is deposited on the capillary inner surface (see Chapter 3 for details), and thus $Q_{polymer}$ denotes the combined loss caused by polymer optical absorption and by the scattering by polymer surface/body imperfections. $Q_{coupling}$ represents the energy loss due to the optical taper output coupling. For OFRR lasers, the optical cavity will be filled with liquid solution, which may cause additional loss, as reflected by Q_{sol}. The total Q-factor for OFRR laser in the absence of dye molecules is then determined by the following equation:

$$Q_{total}^{-1} = Q_{rad}^{-1} + Q_{wall}^{-1} + Q_{sca}^{-1} + Q_{coupling}^{-1} + \eta Q_{sol}^{-1}, \quad (2.4)$$

where $Q_{sol}=2\pi n/\lambda\alpha_{sol}$, α_{sol} is the absorption coefficient of the solvent, and η is the fraction of light in the capillary core, which is usually less than 0.1.

The radiation loss is dependent on the cavity size, and for the OFRR larger than 10 μm in diameter, the WGM can have $Q_{rad} >> 10^{11}$ [9]. Q_{wall} and Q_{sca} are expected to be around 10^{10}, which has been investigated in detail in Ref. [87, 88] on fused silica microspheres. Therefore, the OFRR intrinsic Q-factor is around 10^{10}. In OFRR gas sensing, the total Q-factor is limited by the $Q_{polymer}$ and $Q_{coupling}$, which can be determined in experiment. In OFRR lasers, for a number of commonly used solvent such as methanol,

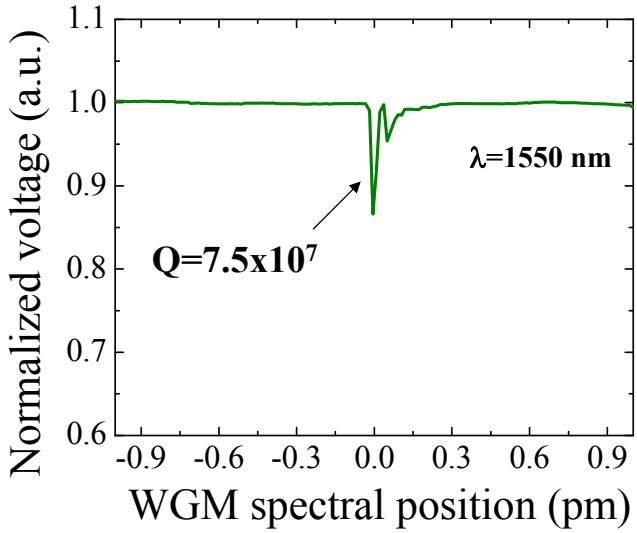

Fig. 2.7 OFRR Q-factor measurement. The transmission spectrum showing a WGM has a Q-factor of $7.5x10^7$.

ethanol, chloroform, and water, $Q_{sol} >> 10^8$, due to low optical absorption of those solvents at the visible spectrum [89-91]. Therefore, Q_{total} is expected to be over 10^8 [92].

To experimentally measure the empty Q-factor (the OFRR core is filled with air), the characterization setup illustrated in Fig. 2.5 is used. After a transmission spectrum is obtained for OFRR, the Q-factor for individual resonant mode can be calculated as $Q=\lambda/\Delta\lambda$. A WGM Q-factor of $7.5x10^7$ is measured in Fig. 2.7. Note that this Q measurement is limited by the laser scanning step size.

2.2.3.3 Etching

After pulling the OFRR capillary as described in the Section 2.2.2, the wall thickness may not be as thin as desired for sensing and lasing purposes. Further reduction of the wall thickness is carried out with hydrofluoric acid (HF) etching by using two different protocols.

The first etching protocol is used in preparing OFRR capillaries for gas sensing experiments in Chapter 3 and Chapter 4. A series of diluted concentrations of HF is passed slowly through the OFRR, where the capillary inner surface is gradually etched away. The etching starts with 12% HF solution in water. During the etching process, we monitor the WGM spectral shift using the setup illustrated in Fig. 2.5. As the OFRR wall thickness decreases, the WGM spectral position shifts to a shorter wavelength, according to Eq. 2.1, since water (RI=1.33) replaces glass (RI=1.45), resulting in a smaller effective RI. We then switch to lower HF concentrations progressively when the wall becomes thinner and thinner, and the WGM spectral shift becomes too fast to monitor.

The second etching protocol is used in preparing OFRR capillaries for lasing experiments in Chapter 5 and Chapter 6. The HF etching is conducted on the outer surface of a pre-form. Specifically, the capillary pre-form is sealed with optical glue at both ends and then immersed in 3% HF water solution for 17 hours at room temperature. After etching, the pre-form is pulled under CO_2 laser irradiation using the same method described in Section 2.2.2.

The Q-factor over 10^{10} can be achieved in the OFRR after pulling, due to the ultra-smooth glass surface generated from CO_2 laser irradiation [93]. However, the HF etching in the first protocol causes surface roughness due to the subsequent HF etching, thus decreasing the final Q-factor of the OFRR. The second protocol solves this problem, because the CO_2 laser irradiation occurs after the etching. Consequently, the ring resonator surface is re-generated and high Q-factors are preserved. The second etching protocol is adopted when a high Q-factor is desired. For example, in OFRR lasing experiments, a high Q-factor ($>10^7$) is needed to achieve an ultra-low lasing threshold.

However, for OFRR gas sensing experiments, the effective Q-factor is limited by the loss from polymer coating, instead of the glass surface roughness induced by the etching process. Therefore, the first etching protocol is used because the etching process, hence the resultant wall thickness, can be monitored in real-time with the WGM spectral shift.

2.2.3.4 Sensitivity calibration

As mentioned earlier, the OFRR wall thickness is an important parameter that determines the strength of the light-analyte interaction and hence the sensitivity of the sensor. The direct method to characterize the wall thickness is through SEM measurement, however, the SEM characterization needs to break the capillary and the measurement process easily introduces contaminants to the capillary surface, which will degrade the Q-factor of the OFRR. Therefore, here we use an alternative noninvasive method to characterize the wall thickness. By measuring the OFRR bulk RI sensitivity, which is the sensor response to the RI change occurring in the homogeneous bulk solution, we can infer the wall thickness of the capillary.

The bulk RI sensitivity (or sensitivity for simplicity) is usually characterized using solutions of known refractive indices. In our experiment, an ethanol-water mixture is used because the RI of different concentrations of ethanol-water solution is known, as illustrated in Fig. 2.8. The WGM spectral shift per refractive index unit (RIU) is used to specify sensitivity. Initially, the OFRR is filled with water to establish the WGM spectral position as the baseline. A mixture of water and ethanol, which has a higher RI than pure water, is then passed through the OFRR, resulting in a shift to a longer wavelength in the WGM spectral position, as shown in the sensorgram in Fig. 2.9(A). The sensitivity is then

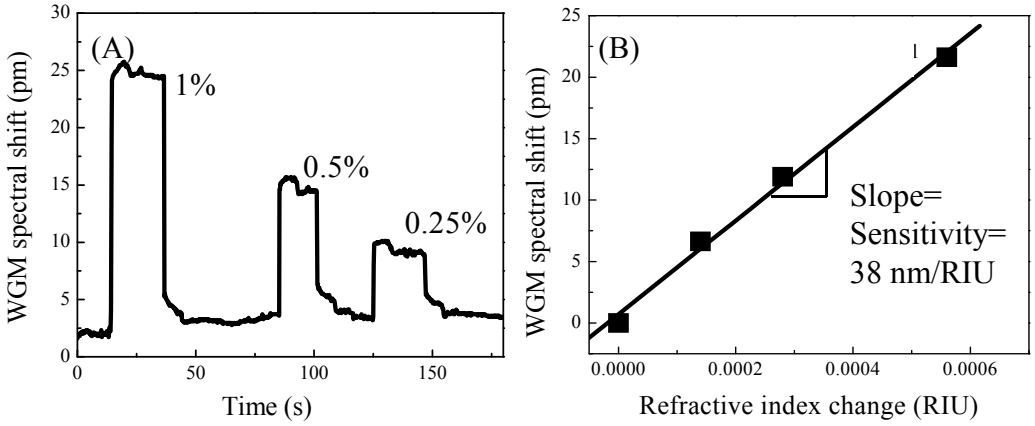

Fig. 2.9 (A) Sensorgram of the WGM response to ethanol-water mixtures at different concentrations. (B) Sensitivity calibration curve, which is a linear fitting from data points from (A).

calculated from the slope of each response curve. WGM spectral shift versus the change in the RI is then plotted, as illustrated in Fig. 2.9(B). The data points are fitted with the linear regression. The slope of the linear curve is the sensitivity of the OFRR sensor, which is 38 nm/RIU for the particular OFRR shown in Fig. 2.9(B).

2.2.4 Theoretical analysis

The WGM of the OFRR can fully be described using the Mie theory by considering a three-layered radial structure [66, 94]. The radial distribution of the WGM electrical field of an OFRR is governed by:

$$E_{m,l}(r) = \begin{cases} AJ_m(k_{m,l}n_1 r) & (r \le r_1) \\ BJ_m(k_{m,l}n_2 r) + CH_m^{(1)}(k_{m,l}n_2 r) & (r_1 \le r \le r_2) \\ DH_m^{(1)}(k_{m,l}n_3 r) & (r \ge r_2) \end{cases}, \tag{2.5}$$

where J_m and $H_m^{(1)}$ are the mth Bessel function and the mth Hankel function of the first kind, respectively. The refractive index of the core, wall, and the surrounding medium is described by n_1, n_2, and n_3. The terms r_1 and r_2 represent the inner and outer radius of the OFRR, respectively, and $k_{m,l}$ is the amplitude of the wave vector in vacuum for the lth order radial WGM. Using this three-layer model, the WGM spectral position, the radial distribution of the light, and Q_{rad} can be obtained as a function of the wall thickness, the OFRR size, operating wavelength, *etc*. In this section, Matlab is used to solve Eq. (2.5) to illustrate two unique properties of OFRR capillary below.

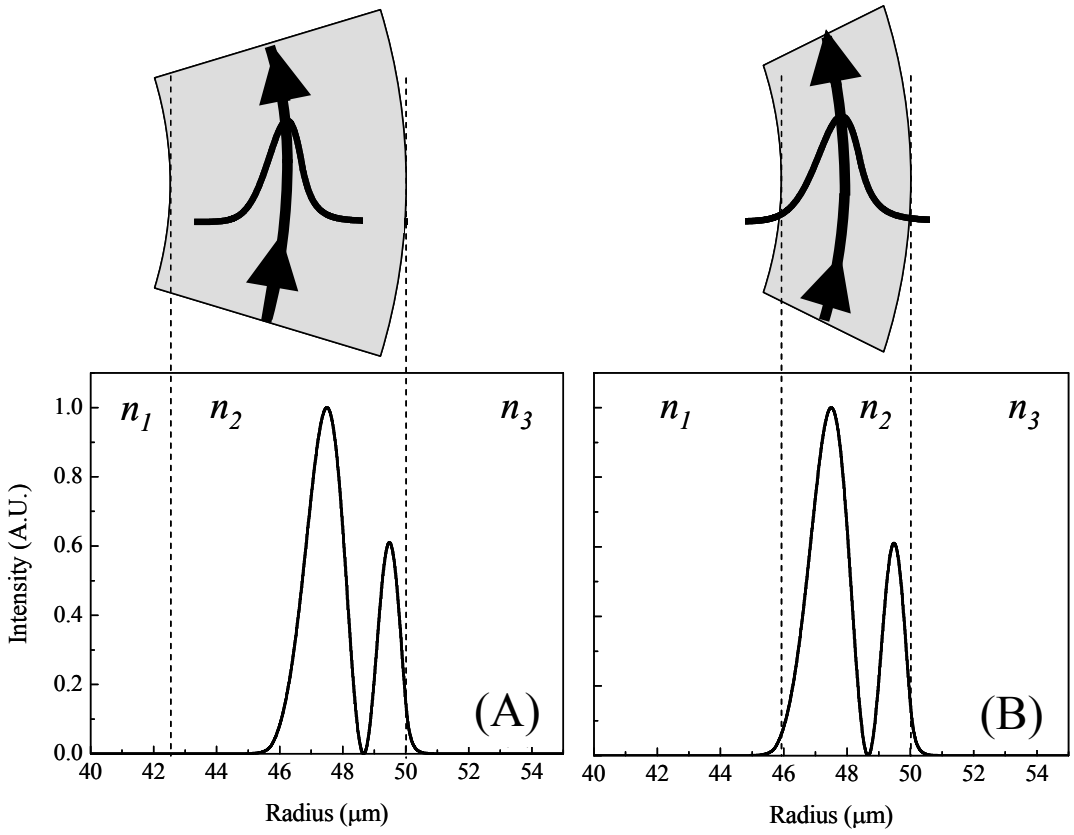

Fig. 2.10 Intensity distribution of the second order radial WGMs for two different fused silica wall thicknesses shows that the wall needs to be sufficiently thin to expose the evanescent field to the core. Dashed lines show the interior and exterior surfaces of the OFRR. Refractive index: n_1=1.33, n_2=1.45, n_3=1.0.

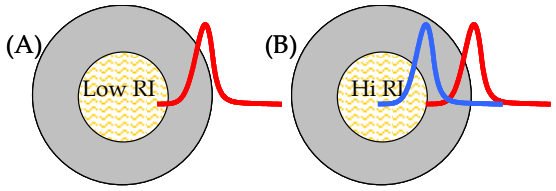

Fig. 2.11 (A) Low core RI. The WGMs form at the outer glass wall and has an evanescent field in the core. (B) High core RI. The WGMs exist at both inner and outer surface of the glass wall.

Why thin-walled capillary is necessary?

Using thin-walled capillaries (*i.e.*, a few micrometers), a significant evanescent field of the WGM can be present near the inner surface of the OFRR, as illustrated in Fig. 2.10. Take a 2nd-order radial mode for example. When the capillary wall is thick (*i.e.*, 7.5 μm in Fig. 2.10(A)), the WGM intensity is mostly confined within the wall region, with a virtually negligible evanescent field in the core. In contrast, when the capillary wall thickness is sufficiently thin (*i.e.*, 4 μm in Fig. 2.10(B)), the evanescent field of the WGM starts to expose to the capillary core, and interacts with the analytes near the capillary inner surface or inside the capillary, which is the key to OFRR sensing and lasing.

OFRR works with solutions of any RI

In optofluidic laser applications (detailed in Chapter 5), it is desirable that the laser cavity is capable of operating with liquid solution of any RI. As mentioned in Chapter 5, currently, almost all the optofluidic laser cavities can only work with liquid RI either lower *or* higher than the cavity RI (depending on the specific design of the cavity). However, the unique thin-walled structure makes the OFRR versatile to accommodate liquid of any RI. Fig. 2.12 shows that the OFRR continuously supports the WGM that interacts with the liquid when the core changes from low RI to high RI [95]. As shown in

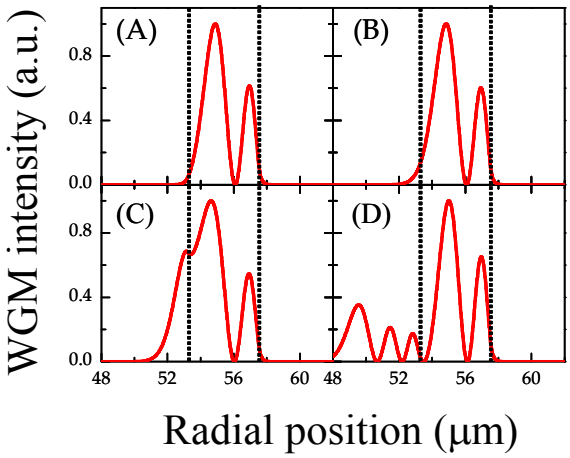

Fig. 2.12 Transition of the WGM when the core changes from low RI to high RI. Core RI is (A): 1.33; (B) 1.45; (C) 1.5; (D) 1.6. RI for OFRR wall: 1.45. Surrounding medium: air. Dashed lines are OFRR inner and outer surface.

Fig. 2.11(A), when the RI of the liquid core is lower than that of the glass wall, the circular cross section of the capillary forms a ring resonator that supports the WGM bound by the OFRR outer surface and the surrounding medium. Due to the thin wall, the evanescent field of the WGM has sufficient exposure to the capillary core so as to provide the optical feedback for lasing. With the increased core's RI, the WGM is gradually "pulled" into the core, as shown in Fig. 2.11(B) and (C). When the core's RI exceeds that of the wall by a large amount, the WGM forms at both OFRR inner surface and outer surface, as shown in Fig. 2.11(D). Due to the thin wall, these two sets of modes interact strongly to form so-called photonic molecules [95, 96], which redistribute the WGM so that the electric field exists both in the core and outside of the OFRR [95].

2.3 Conclusion

In this chapter, a detailed introduction to the OFRR platform is given, including fabrication, characterization, and theoretical analysis. As we have shown, the OFRR has efficient microfluidics inherent to the capillary and is versatile to accommodate liquid of any RI. Therefore, the OFRR is well poised for sensing and lasing applications that will be studied in detail in the following chapters.

Chapter 3

OFRR Chemical Vapor Detection

3.1 Introduction and motivation

Chemical vapor sensors have broad applications in environmental monitoring, homeland security, military surveillance, and biomedical diagnosis. The desirable characteristics of a chemical vapor sensor include ultra-high sensitivity, specific and rapid response to certain vapor molecule, as well as the ability for on-the-spot chemical analysis, which usually requires the sensor to be small, portable, reusable, stable, robust, and cost-effective. Towards this end, various sensing technologies have been studied extensively in recent years [97-102]. Among them, optical sensors are a powerful tool in gas detection and analysis. Especially when the vapors are flammable or explosive, optical sensor provides an inherently safe detection by eliminating the danger of igniting the vapor during the test. A further advantage of optical sensor is that the optical signal is less sensitive to electromagnetic noise than other detection technologies, and thus better LOD can be potentially achieved.

According to the sensing mechanism, optical vapor sensors can be divided into the following four categories: optical absorption measurement (*i.e.*, direct absorption measurement [103-106], Fourier transform infrared spectroscopy [107, 108],

photoacoustic spectroscopy [109], and cavity ring down spectroscopy [110]), photoluminescence measurement [111], Raman spectroscopy [112] and surface enhanced Raman spectroscopy [113], and RI measurement.

The RI measurement relies on the detection of RI changes caused by the interaction of vapor molecules and the sensing material deposited on the sensor surface. The sensing signal is proportional to the vapor concentration rather than the total mass, which makes the technique very attractive in building miniaturized vapor sensors and sensor arrays in field deployment and environmental monitoring as well. A variety of optical structures have been developed to detect the RI change, including waveguides [114], optical fibers (*i. e.*, D-shaped) [115-117], fiber Bragg gratings (FBGs) and long period gratings (LPGs) [117-120], Fabry-Pérot cavities [121, 122], interferometers [123, 124], photonic crystal fibers [125, 126], surface plasmon resonance (SPR) [127], and localized surface plasmon resonance (LSPR) spectroscopy [128-130].

Recently, as another type of RI sensor, optical ring resonators are under investigation as a promising chemical vapor sensing technique [24, 62, 131-137]. One of the major advantages of the ring resonator is its compact size. In a ring resonator, the light propagates in the form of WGMs or circulating waveguide modes [138]. Although the ring resonator is only a few tens to a few hundreds of micrometers in size, the effective detection length can significantly be enhanced due to the high Q-factors of the WGMs, as detailed in Chapter 2. Therefore, the ring resonator technology enables large density of sensor arrays for portable devices with multiplexed detection capability. Like many other optical chemical vapor sensors, the ring resonator vapor sensor relies on the polymer to provide certain selectivity towards the analytes. In the presence of vapor

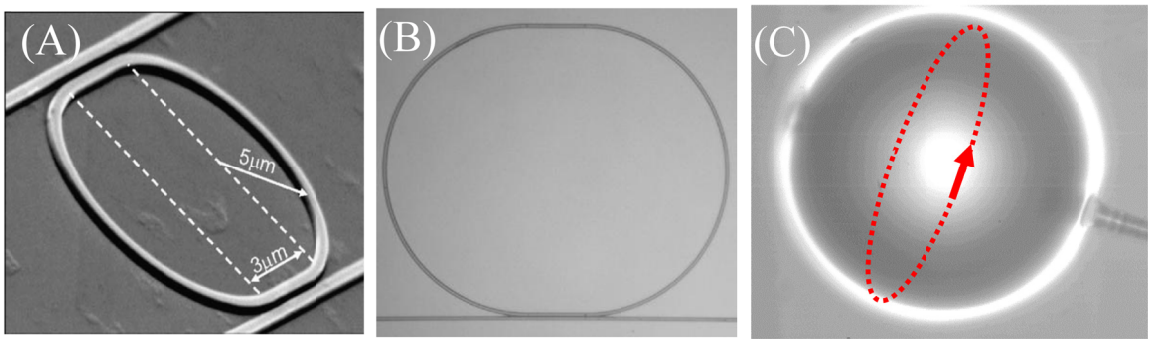

Fig. 3.1 Various configurations of ring resonator vapor sensor. (A) Planar ring resonator. (B) Polymer ring resonator. (C) Dielectric microsphere. Reprinted with permission from Refs. [62, 136].

molecules, the polymer undergoes RI and thickness change [24, 127], resulting in a WGM spectral shift. Therefore, by directly or indirectly monitoring the WGM spectral position in real time, both quantitative and kinetic information regarding the interaction between vapor molecules and the polymer can be extracted.

So far, there are three basic ring resonator configurations that have been studied as a vapor sensor, as illustrated in Fig. 3.1. They include (1) chip based planar ring resonators made of solid dielectric materials such as SiON and coated with a vapor sensitive polymer as the cladding (Fig. 3.1(A)) [24, 62, 131], (2) chip based polymer ring resonators, in which polymer is used as the building block of the ring resonator and also as the sensing material (Fig. 3.1(B)) [136, 137], and (3) free-standing microspheres whose exterior surface is coated with a layer of polymer (Fig. 3.1(C)) [135]. While these ring resonators have been investigated for sensitive detection of alcohol [24, 136], ammonia [131], and explosives [137], they suffer from cumbersome and ineffective gas fluidics, which is also commonly seen in many other optical vapor sensors. In some cases these sensors are placed in large conventional gas cells with a gas flow rate as high as tens of liters per minute [117, 139]. This not only requires a large amount of gas analytes,

but also significantly slows down the sensing response and recovery time (a few to a few tens of minutes may be needed [24, 136]). Both may deteriorate the sensor performance, especially in the situation where fast response and short recovery time are needed and where only low sample quantity is available.

To overcome the lack of effective fluidics issue seen in the current microring resonator vapor sensors, in this chapter, we develop a novel sensing configuration using the OFRR, which naturally integrates the ring resonator with capillary microfluidics. We investigate experimentally and theoretically the sensing capability of the OFRR. Experimentally, we demonstrate rapid detection of ethanol and hexane vapors, respectively, and show the OFRR sensor can provide certain selectivity towards vapors by coating different sensing polymers. Our theoretical studies involve analysis of WGM sensitivity in terms of OFRR physical dimension (capillary diameter and wall thickness), polymer coating RI and thickness, and resonant mode order and polarization. The design guidelines are provided for ring resonator vapor sensors in order to balance their performance in sensitivity, LOD, and response time according to the application area.

3.2 OFRR vapor sensing principle

As illustrated in Fig. 3.2, the OFRR interior surface is coated with a polymer thin film of several tens to several hundreds of nanometers. The capillary itself functions as a micro-sized vapor cell. During a sensing event, vapor analyte is flowed through the capillary from one end (gas inlet) to the other (gas outlet). Due to the small size of the capillary, the sample volume needed for one test is 30 nL assuming OFRR diameter is 65

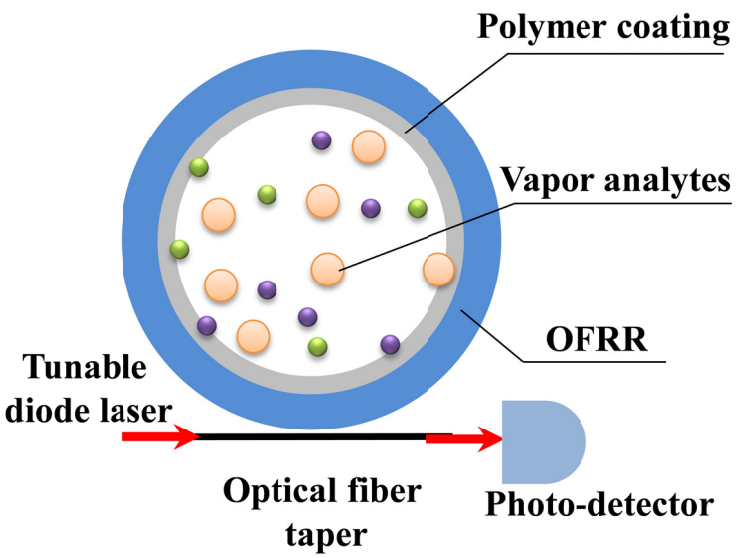

Fig. 3.2 The cross-sectional view of an OFRR vapor sensor.

μm and capillary length is 1 cm, which is orders of magnitude smaller than the conventional optical vapor sensors reported previously. The excellent capillary fluidics also benefits the sensor response and regeneration time, which makes fast detection of chemical vapors possible. The circular cross section of the capillary forms an optical ring resonator, where WGMs are supported by total internal reflection of the light along the curved inner/outer boundary [138]. The WGM can be excited at any place along the OFRR by a tapered fiber in contact with the OFRR capillary. The WGM resonant wavelength (or spectral position), λ_{WGM}, is governed by $\lambda_{WGM} = 2\pi R n_{eff}/m$ [45], where R is the OFRR radius, n_{eff} is the effective RI experienced by the WGM, and m is an integer. Since the OFRR capillary wall is thin (<4 μm), the WGM has significant electric field in the polymer layer. When vapor molecules are delivered into the OFRR, they are absorbed and diffuse into the polymer. The interaction process cause changes in polymer RI and thickness (polymer may swell or shrink). Both effects will result in a change in n_{eff}, and

hence λ_{WGM}. By monitoring the WGM spectral shift in time, the quantitative and kinetic information regarding the vapor molecule interaction with the polymer can be acquired.

3.3 Experimental studies of OFRR vapor sensing

3.3.1 Sensor preparation

An OFRR is fabricated by rapidly pulling a capillary pre-form (Polymicro Technologies, Phoenix, AZ) under CO_2 laser irradiation using a home-build pulling system. After direct pulling, the OFRR capillary has an OD around 90 μm and a wall thickness around 5 μm, suggested by SEM characterization. In order to increase the sensitivity, the OFRR is further etched by diluted HF solution to reduce the wall thickness and to expose a sufficient fraction of light to the polymer layer [134]. The etching process is controlled by bulk RI sensitivity calibration (as detailed in Chapter 2) to yield a wall thickness in the range of 2.8 to 3.0 μm. Each OFRR is calibrated separately before use. Helium is used to dry the OFRR capillary interior surface after etching.

The OFRR interior surface is then coated with two different polymers, moderately polar methyl phenyl polysiloxane (OV-17, Sigma-Aldrich, St. Louis, MO) or highly polar polyethylene glycol (PEG, Fluka, Buchs, Switzerland), for the detection of different types of chemical vapors. The coating procedures are adapted from well-developed static coating procedures for GC microfabricated columns [140]. Briefly, the polymer dissolved in an organic solvent such as toluene, methanol, or acetone is first filled into the OFRR by capillary force. Then both ends of the OFRR are sealed with a septum and the polymer

solution is left in the OFRR for one hour. After this, low vacuum is applied at one end to gradually evaporate the coating solvent out of the OFRR, followed by high vacuum for twelve hours. All the coating procedures are carried out at room temperature. The thickness of the polymer coating can be controlled by varying the concentration of coating solution and the concentration used in this study should yield an average thickness of 200 nm. Finally, the OFRR capillary is checked under a microscope to ensure that a uniform and smooth polymer thin film has been formed.

Smooth and uniform polymer surface after vacuum plays a key role to ensure good OFRR sensing performance. We have observed in experiments that toluene after vacuum is prone to leave a number of cavities of a few micrometers in diameter on the surface. These cavities will induce additional scattering loss for the WGMs in the OFRR, which greatly degrade the Q-factor, and hence the LOD of the OFRR vapor sensor. Moreover, these small cavities have different adsorption characteristics compared to smooth polymer surface. Vapor molecules may be retained for a longer time at the cavity, which increases the response time and recovery time. Acetone and methanol are found to be better candidates for solvents because they usually leave uniform and smooth surface after vacuum.

3.3.2 Rapid chemical vapor sensing

In this part, we demonstrate OFRR's capability as a rapid chemical vapor sensor. During experiments, ethanol and hexane vapors are used as a model system and represent polar and nonpolar analytes, respectively.

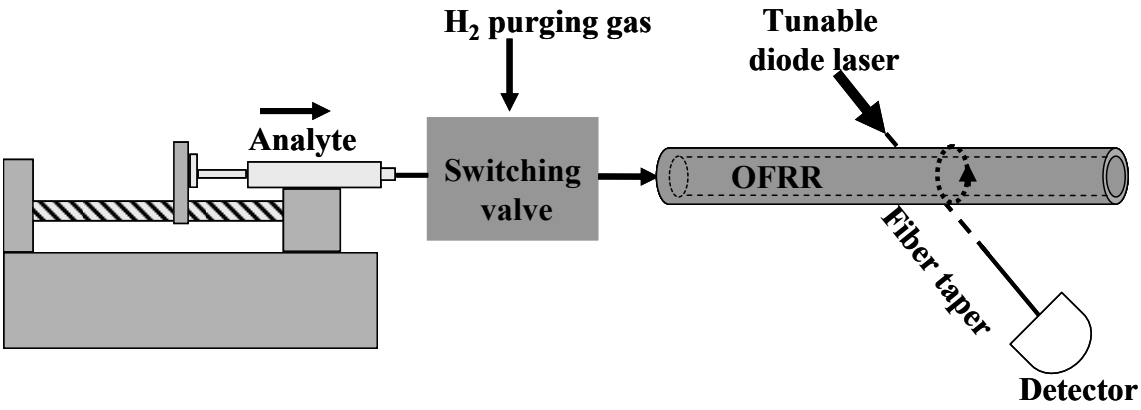

Fig. 3.3 Experimental setup for rapid chemical vapor detection.

Fig. 3.3 illustrates the schematic of the experimental setup. Various concentrations of analyte/air vapor mixture is injected into the OFRR capillary by a syringe pump (Harvard Apparatus, MA) at a flow rate of 1 mL/min. Ultra-high purity hydrogen is flowed into the OFRR before injection of the vapor samples to establish the sensing baseline and then after each sensing measurement to purge the analytes. A switching valve (Upchurch Scientific, WA) is used to quickly switch between the analyte channel and the purging channel. The vapor detection can be performed at any locations along the OFRR capillary, through a fiber taper perpendicular in contact with the OFRR. A tunable diode laser (central wavelength at 1550 nm) is scanned over 220 pm range in wavelength (scanning rate: 5-15 Hz) is coupled into the WGM via the optical fiber taper. When the light is on resonance with the WGM, it is coupled into the OFRR, leaving an intensity dip at the fiber output end (monitored by a photodetector), which is used to indicate the WGM spectral position. When vapor molecules pass through the OFRR, they interact with the polymer layer, causing an RI change and thickness change in the polymer layer, which leads to a spectral shift in the WGM. The Q-factor of the OFRR is

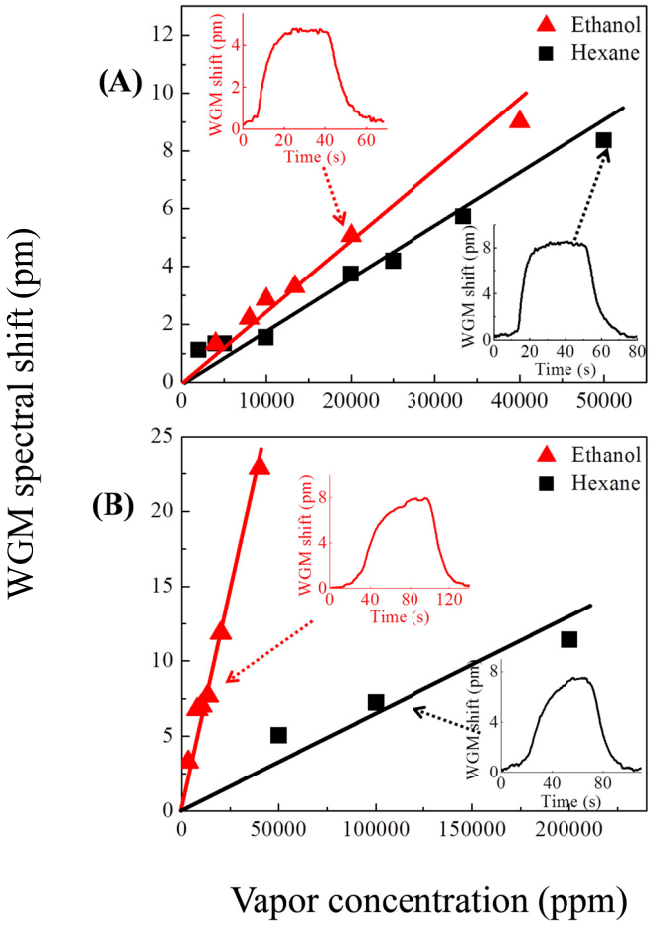

Fig. 3.4 OFRR response to various part per million (ppm) concentrations of ethanol and hexane vapors. The OFRR is coated with a 200-nm-thick OV-17 (A) and PEG-400 (B). Insets are the sensorgrams taken by monitoring the WGM shift in real time. Reprinted from Ref. [133] with permission.

approximately 10^6 and the whole OFRR is placed on a plastic module covered by a glass slide to minimize temperature fluctuations.

The inset of Fig. 3.4(A) shows the sensorgrams when ethanol or hexane vapor is introduced to an OV-17 coated OFRR. H_2 is initially flowed through the OFRR to establish the baseline. Then the valve is switched to the analyte channel. Upon the interaction with the analyte, the WGM shifts to a longer wavelength and reaches the equilibrium value within 10 seconds. Then the flow is switched back to H_2 to purge the

OFRR, as reflected by the decrease in the WGM spectral position. There are two phenomena worthy of pointing out, which attest to the rapid and efficient nature of the OFRR vapor sensor. First, purge is completed within 20 seconds, much faster than the previous ring resonator designs and many other types of optical vapor sensors. Second, thorough purge can be achieved, as evidenced by the fact that the WGM returns to the baseline every time after purge.

Fig. 3.4(A) plots the WGM shift obtained at the equilibrium for various concentrations of ethanol or hexane vapor by the OV-17 coated OFRR. The sensitivity is nearly the same for ethanol and hexane for OV-17, which contains 50% modestly polar phenyl groups and 50% non-polar methyl groups. For a comparison, Fig. 3.4(B) plots the sensitivity curve for ethanol and hexane using another OFRR coated with PEG-400. Both Fig. 3.4(A) and (B) indicate that the WGM shift linearly depends on the analyte concentration. Sensitivity for ethanol vapor with PEG is 0.5×10^{-3} pm/ppm, ten times higher than that for hexane, as PEG-400 is highly polar, hence having higher polar interactions and solubility for ethanol. To estimate the LOD for ethanol vapor, we use a WGM resolution of 0.1 pm [133], which can be obtained without any active temperature control. Based on Fig. 3.4(B), an LOD of 200 ppm for ethanol vapor can be derived.

3.4 Theoretical analysis of OFRR gas sensing performances

In an optical vapor sensor, the sensing signal depends directly on the strength of the light-matter interaction, and thus it is important to understand the WGM spatial distribution and calculate quantitatively the fraction of the light in the polymer layer,

which is responsible for producing the spectral shift. In this part, we first establish a four-layer Mie scattering model to describe the mode spatial distribution in the OFRR vapor sensor. Based on this model, we study the sensor sensitivity and give design guidelines to an optical vapor sensor.

3.4.1 Theoretical description

The WGM spectral position can be solved by considering the four-layer Mie model, as illustrated in Fig. 3.5. The radial distribution of the WGM for the four-layered OFRR is given by [94]

$$E_{m,l}(r)=\begin{cases} AJ_m(kn_1r) & (r\le OD/2-d-t) \\ BJ_m(kn_2r)+CH_m^{(1)}(kn_2r) & (OD/2-d-t\le r\le OD/2-d) \\ DJ_m(kn_3r)+EH_m^{(1)}(kn_3r) & (OD/2-d\le r\le OD/2) \\ FH_m^{(1)}(kn_4r) & (r\ge OD/2) \end{cases}, \tag{3.1}$$

where J_m and $H_m^{(1)}$ are the mth Bessel function and the m^{th} Hankel function of the first kind, respectively. The RI of the core, the polymer, the ring resonator wall, and the surrounding medium are described by n_1, n_2, n_3, and n_4. $k=2\pi/\lambda$, where λ is the WGM wavelength in vacuum. The WGMs have two polarizations, a-mode and b-mode, with the magnetic field and the electric field being along the cylinder longitudinal direction, respectively.

The OFRR sensor sensitivity can be described by:

$$S=\frac{d\lambda}{d\rho}=\frac{\partial\lambda}{\partial t}\cdot\frac{\partial t}{\partial\rho}+\frac{\partial\lambda}{\partial n_2}\cdot\frac{\partial n_2}{\partial t}\cdot\frac{\partial t}{\partial\rho}+\frac{\partial\lambda}{\partial n_2}\cdot\frac{\partial n_2}{\partial\rho}, \tag{3.2}$$

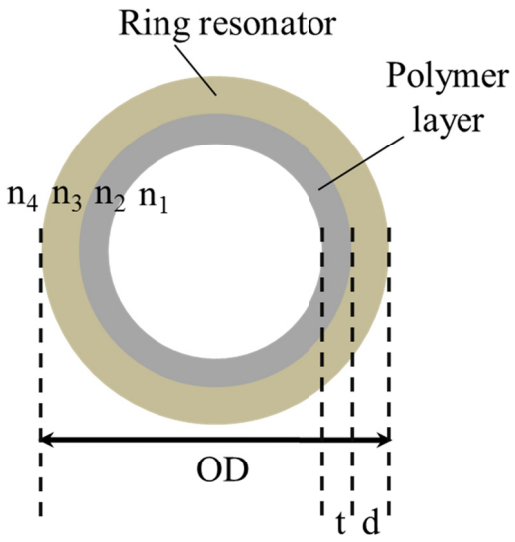

Fig. 3.5 Four-layer model for the OFRR vapor sensor. *OD*: ring resonator outer diameter; *t*: polymer thickness; *d*: ring resonator wall thickness; n_1, n_2, n_3, and n_4 are the refractive indices for the medium inside (air), polymer, silica ring resonator, and medium outside (air), respectively.

where $d\lambda/d\rho$ is the WGM spectral shift due to the change of the vapor molecule density in the polymer matrix, ρ. $\frac{\partial \lambda}{\partial t}$ and $\frac{\partial \lambda}{\partial n_2}$ refer to the WGM thickness sensitivity (S_t) and RI sensitivity (S_{RI}), respectively, which are the intrinsic properties associated with the optical modes of the coated ring resonator. $\frac{\partial t}{\partial \rho}$ and $\frac{\partial n_2}{\partial \rho}$ are the polymer swelling/shrinkage and the RI change due to the vapor molecule absorption, which depend on the polymer-analyte interaction. Note that the RI change can be caused by either the polymer volume change induced by vapor molecules, or by the doping effect due to the presence of the vapor molecules in the polymer matrix [127], as described respectively by the second and the third term on the right-hand-side of Eq. (3.2).

RI sensitivity for the polymer RI change, S_{RI}, is related to the fraction of light in the polymer, η, by [141-143]:

$$S_{RI} = \frac{\partial \lambda}{\partial n_2} = \frac{\lambda}{n_{eff}} \eta, \tag{3.3}$$

where $n_{eff} = m\lambda/2\pi R$ (R: ring resonator radius) is the WGM effective RI. However, the thickness sensitivity is more complicated, which will be discussed later in Chapter 3.2.2. While the polymer thickness change due to vapor molecules adsorption and the thickness-induced RI change may have to be determined experimentally [123, 144, 145], the RI change due to the doping effect can be modeled by the Lorentz-Lorenz equation [127]:

$$\delta n_2 = \frac{(n_2{}^2 + 2)^2}{6 n_2} \frac{1}{3\varepsilon_0} (\delta \rho) \alpha, \tag{3.4}$$

where α is the vapor molecule polarizability. It should be noted that the polymer RI change and thickness change may not work additively. For example, while the doping induced polymer RI change is always positive, its thickness related RI decreases when the polymer swells upon interaction with the analyte.

3.4.2 Theoretical analysis of the OFRR vapor sensor

Using the model presented in Chapter 3.4.1, we systematically investigate two cases where the polymer RI is lower and higher than that of the capillary wall.

3.4.2.1 Low RI polymer coating

When the polymer RI is smaller than or close to that of the ring resonator, the polymer layer can be regarded as an extension of the ring resonator wall, regardless of the polymer thickness. Initially, when the polymer layer is thin, only the evanescent field exists in the polymer layer and the RI sensitivity is low. With the increased polymer

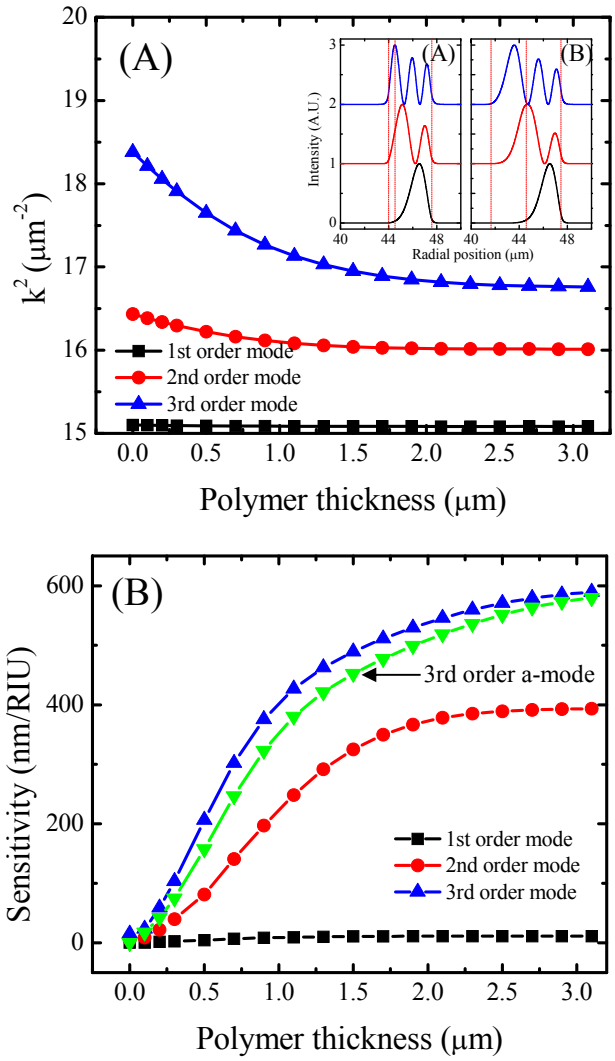

Fig. 3.6 (A) k^2 as a function of polymer thickness for the first three WGMs. The relevant parameters are: OD = 95 μm. d = 3 μm. n_1 = 1. n_2 = 1.47. n_3 = 1.45. n_4 = 1. m = 257. All for b-mode. *Inset*: Intensity radial distribution for the first three modes when the polymer thickness is 0.5 μm (A) and 2.9 μm (B). *Vertical lines* indicate the boundaries of the ring resonator and the polymer layer. (B) The corresponding RI sensitivity. The RI sensitivity for the third WGM of different polarization (a-mode) is also plotted. Reprinted from Ref. [134] with permission.

thickness, higher order modes start to move inward, resulting in a higher RI sensitivity for those modes while the lower order modes are not affected much. This behavior is shown in the insets of Fig. 3.6(A). The thickness sensitivity, S_t, can be deduced from the

slope of the curves in Fig. 3.6(A). S_t is always positive. However, it drops gradually to zero when polymer thickness increases, meaning that the sensor is insensitive to any polymer thickness change for the thick polymer layer. The RI sensitivity, S_{RI}, is plotted in Fig. 3.6(B), which increases monotonically with the increased polymer thickness. The maximum of S_{RI} depends highly on the mode order. The higher order the mode, the higher S_{RI} it can achieve. This is a result of Eq. (3.3), as higher order modes have more fraction of light in the polymer. Polarization dependent S_{RI} is also given in Fig. 3.6(B), showing that the b-mode has a slightly higher sensitivity than the a-mode.

For the OFRR-based vapor sensor, the ring resonator wall thickness has a significant impact on the sensor performance. Since the polymer layer is treated as the extension of the ring resonator, the relative thickness between the wall and the polymer determines the radial intensity distribution of the WGMs. As a result, the fraction of light and hence the RI sensitivity is lower with a thicker-wall ring resonator, as shown in Fig.

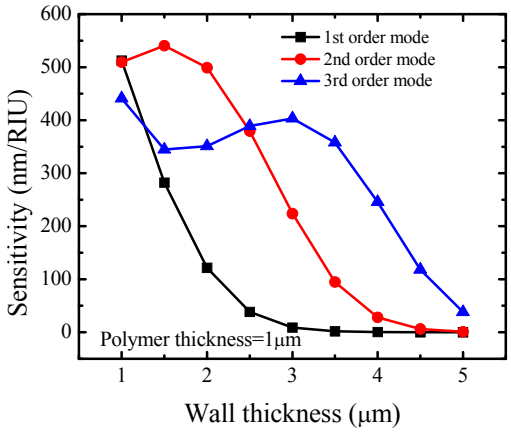

Fig. 3.7 RI sensitivity as a function of the OFRR wall thickness for the first three WGMs. The polymer thickness is fixed at 1 mm. Other parameters are the same as in Fig. 3.6. Reprinted from Ref. [134] with permission.

3.7. Eventually, the RI sensitivity drops to zero when the wall is sufficiently thick, in which case, the WGM is predominantly confined within the wall.

3.4.2.2 High RI polymer coating

When a polymer of sufficiently high RI is used as the coating material, the WGMs exhibit completely different behavior. Initially, the light is confined within the ring resonator wall as a wall mode. With the increased polymer thickness, the polymer starts to support a new set of WGMs that interact with the wall modes to form a so-called photonic molecular mode that has characteristics from both wall mode and polymer layer mode [95, 96]. Fig. 3.8(A) shows the dispersion for the three lowest modes in such a polymer coated ring resonator. The energy splitting occurs when the 1^{st} order wall mode (shown as the dashed line in Fig. 3.8(A)) intersects the polymer modes. Eventually, when the polymer is sufficiently thick, polymer modes and wall modes are de-coupled. This is equivalent to creating a new polymer ring resonator in a capillary and the glass capillary simply acts as the physical substrate. Fig. 3.8(B) shows such a transition for the 2^{nd} order mode.

The RI sensitivity, S_{RI}, of the above sensor structure is given in Fig. 3.9. Whereas the sensitivity for the 1^{st} order mode increases monotonically with the increased wall thickness, the sensitivity for the 2^{nd} and 3^{rd} order modes oscillates significantly. In particular, S_{RI} becomes nearly zero at certain regions that correspond to the plateaus in Fig. 3.8(A), where the mode possesses the dominant characteristic of the wall mode (*e.g.*, the mode in the second figure of Fig. 3.8(B)). After the de-coupling process, all modes approach their respective maximal sensitivity. The thickness sensitivity, S_t, is generally

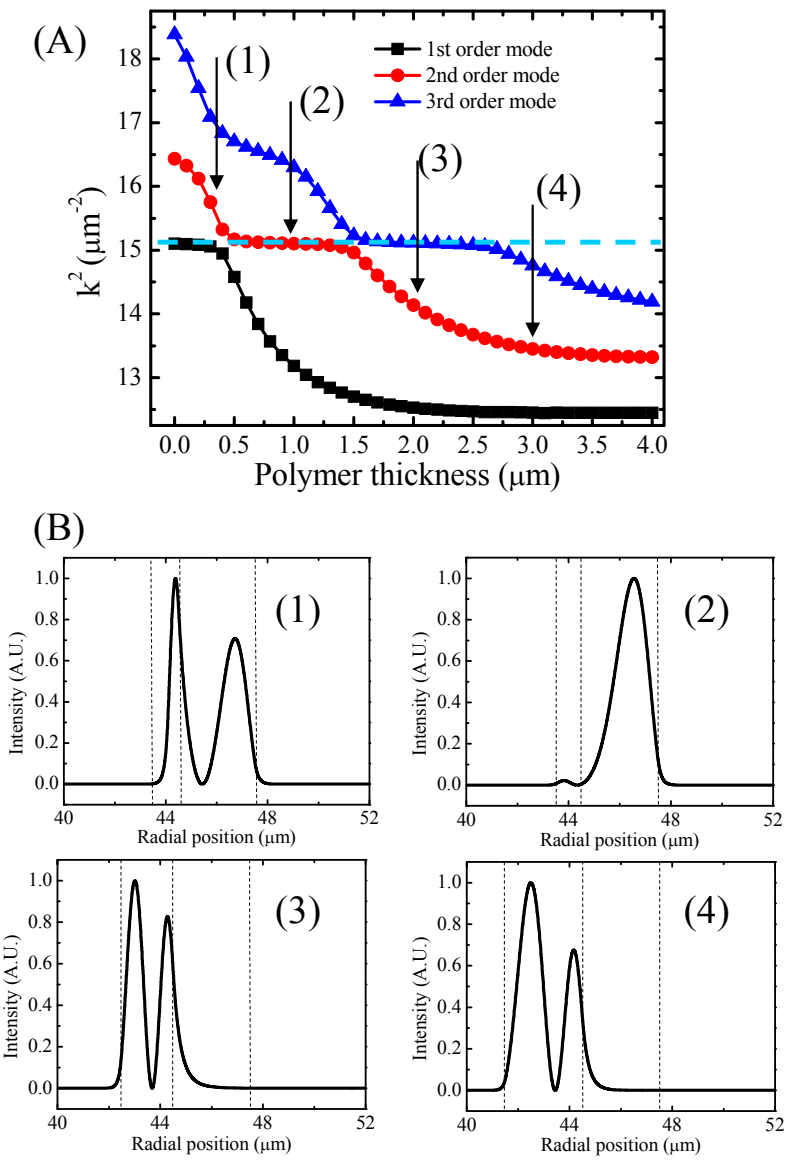

Fig. 3.8 (A) k^2 as a function of polymer thickness for the first three WGMs. *Dashed line* indicates the k^2 position for the first-order ring resonator wall mode in the absence of the polymer layer. The simulation parameters are the same as in Fig. 3.6, except that the polymer RI, n_2, is 1.7. (B) The WGM radial distribution of the second-order mode for various polymer thicknesses indicated by the *arrows* in (A). *Vertical lines* indicate the boundaries of the ring resonator wall and the polymer layer. Reprinted from Ref. [134] with permission.

positive. However, at the region of plateau in Fig. 3.8(A), it becomes nearly zero, meaning that the OFRR sensor is insensitive to any polymer change induced by chemical vapors.

3.4.3 Discussion

3.4.3.1 Limit of Detection

The LOD of the ring resonator vapor sensor is determined by its sensitivity and its minimally resolvable spectral shift $(\delta\lambda)_{m,}$ *i.e.*:

$$DL = \frac{\delta\lambda_m}{S} \tag{3.5}$$

$(\delta\lambda)_m$ is usually chosen to be 1/20 – 1/50 of the WGM resonance linewidth [48], which

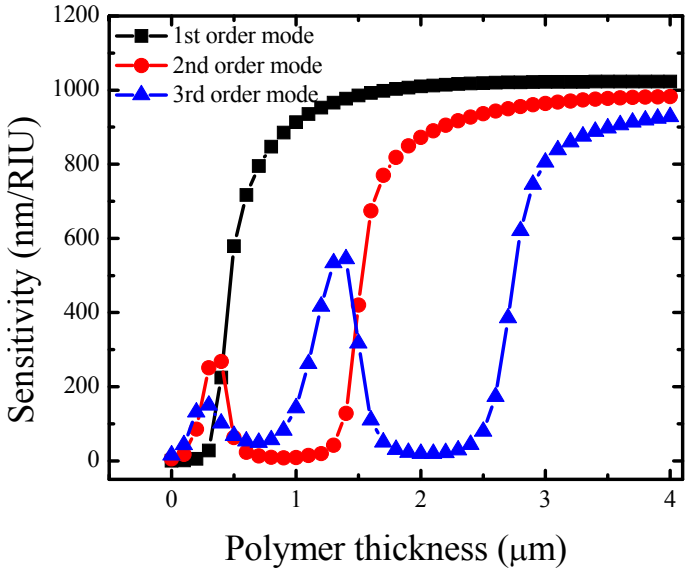

Fig. 3.9 RI sensitivity as a function of polymer thickness for the first three WGMs. The polymer is coated on the inner surface of the ring resonator. The simulation parameters are the same as in Fig. 3.7, except that the polymer RI, n3, is 1.7. Reprinted from Ref. [134] with permission.

inversely proportional to the ring resonator's Q-factor given by [88]:

$$Q = \frac{2\pi n}{\lambda \sigma \eta}, \tag{3.6}$$

where σ is the polymer optical attenuation coefficient. It should be emphasized that although a thicker polymer layer may result in a higher sensitivity (*e.g.*, a larger S_{RI}), it does not necessarily lead to a better LOD, as polymers typically have a much larger attenuation coefficient than fused silica wall. Excessive exposure of the WGM in the polymer layer may significantly degrade the WGM Q-factor and hence the LOD. Therefore, for those polymer ring resonators formed on a chip (the second configuration) and those formed by coating the exterior surface of a microsphere/cylinder with a thick polymer layer (the third configuration), their LOD may not be optimal.

We now apply our simulation results to analyze the performance of the OFRR based vapor sensor, assuming that the doping effect is dominant. Considering that a 1 μm thick polymer layer with RI of 1.47 is coated on the OFRR inner surface and using the parameters given in Fig. 3.6(B), a RI sensitivity of approximately 400 nm/RIU for the 3rd order WGM can be obtained. Further assuming that the polymer absorption loss is 1 dB/cm, which is equivalent to an attenuation coefficient σ = 0.23 cm^{-1}, and using Eq. (3.6), we achieve Q = 5x10^5, at λ = 1550 nm, n = 1.45, and η = 50%. Although practically the Q-factor of the ring resonator could be degraded due to the roughness of the coating, a relatively high Q-factor can still be obtained. In fact, a Q-factor over 10^6 has been demonstrated with a 1.5 μm thick polymer coating on the inner surface of a ring resonator [146]. Assuming that we are able to resolve 1/50 of the resonance linewidth [49] and that the temperature induced WGM spectral fluctuation can be controlled below 0.1

pm at 1550 nm, we arrive at a sensor spectral resolution of 0.1 pm, which has also been experimentally demonstrated recently [133]. As a result, the sensor LOD is estimated to be 2.5×10^{-7} RIU.

Equation (3.4) relates the RI change in the polymer layer to the vapor molecule density in the polymer matrix, which is further related to the vapor concentration in free space, ρ_0, by $K = \rho / \rho_0$, where K is the partition coefficient ranging from a thousand to hundreds of thousand [147, 148]. Using K = 1000 and $N_A\alpha/(3\varepsilon_0) = 30$ cm^3/mol (N_A is the Avogadro's number), which are typical for many types of vapor molecules [127], we have $\delta(n_2) = 2.4 \times 10^{-6}$ RIU/ppm at room temperature and the atmospheric pressure. This result is close to the experimental data [127, 133]. Using the LOD of 2.5×10^{-7} RIU for RI, we obtain a concentration LOD of 0.1 ppm for chemical vapors.

For the polymer thickness induced WGM shift, we use the same parameters as in the previous discussion (*i.e.*, t=1 μm and the 3rd WGM) and assume that the thickness swelling coefficient is 10^{-6}/ppm [144, 145], which results in a 0.03 pm/ppm in the WGM shift based on the simulation in Fig. 3.6. Further using the 0.1 pm spectral resolution, we arrive at a LOD of 3.3 ppm for chemical vapors. Note that in practice, both polymer swelling and the RI change may co-exist and their relative contribution to the WGM shift may vary, depending on the polymer and its interaction with the analyte. However, the derivation discussed above should still be valid.

3.4.3.2 Sensor response time

In the previous section, the sensitivity and the LOD are deduced based on the assumption that the vapor molecules is fully adsorbed by the whole polymer layer and

reaches equilibrium with the polymer. However, for rapid vapor detection and gas chromatography, the diffusion time for vapor molecules to reach the location in the polymer with the highest light intensity need to be taken into account in sensor development. Typically, the diffusion constant for vapor molecules is on the order of $10^{-10} - 10^{-12}$ cm^2 s^{-1} [127, 148]. Therefore, it takes tens of seconds for the detection signal to achieve its saturation value [127]. Sensitivity may have to be compromised for quick detection. For example, when the polymer thickness is reduced to 0.5 μm from 1 μm, the diffusion time will be shortened by 4 times, but in the meantime, the RI sensitivity presented in the previous section will drop to 200 nm/RIU (see Fig. 3.6(B)). This problem could be mitigated by using a high RI polymer. With the same 0.5 μm thickness, a RI sensitivity of nearly 600 nm/RIU is achieved (Fig. 3.9), provided that the diffusion constant remains unchanged. A polymer with a high partition coefficient may also be used for a higher vapor density in the polymer matrix.

3.5 Conclusion

In this chapter, we have developed an OFRR based vapor sensor, which exhibits fast detection and recovery time with a flow rate of only 1 mL/min. The fast response is credit for the OFRR's excellent build-in microfluidics that can deliver the gas sample to the sensor head efficiently without any dead volumes. Detection of two representative chemical vapors, ethanol and hexane, were studied experimentally, with a linear dosage curve established using two different polymer coatings. The LOD for ethanol vapor is around 200 ppm in terms of concentration. Theoretical analysis shows that the RI LOD of

the OFRR is over ten times better than the existing ring resonator technology, which can further be enhanced with a thicker polymer layer at the cost of sensor response time.

Additionally, we used the four-layer Mie model to study the OFRR gas sensing performance and carried out systematic theoretical analysis of sensor sensitivity towards sensor physical structure and polymer coating. The results are meaningful not only to OFRR gas sensor design, but to other optical RI based gas sensors as well.

Future work will be carried out to improve the detection sensitivity while maintaining the fast response time. Packing OFRR capillaries into a PDMS chip to build sensor arrays would also be important in practical application, especially in environmental monitoring where large-scale and distributed sensing scheme is needed. Furthermore, different kinds of polymers can be used to coat OFRRs, and thus to generate patterned response towards individual vapors to improve the sensing specificity.

Chapter 4

OFRR Micro-Gas Chromatography

4.1 Introduction and motivation

In Chapter 3, we have demonstrated that the OFRR is an excellent platform for the development of fast response optical vapor sensors. However, the most significant drawback with the RI detection is the lack of the detection specificity. Although different kinds of sensing polymers can provide certain selectivity towards VOCs according to their molecule polarity, volatility, molecular structure, and functional groups, the RI-based chemical vapor sensors are not able to specifically identify the chemical vapor compounds. In practical applications such as monitoring environmental pollutants, assessing human exposure to toxic chemicals, diagnosing diseases, and detecting chemical threats in the battlefield, it is crucial for the sensor to selectively detect low concentrations of target analyte out of complex vapor mixtures. This is a challenging task for OFRR vapor sensors because the polymer will respond to almost all VOCs and produce WGM spectral shift unbiased.

To solve this problem, we combine the ring resonator sensing technology and the GC technology to selectively and rapidly identify target vapor analyte out of complex interfering vapor mixtures. GC is a well-established and powerful analytical tool that has high selectivity in analyte detection. In GC, the selectivity is achieved by separating the vapor mixture into individual vapor analytes through long separation columns and

recognizing each analyte at the end of the column through their unique retention times [149]. However, bench-top GC is large, power intensive, and requires long analysis times. These factors have significantly hindered its deployment as a portable technology for field applications. Therefore, significant efforts have been invested to develop and test the portable GC systems. Research on micro-GC (μGC) analyzers over the past ten years has shown great potential for analyzing multi-VOC mixtures of arbitrary composition [150-153].

In this chapter, we will investigate and develop a unique μGC system based on OFRR for direct on-column detection of vapor VOCs. The implementation of OFRR-based μGC system will be presented, followed by using the system in separation and detection of 2,4-dinitrotoluene (DNT), an indicator of the existence of explosives such as 2,4,6-trinitrotoluene (TNT), out of interfering vapor mixtures. To improve the chromatographic resolution (or separation resolution) of the μGC system, we further study a tandem-column setting with OFRR μGC, and demonstrate separation and detection of 12 analytes with various volatilities and polarities within 4 minutes.

4.2 Design and implementation of OFRR micro-GC system

4.2.1 Concept of the OFRR μGC

To better understand the OFRR μGC, we will first introduce the working principle of the regular bench-top GC. In a GC system, as illustrated in Fig. 4.1(A) and (B), a mixture of vapor analytes is introduced into the gas injector, often heated at high temperature, and then released as a pulse carried by the inert carrier gas that travels along

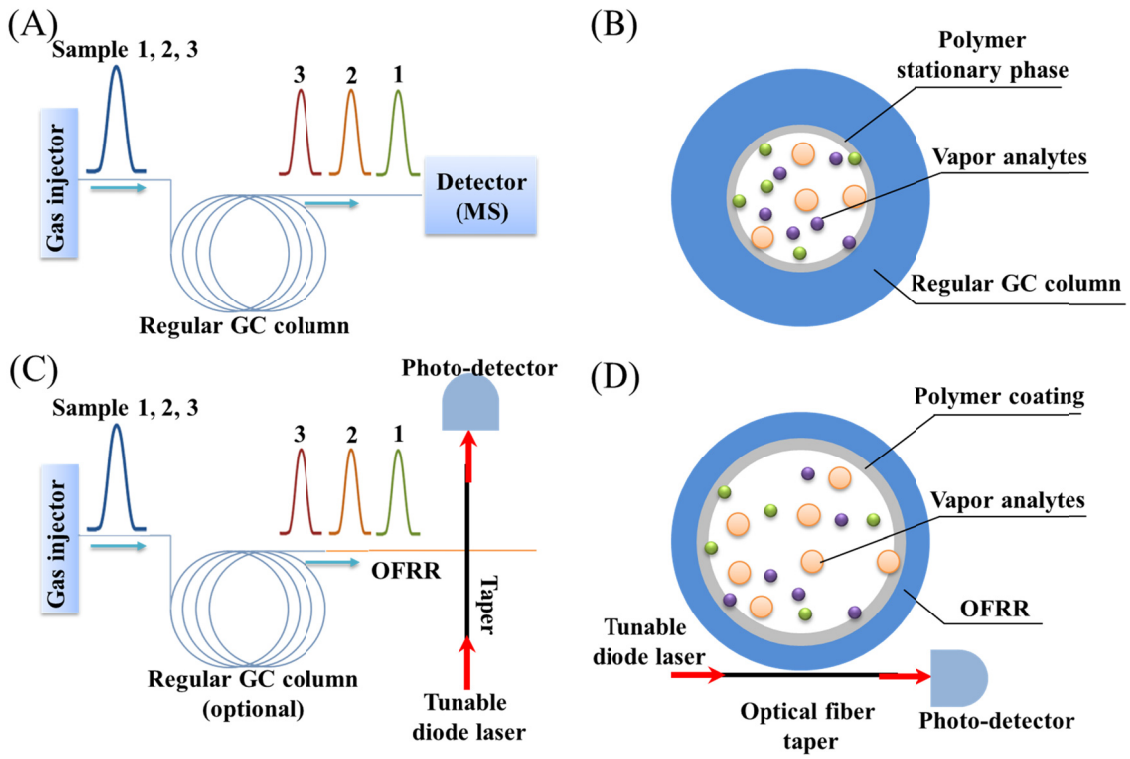

Fig. 4.1 (A) Conceptual illustration of a regular GC setup. (B) Cross-sectional view of a regular GC column. (C) Conceptual illustration of the OFRR-based μGC setup. (D) Cross-sectional view of the OFRR.

the GC column coated with a layer of polymeric stationary phase. Vapor molecules partition between the carrier gas (the mobile phase) and the stationary phase within the GC column. After components of the mixture move through the GC column, they reach a detector, *i.e.*, mass spectrometry (MS). Ideally, components of the mixture will reach the detector at varying times due to differences in the partitioning between mobile and stationary phases. Therefore, by monitoring the elution time (or retention times) at the end-column detector, each component in the sample mixture will be uniquely identified on the chromatogram. The area under the peak on the chromatogram is proportional to the quantity of one component in the vapor mixture. To achieve optimal separation, it is important to select the GC column with proper stationary phase according to the sample

analyzed. As illustrated in Fig. 4.1(B), the GC column is a thick-walled glass capillary, coated with polymer (100-200 nm) inside of the column as the stationary phase. The column inner diameter (ID) is usually around 100-250 μm.

Following the same concept of GC, we developed the OFRR-based μGC system, as shown in Fig. 4.1(C) and (D). In this system, the OFRR has a dual function of separation column and the micro-optical detector. By coating the capillary inner surface with a thin layer of polymer as stationary phase, OFRR is essentially a GC column, capable of separating vapor mixture according to the interaction of chemical compounds and the stationary phase. The only difference between the OFRR and regular GC column is that OFRR has a thin wall (< 4 μm). However, wall thickness does not affect the separation process. Additionally, the cross section of the OFRR forms a high-Q micro-ring resonator, which responds quantitatively to chemical vapors flowing through the capillary in real-time, as studied in Chapter 3. Through optical tapered fiber coupling at one location or multiple locations on the OFRR, GC separation column and detectors are naturally integrated into one piece. Since the detection is carried out directly on the GC separation column, in contrast to the end-column detectors used in conventional GC system, our detection scheme is called on-column detection. On-column detection not only provides greater detection flexibility since it is capable of detecting vapor analytes at any locations along the OFRR, but could also provide additional information about co-eluted analytes, which are impossible to be identified by an end-column detector. Furthermore, the OFRR based μGC has a few additional distinct advantages. First, the OFRR serves a dual purpose as both a GC separation column and micro-detector. No additional end-column detectors are needed. Such integration greatly simplifies the μGC

design, thus improving μGC reliability and enabling device miniaturization. Second, as a μGC detector, the OFRR has no internal volume, short rise time, and ultra-low intrinsic noise level. The laser and photo-detector in the OFRR μGC system are potentially capable of operating at a high data acquisition rate (>MHz), which are highly desirable attributes for fast μGC systems. Third, the unique on-column analysis enables detection at any pre-determined locations along the OFRR without interfering with the gas flow inside, which is not feasible with conventional GC detectors that are separated from the column. Fourth, the OFRR is capable of performing multi-point on-column detection by placing tapered fibers at any location along the separation column. Therefore, analytes can be well separated on at least one of the detection locations. Moreover, with multiple detection points on the OFRR column the entire separation process can be monitored. All of these help avoid the complicated and costly modulation procedures and allow for rapid profiling and screening of large varieties of analytes. Fifth, efficient capillary microfluidics and in-situ analyte separation and detection within the same column reduce the fluidic dead volume to a minimum, and thus reduce the band broadening effect along the column. Sixth, the circular cross section of the OFRR is fully compatible with conventional GC columns (see Fig. 10(C)) and related testing equipment without introducing any added dead volumes. Therefore, the OFRR can either be used independently as a separation column and on-column detector or can be used in conjunction with a regular GC column. Seventh, the OFRR based μGC system can be made inexpensively. The fabrication and detection methods are simple and straightforward, and the system can be scaled-up for multiplexed and parallel detection to significantly enhance the separation capability and detection speed.

4.2.2 Demonstration of OFRR μGC concept

To demonstrate the proof-of-concept of the OFRR's separation and on-column detection, several vapor analytes are used as a model system. The OFRR is coated with 100 nm PEG using the static coating method as detailed in Chapter 3. The optical detection scheme is the same as detailed in the OFRR vapor sensing experiments previously, which is also illustrated in Fig. 4.1(C) and (D). The detection is achieved by optical taper coupling of WGMs at a position of 3 cm downstream from the OFRR capillary inlet. In the experiment, a GC injection port (Agilent GC 5890 II) is used to generate the vapor pulse. A short segment (*ca*. 100 cm) of nonpolar deactivated phase fused silica capillary (0.25 mm ID) is used to bridge the injection port and the OFRR capillary inlet. The analytes are sealed individually in 10 mL sample vials. The solid phase microextraction (SPME) fiber with a 65 μm coating of polydimethyl siloxane/divinyl benzene (PDMS/DVB) (Supelco) is exposed to the headspace for different sampling times to pick up proportional amounts of analyte, and then released at a GC injection port that was heated to 250 ^{o}C. Ultra-high purity (UHP) helium is used as the carrier gas at a flow rate of 6.8 mL/min measured at the outlet of the OFRR capillary. The split ratio of vent flow to column flow is 5:1.

Fig. 4.2 shows the chromatograms of toluene/decane (Fig. 4.2(A)), decane/dodecane (Fig. 4.2(B)), hexane/decane (Fig. 4.2(C)), and toluene/DMMP (Fig. 4.2(D)). All the analytes could be well-separated at room temperature. Toluene, hexane, and decane vapors have a rapid response, with a peak width of sub-second. The rise time for DMMP is 1.25 seconds and it has strong tailing effect due to the strong interaction of DMMP and polar PEG coating. Additionally, the residual active sites in the OFRR

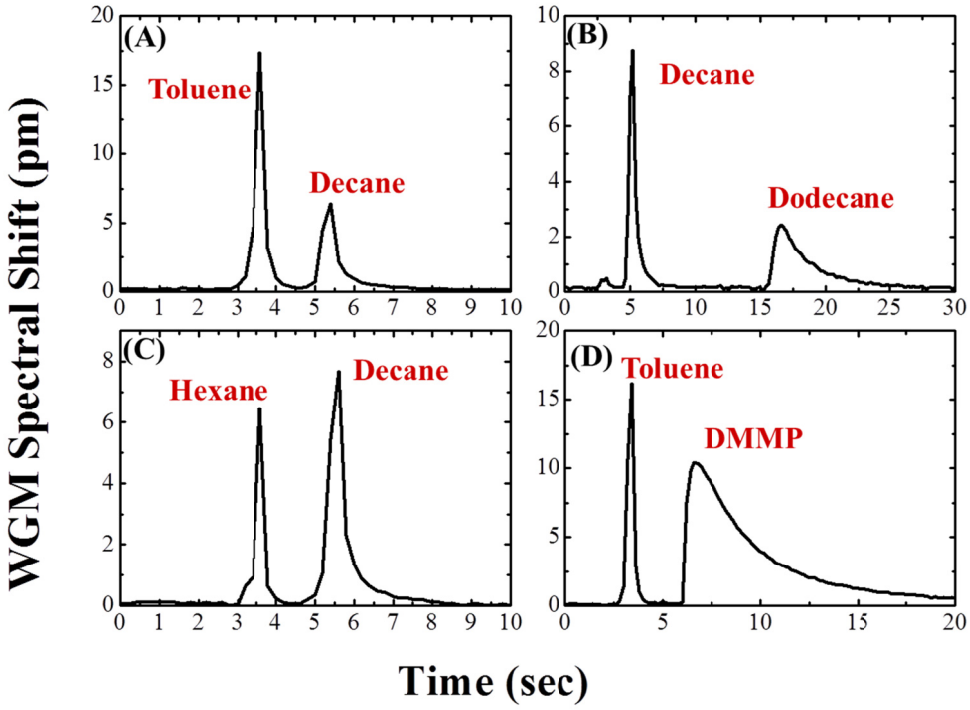

Fig. 4.2 Separation and detection of different analytes with a PEG-400 coated OFRR μGC

column may also increase the tailing effect, since compared to commercial GC columns, our column coating procedure does not introduce the surface deactivation layer between the polymer coating and the glass surface. Dodecane has a relatively low response time of 2 seconds because of the low volatility at room temperature. This experiment clearly shows efficient separation and rapid on-column detection can be achieved through several centimeters long OFRR capillary. The ability to separate samples over a short distance is enabled by the small ID of the OFRR.

4.3 Rapid explosive vapor detection

Detection of explosives is a challenging task for the development of portable vapor sensors due to their extremely low volatility. Several methods have already been demonstrated with ultra-high sensitivity towards the common explosive compounds, such as DNT, TNT, PETN, and RDX [109, 154-156]. For the pure analyte sample, where only a single analyte is present, the detection limit can be pushed down to the sub-part-per-billion (ppb) level. However, for practical applications, especially in the battlefield, at airport security checkpoints, and for air monitoring with counter-terrorism purpose, it is crucial for the sensor to discriminate the trace level of explosive substances out of other usually more volatile interferences in the air. This is very challenging for most of the miniaturized portable vapor sensors because they typically rely on polymer coatings to provide certain selectivity. When the explosive substances are mixed with volatile interferences, the signal from explosives is prone to be buried in the background, which would cause false positives. In the aim of developing a portable gas analyzer with high sensitivity, high specificity, and rapid response, we study the OFRR μGC analyzer for explosive detection. DNT is chosen as a model system, because its chemical structure is similar to TNT while its significantly higher volatility facilitated testing. Also, DNT is present in some explosives and is usually used as an indicator to predict the existence of TNT.

4.3.1 Experimental setup and condition

The experimental setup and optical detection scheme has been detailed in the chemical vapor sensor experiments in Chapter 3.

The OFRR used in the experiment is coated with 3 mg/mL PEG 1000 to yield an average thickness of 60 nm. The OFRR used is 3.5 cm in length and the detection position is approximately one centimeter from the OFRR inlet, which is connected to a GC injection port through a nonpolar deactivated phase fused silica capillary (0.25 mm ID, 35 cm in length) wrapped in a transfer line, which is heated to approximately 65 ^{o}C to avoid DNT condensation. The OFRR and fiber optic taper are covered with a homemade plastic module to reduce the thermally induced fluctuations in the WGM spectral position caused by surrounding air flow. All experiments are carried out at room temperature (~ 20 ^{o}C), unless otherwise specified.

The analytes (DNT, nitrotoluene, or TEP) are sealed individually in 10 mL sample vials. The SPME fiber is exposed to the headspace for different sampling times to pick up proportional amounts of analyte, and then released at a GC injection port that is heated to 250 ^{o}C. UHP helium is used as the carrier gas at a flow rate of 10.6 mL/min measured at the outlet of the OFRR capillary.

4.3.2 Results and discussion

Real-time detection of 2,4-DNT vapor

Fig. 4.3 shows the real-time response of the PEG 1000 coated OFRR sensor upon injection of DNT. The WGM starts to shift to a longer wavelength around 20 seconds after injection, and reaches its peak value around 40 seconds. The signal completely returns to baseline quickly afterwards, indicating that the polymer is completely regenerated for the following sensing activities. A single sensing event is accomplished

within only one minute at room temperature, showing great promise for detecting explosives in a rapid and simple manner.

Fig. 4.4 plots the WGM spectral shift of the OFRR used in Fig. 4.3 (OFRR #1) in response to various SPME extraction times. To further characterize the variations in the OFRR sensitivity, another OFRR (OFRR #2) is made and tested. An excellent linear response is observed for both OFRRs. Furthermore, the OFRR showe good repeatability in the WGM spectral shift for a given DNT mass. However, a relatively large variation is present in the OFRR sensitivity (0.41 pm/ng and 0.67 pm/ng for OFRR #1 and #2, respectively), which can be attributed to the variations in the OFRR fabrication process that might result in different wall thickness [134]. To estimate the detection limit of the

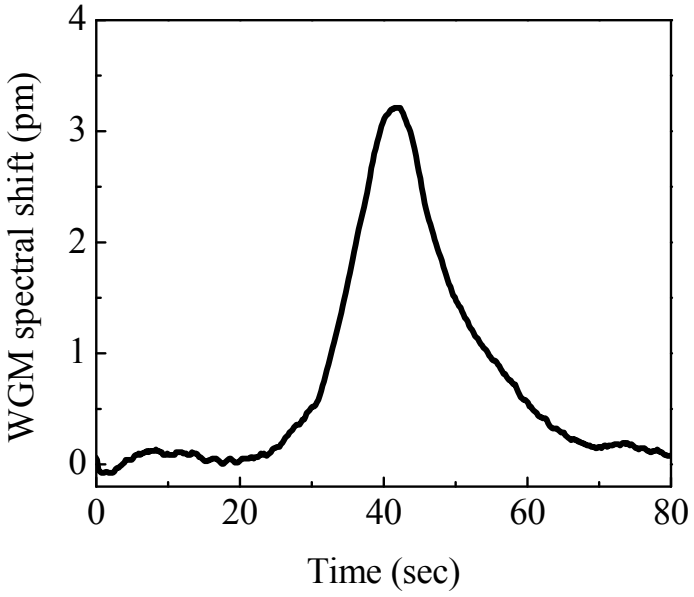

Fig. 4.3 Temporal response of the OFRR vapor sensor upon injection of DNT vapor. Peak position = 41 seconds. Peak width = 13.6 seconds. DNT is extracted by SPME from equilibrium headspace of a vial containing DNT powder at room temperature. SPME extraction time = 40 seconds. DNT is injected at 0 second. Reprinted from Ref. [172] with permission.

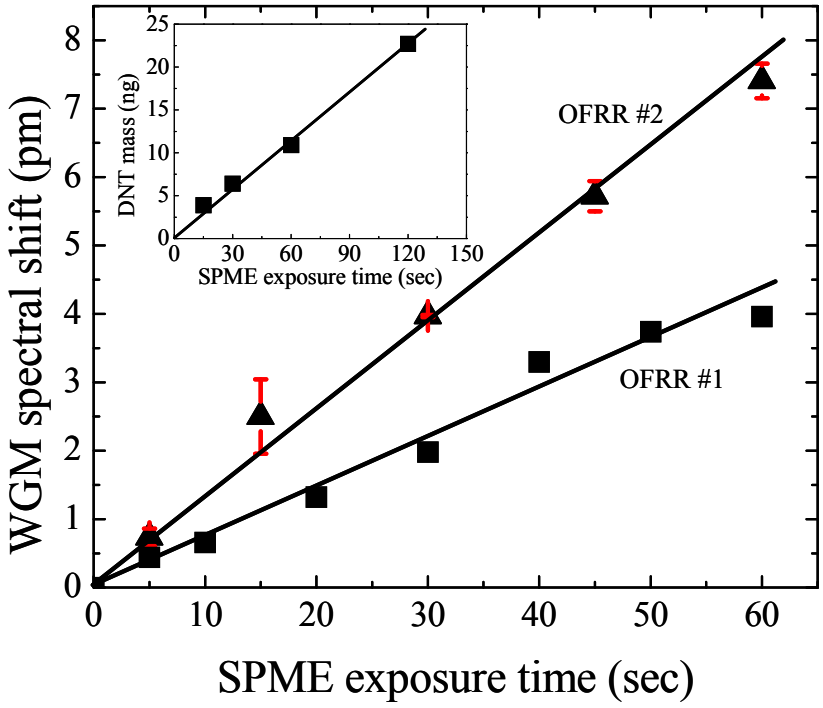

Fig. 4.4 OFRR vapor sensor response to DNT vapor samples extracted with various SPME sampling times at room temperature. The sensitivity for DNT is estimated to be 0.41 pm/ng and 0.67 pm/ng for OFRR #1 and #2, respectively. The error bars represent standard deviation obtained from three measurements with OFRR #2. Inset: Calibration curve obtained with a GC/MS system (Varian) for the mass of DNT extracted by the SPME fiber under various extraction times at room temperature. Reprinted from Ref. [172] with permission.

OFRR vapor sensor for DNT, we used a WGM resolution of 0.15 pm (3 standard deviations) [132], which results in a detection limit of approximately 200- 300 pg for DNT vapor, corresponding to about one second of SPME extraction time at room temperature.

Identification of DNT out of vapor mixtures

In many chemical vapor sensors for explosive detection, a polymer is used to capture and recognize the target explosive molecules. Since nitro groups in explosive

compounds are great electron acceptors, a wide range of sensing polymers acting as electron donors have been designed to recognize explosives. However, these polymers experience challenges in detection selectivity because they will respond to interferents in real analyte samples, especially those that also contain the nitro group or other electron acceptors, which would cause false positives.

OFRR vapor sensors are able to differentiate the target explosive analyte out of a series of interfering analytes in the vapor mixture by monitoring the WGM wavelength shift in real time. Different analytes will have unique retention times according to their affinity towards the polymer as well as volatility difference. Fig. 4.5(A) shows the separation between DNT vapor and nitrotoluene vapor using OFRR #1. Although nitrotoluene and DNT only have one nitro group difference in structure, OFRR vapor sensors achieved very efficient separation between them. Since the retention time is used as a unique criterion to provide additional selectivity, it is crucial to ensure the repeatability from one injection to another. We test separation between nitrotoluene and DNT vapor mixtures with various mass ratios for numerous times and all the data showe consistent retention times. In addition, the signal amplitude is proportional to the extraction time of the SPME fiber in equilibrium headspace. In Fig. 4.5(B), we further show the highly reproducible and highly specific detection of DNT from a mixture containing three different analytes. The four traces not only demonstrate the separation capability among analytes that have relatively big difference in retention times, such as nitrotoluene and DNT, but also show excellent separation efficiency in analytes that have similar interaction with the polymer, indicated by the well resolved peaks with one second retention time difference between nitrotoluene and TEP.

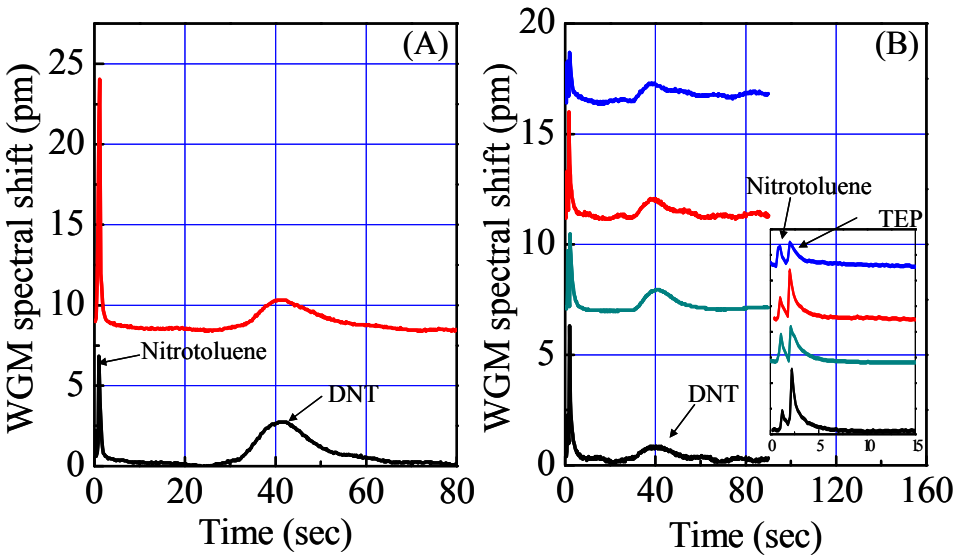

Fig. 4.5 Highly repeatable detection of DNT using OFRR #1 from interference background. (A) Separation and detection of DNT from nitrotoluene/DNT mixtures. SPME extractions are performed at room temperature. Curves are vertically shifted for clarity. Top curve: Nitrotoluene extraction time = 3 seconds, DNT extraction time = 20 seconds. Bottom curve: Nitrotoluene extraction time = 1 second, DNT extraction time = 30 seconds. (B) Separation and detection of DNT from nitrotoluene/TEP/DNT mixtures. SPME extractions are performed at room temperature. Extraction time for each analyte is varied among four operations. Curves are vertically shifted for clarity. Inset shows the details of the first 15 seconds. Reprinted from Ref. [172] with permission.

Effects of polymer thickness and temperature

Both polymer thickness and OFRR working temperature play an important role in the sensor performance. Fig. 4.6(A) shows the WGM response to DNT from an OFRR coated with 200 nm PEG 1000 working at room temperature. As compared to the one with a 60 nm polymer coating shown in Fig. 4.3, the temporal response peak position is significantly delayed to 240 seconds with a much more broadened peak width. In addition, the response curve has a strong tailing effect, which significantly deteriorates the sensor

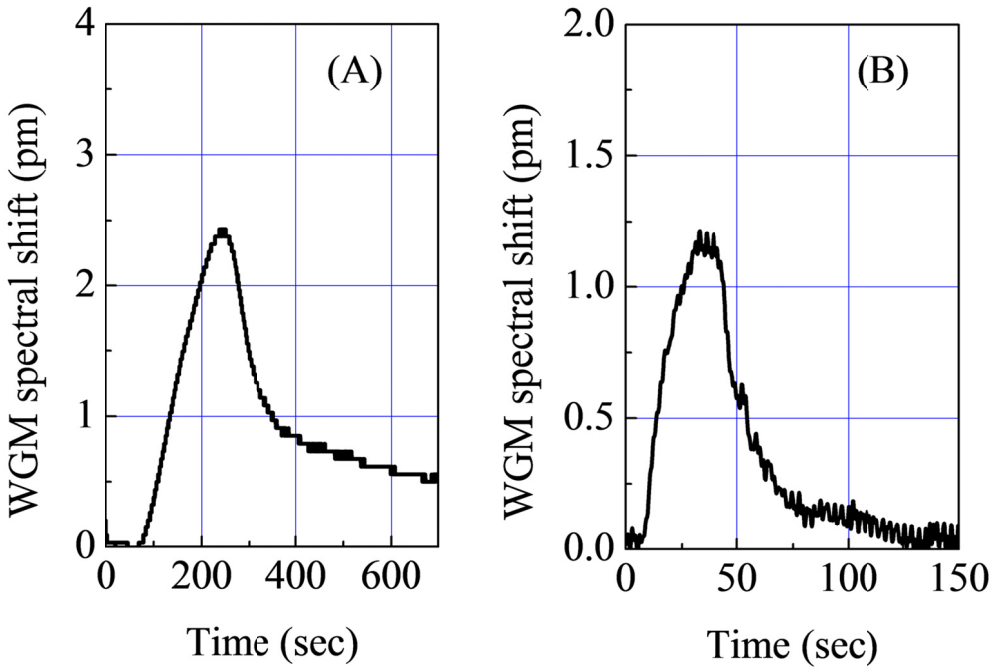

Fig. 4.6 Response of the WGM to DNT when the polymer coating thickness is 200 nm. (A) The OFRR is at room temperature. DNT mass injected ≈ 400 ng. Peak position = 240 seconds. Peak width = 150 seconds. (B) The OFRR is at 65 oC. DNT mass injected ≈ 400 ng. Peak position = 34 seconds. Peak width = 33 seconds. Reprinted from Ref. [172] with permission.

regeneration capability. However, when the OFRR is heated to a higher temperature (*e.g.* ~ 65 ^{o}C), the response peak, shown in Fig. 4.6(B), emerges at a much earlier time with a narrower peak width, since the DNT becomes more volatile at this temperature. Also the WGM returns to baseline, indicative of regeneration of the polymer. Regarding DNT sensitivity, however, in comparison to Fig. 4.6(A), the WGM spectral shift at higher temperature decreases. This decreased response is expected since the partition coefficient for the vapor absorbed into the stationary phase polymer coating decreases with increasing temperature. Therefore, for explosive detection, it is critical to tailor the

polymer coating thickness as well as the OFRR operating temperature to obtain an optimized sensitivity and time response.

4.3.3 Theoretical analysis

The DNT detection process can be analyzed using a Mie model in conjunction with the effective medium model that accounts for the RI change induced by the embedded analyte molecules in the polymer matrix [127, 134].

First, we need to estimate the DNT molecule density in the polymer layer, ρ_2,

$$\rho_2 = [\frac{KV_1}{V_1 + KV_2}] \cdot \rho_0 , \tag{4.1}$$

where V_1 and V_2 are the DNT vapor phase volume in the OFRR capillary and the polymer volume, respectively. ρ_0 is the initial DNT molecule density in the vapor phase, and K is the partition coefficient. Although K is unknown between DNT and PEG 1000, it is reasonable to assume K = 60 based on the studies performed on TNT extraction using a SPME fiber [157]. V_1 and V_2 can be estimated by considering the length of the DNT plug travelling in the OFRR, the dimensions of the OFRR, and polymer thickness. While the mobile (gas) phase has a large linear velocity, which is about 28 m/s in our experiment, DNT travels at a much slower speed due to the strong interaction with the polymer. Using the retention time in Fig. 4.3 and the distance between the OFRR inlet and the detection position, the DNT speed can be estimated to be 0.025 cm/s, which translates to a DNT spread of 0.34 cm along the OFRR capillary by using 13.6 seconds of the DNT peak width. As a result, $V_1 = 2.1 \times 10^{-11}$ m^3 and $V_2 = 5.8 \times 10^{-14}$ m^3, and subsequently $\rho_0 = 0.26$ mol/m^3 and $\rho_2 = 13.4$ mol/m^3 can be obtained for 1 ng of DNT injected.

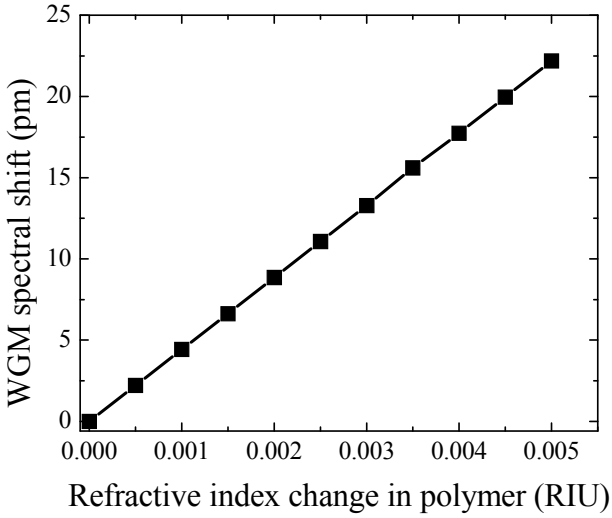

Fig. 4.7 Calculated WGM spectral shift as a function of the RI change in the polymer layer using a four-layer Mie model with OD = 90 μm, wall thickness = 3 μm, and polymer thickness = 60 nm, The sensitivity is 4.3 nm/RIU. Reprinted from Ref. [172] with permission.

The RI change in the polymer layer, Δn, due to the DNT molecules embedded in the polymer can be estimated using the effective medium model or Lorentz-Lorenz model [127, 134]:

$$\Delta n = \frac{(n_{polymer}{}^2 + 2)^2}{6 \cdot n_{polymer}} \times [\frac{N_A \alpha}{3\varepsilon_0}] \cdot \rho_2 , \tag{4.2}$$

where α is the vapor molecule polarizability, $n_{polymer}$ (*e.g.*, 1.47 for PEG) is the RI for the polymer layer, N_A is Avogadro's number, and ε_0 is the dielectric constant for vacuum. Using $N_A\alpha/3\varepsilon_0 = 4\text{x}10^{-5}$ m^3/mol for DNT [158, 159], we arrive at $\Delta n = 1\text{x}10^{-3}$ RIU for 1 ng of DNT.

The OFRR sensitivity can be simulated using a four-layer Mie model that includes the air core, polymer layer, OFRR wall, and the surrounding air, as detailed in Chapter 3. Fig. 4.7 plots the linear WGM spectral shift as a function of the RI change in

the polymer layer, using the OFRR OD of 90 μm, the wall thickness of 3 μm, and the polymer thickness of 60 nm. The sensitivity based on the slope in Fig. 4.7 is approximately 4.3 nm/RIU, which further leads to a sensitivity for DNT of 4.3 pm/ng. This result is approximately 10 times higher than that obtained experimentally (0.41 pm/ng). The discrepancy can be attributed to the lack of detailed information about the OFRR wall thickness, the polymer thickness, and the partition coefficient in theoretical analysis, and the possible analyte loss at the connectors and along the column during the experiment.

4.4 Tandem-column micro-GC

4.4.1 Motivation

Although research on μGC analyzers over the past ten years has shown great potential for portable, rapid, and low power consumption μGC systems [150-152, 160-166], due to the limited length of the separation columns employed (usually one meter), it suffers an inherent constraint with regard to separation resolution; multiple analytes may co-elute at the end of the short column, which limits the complexity of the mixtures it can effectively analyze.

In order to maintain fast separation while improving the selectivity, a μGC system consisting of coupled tandem columns coated with different stationary phase has been proposed [167-169]. In this system, a nonpolar or slightly polar phase column is usually used as the first separation column, followed by a short polar phase column. Analytes are basically separated according to their volatility on the first column and then further

separated according to their polarity on the second column, resulting in greatly increased separation power. In a typical tandem-column μGC setup, an adjustable pressure control valve is used at the tandem-column interface to address the co-elution problem occurring at the end of the tandem-column. The valve tunes the carrier gas velocity, hence the analyte retention, in both columns, with each set of retention combination being employed to avoid co-elution of a specific set of analytes in the sample [151, 161, 162, 170, 171]. Although enhanced selectivity is achieved, the valve operation is sophisticated and the sample needs to be tested several times under different retention conditions in order to separate all the chemical compounds in it.

In this chapter, we will study OFRR-based tandem-column μGC system to improve the separation resolution. Due to OFRR's unique multi-point on-column detection capability, the tandem-column separation can be employed in a simple manner, without using valve or modulator at the interface of the two columns. We will use twelve representative analytes with various volatilities and polarities to demonstrate the performance of tandem-column separation of the OFRR based μGC system. Further, we will demonstrate the system's capability of on-column monitoring of the separation process for the target analyte in a vapor mixture.

4.4.2 Experimental setup

A schematic of the experimental setup of the OFRR-based tandem-column μGC system is shown in Fig. 4.8. As illustrated in Fig. 4.8(A), the first column (180 cm) is a conventional low polarity GC column, followed by a second, relatively short (~ 10 cm), home-fabricated OFRR column coated with a polar stationary phase. Two detection

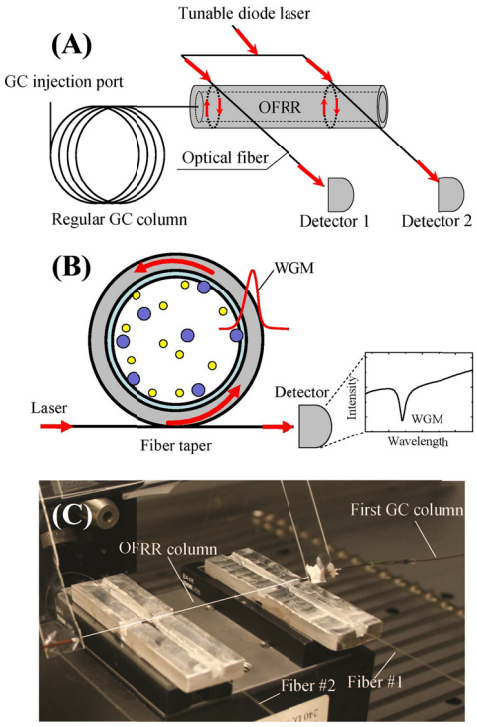

Fig. 4.8 (A) Conceptual illustration of tandem-column separation based on OFRR μGC. A nonpolar phase regular GC column is connected with a relatively short polar phase coated OFRR column through a press-tight universal connector. A tunable diode laser is coupled into two fibers in contact with the OFRR. The first fiber is placed at the inlet of the OFRR and the second one a few centimeters downstream along the OFRR, defining two detection locations, respectively. (B) Cross sectional view of the OFRR. The WGM is excited through the fiber perpendicularly in contact with the OFRR and circulates along the circumference of the OFRR. The WGM spectral position changes in response to the interaction between the polymer coating and vapor molecules. (C) A picture of the OFRR with two tapered fibers separated by approximately 6 cm. A white line is drawn along the OFRR column to guide the eye. Reprinted from Ref. [38] with permission.

locations are chosen, one at the inlet of the OFRR, right after the first column, and the other one a few centimeters away from the first detection point, to monitor the separation in the first column and the second column, respectively. Since OFRR on-column detectors record the retention time independently and provide complementary chromatograms for each chemical compound, co-elution at the terminal end of columns is no longer an issue for the OFRR based tandem-column μGC. By monitoring retention

times at multiple locations along the OFRR column, analytes can be well separated on at least one detection location. As a result, no complicated and costly modulation at the interface of two columns is required.

The analyte samples are extracted from equilibrium headspace using a SPME fiber with a 65 μm coating of PDMS/DVB (Supelco) at room temperature and then introduced through the GC injection port, which is heated to 250 ^{o}C. The first column consists of a fused-silica capillary with 0.1-mm ID and 180 cm in length. Its interior surface is coated with 0.1 μm nonpolar poly(dimethylsiloxane) bonded stationary phase (Rtx-1) or 0.1 μm slightly polar 5% diphenyl 95% dimethyl polysiloxane (Rtx-5). The second column is an OFRR capillary with a 90 μm OD, 84 μm ID, and 15 cm length. It is coated with a polar stationary phase, PEG 1000, with a coating thickness estimated to be approximately 80 nm. The Rtx-1 (or Rtx-5) column and the OFRR capillary are connected in tandem by a universal quick seal column connector (CP 4787, Varian). A tunable diode laser (JDS Uniphase, center wavelength 1550 nm) is scanned over 110 pm spectral range at a scanning rate of 5 Hz. The laser light is guided by a single-mode fiber and then directed into two branches of tapered fiber through a fiber coupler (Thorlabs, Newton, NJ). The tapered part is approximately 3 μm in diameter and is placed in contact with the OFRR column to excite the WGM, thus defining a detection location. The first tapered fiber is placed at the OFRR column inlet to monitor in real-time the analytes separated by the first column. The second tapered fiber is placed at a location 6 cm away from the first one to monitor the retention time of each analyte separated by both columns. The chromatograms are recorded at these two locations unless otherwise specified. The retention time differences from the two channels indicate the separation of the analyte

along the 6 cm polar-phase coated OFRR column. A photodetector (New Focus 2033) is used at the distal end of each fiber to monitor the output light intensity. When the laser is scanned through a wavelength on resonance with WGM supported by the OFRR, a spectral dip is observed, as shown in Fig. 4.8(B), which could be used to indicate the WGM spectral position. The WGM spectral position changes in response to the analyte passing through the detection point. The data are collected by a data acquisition card (National Instruments NI USB 6211) for post-analysis. UHP helium is used as the carrier gas at a flow rate of 0.86 mL/min. The first column is wrapped in a transfer line maintained at an isothermal temperature of 50 ^{o}C (unless otherwise specified), and the OFRR column is operated at room temperature (~ 23 ^{o}C).

4.4.3 Experimental results and discussion

First-column separation and detection

As illustrated in Fig. 4.8, the first tapered fiber is placed at the beginning of the OFRR capillary column, right after the end of the first traditional Rtx-1 GC column, and is used to monitor the separation achieved by the first column. In order to demonstrate the capability of detecting and monitoring the elution of analyte compounds from the first column in real-time, a vapor mixture of alkanes, including heptane, octane, decane, undecane, and dodecane, is tested. Fig. 4.9(A) shows the retention time of each analyte detected by the two tandem detectors along the OFRR column 6 cm apart. The chromatograms from the first detector show that five alkane analyte peaks are well resolved. Notice that no additional increase in retention time is observed on the second detection channel for the alkanes, which is an expected finding as alkanes have relatively

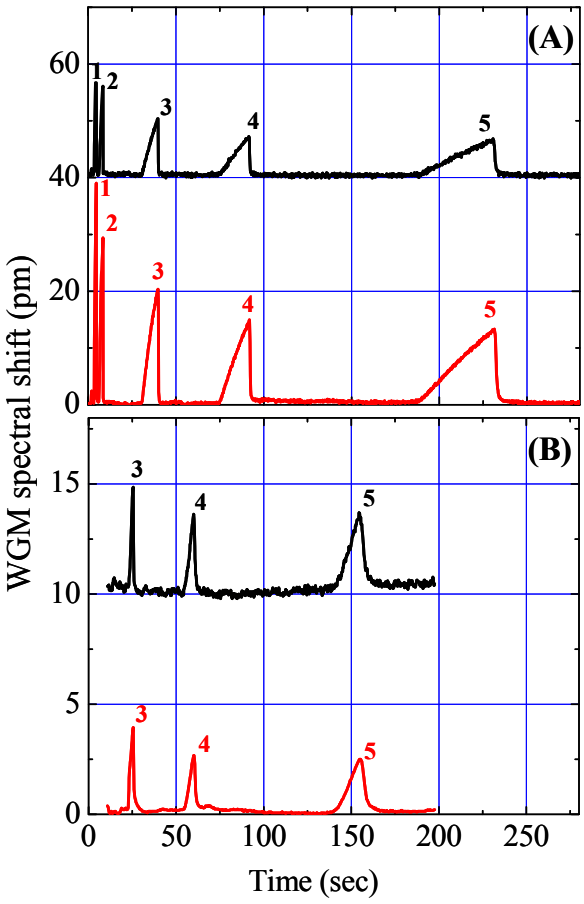

Fig. 4.9 Chromatograms of alkanes. Top trace is recorded by the first detector, showing retention times of each analyte separated by the first Rtx-1 column kept at 50 °C (A) and 150 °C (B) isothermal, respectively. Bottom trace shows the corresponding retention times recorded by the second detector 6 cm away from the first detector. Details of the analytes are listed in Table 4.1. Curves are vertically shifted for clarity. Reprinted from Ref. [38] with permission.

weak interactions with polar stationary phases. The fronting peak profile is caused by overloading the first column. Since the polar stationary phase coated on the OFRR has weak interaction with nonpolar analytes (causing smaller changes in polymer refractive index/thickness), the WGM spectral shift in response to those analytes is usually small, as discussed in our previous work.[133, 134] Consequently, during experiments we inject a significant amount of alkanes into the system in order to obtain a sufficient response from

the polar-coated OFRR, which is in sharp contrast to the highly sensitive response from the same OFRR when the polar analytes were used.[133, 172] Therefore, the OFRR with a polar coating will favorably detect the polar analytes out of nonplar analytes. As discussed later, this unique feature is highly desirable in many applications when the analytes of interest are often highly polar, but mixed with low polarity background interferents (such as alkanes). The insensitive response of the polar-coated OFRR to those low polarity interferents allows us to minimize the effects of the background and single out the trace quantity of polar analytes. Likewise, if sensitive nonpolar analytes detection is needed, the OFRR coated with the nonpolar phase can be used, which will have good rejection towards polar analytes.

In order to improve the alkane peak profile and reduce the fronting effect, we increase the first column temperature to 150 ^{o}C isothermal while leaving OFRR temperature unchanged. In this case, alkanes would have smaller partition into the stationary phase, and therefore become less retained. As expected, the fronting effect is significantly reduced and the chromatogram in Fig. 4.9(B) exhibits more symmetrical and sharper peaks compared to those at isothermal 50 ^{o}C in Fig. 4.9(A). The dodecane peak width measured at the baseline was improved from 44 seconds to 21 seconds. Undecane and decane baseline peak width were only 8 seconds and 3 seconds, respectively. Since heptane and octane analyzed under the elevated temperature become too volatile, they present no adequate separation after traveling through the 180 cm Rtx-1 column, therefore their peaks were not shown in the Fig. 4.9(B).

According to theoretical and experimental studies, the amplitude of the peak (WGM spectral shift) is linearly proportional to the mass of vapor analyte injected.[134,

172] However, in Fig. 4.9(A) the WGM used in the front sensing channel exhibits a lower sensitivity than the WGM used in the back sensing channel since the peak amplitude measured by the first detector was smaller than the one measured by the second detector. WGM sensitivity difference between two channels is possibly due to the OFRR wall thickness difference after etching, PEG coating thickness variation along the capillary, or different order of radial mode used for the measurement.[134, 172] Note that these amplitude differences do not reflect mass differences at two detection locations. In fact, the relative peak amplitudes for all analytes remain the same at both detection channels. In actual applications, a reference sample with known quantity will be used to calibrate the system and the sensitivity difference between the two channels will thus be ratioed out.

Tandem-column separation and detection

The major advantage of tandem-column separation is that all components in a sample will go through two individual separations during one single analysis process and will be analyzed based on their respective volatility and polarity, thus significantly improving the identification, especially for discriminating high polarity analytes from low polarity background species. Fig. 4.10(A) shows that the co-elution of decane and DEMP from the first Rtx-1 column can be very well separated by the PEG 1000 coated 6 cm OFRR column. According to the GC retention index that indicates the relative retention time of alkanes from a nonpolar stationary phase (see Table 4.1), decane and DEMP have the same GC retention index. As a consequence, they are difficult to separate on short nonpolar column. However, during the second separation through the OFRR

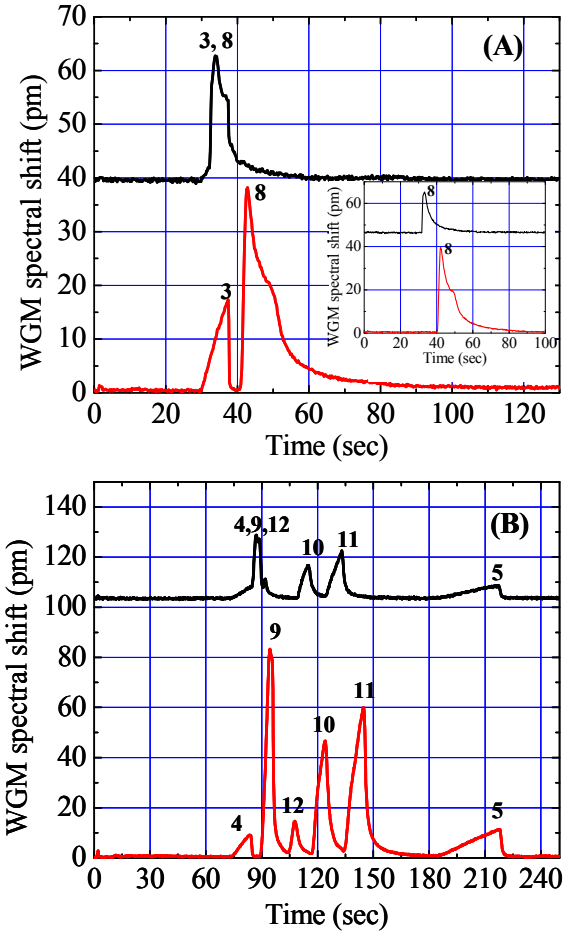

Fig. 4.10 Chromatograms from the two detection channels. The upper trace shows the separation from the 180 cm Rtx-1 column (50 °C) and the lower trace shows the further separation by a 6 cm PEG 1000 coated OFRR column (~ 23 °C). Co-elution of Analyte #3 and #8 in (A) and Analyte #4, #9, and #12 in (B) from the first GC column is well separated by the second OFRR column. The inset of (A) shows the chromatogram for DEMP from the two channels. Curves are vertically shifted for clarity. Reprints from Reprinted from Ref. [38] with permission.

column, the polar analyte DEMP gained an additional 10 seconds in retention as shown in Fig. 4.10(A), whereas the retention time for decane remained the same (see Figs. 4.9(A) and 4.10(A)). To verify that the separation between decane and DEMP indeed took place in the OFRR, the inset of Fig. 4.10(A) plots the chromatogram of DEMP alone from the two channels. In addition, the inset also indicates that the kink right after the main peak

of DEMP might be due to an impurity in the DEMP sample, instead of interference from the decane peak. Fig. 4.10(B) shows the chromatogram of six compounds injected simultaneously. If only separated by the Rtx-1 column, the undecane peak is buried in the stronger peak of 2-NT while DMNB is barely resolved right after the 2-NT peak. Since the three analytes have different polarities, it is clear that after travelling through a 6 cm long OFRR column, all three peaks are well resolved.

Capability of analyzing complex samples

To further demonstrate the tandem-column separation capability of the OFRR

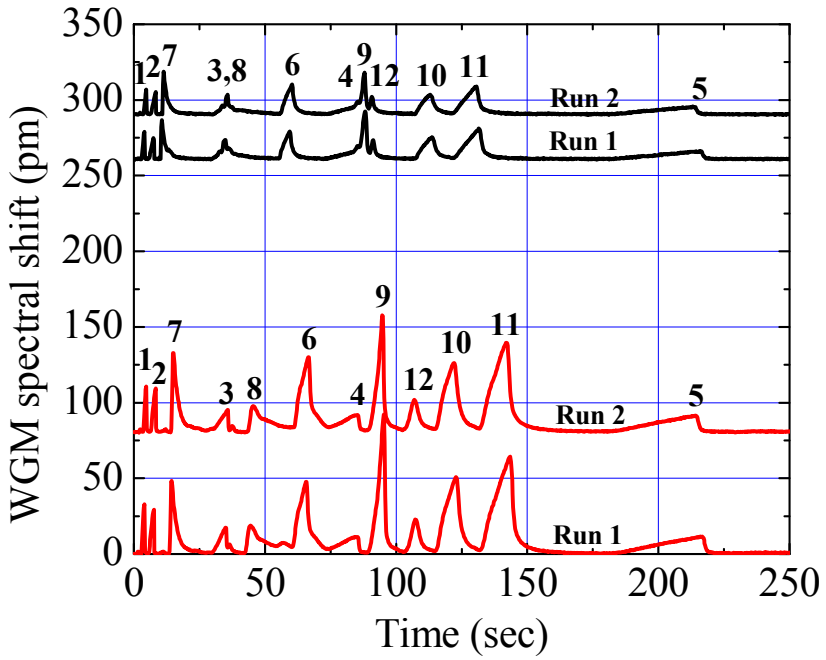

Fig. 4.11 Chromatograms of twelve analytes with various volatilities and polarities obtained by the two detection channels. The whole analysis is completed within four minutes. Two groups of co-elution from the first 180 cm Rtx-1 GC column (50 ^{o}C) (upper trace) are well resolved after the second 6 cm OFRR column (~ 23 ^{o}C) separation (lower trace). The experiments are performed twice (Run 1 and Run 2) to show the separation repeatability. Curves are vertically shifted for clarity. Reprinted from Ref. [38] with permission.

μGC, Fig. 4.11 shows a mixture of twelve compounds that are analyzed by the OFRR μGC system with tandem Rtx-1 column and PEG 1000 coated OFRR capillary column. All twelve compounds are well resolved after tandem-column separation, while two groups of co-elution appeared from the first column separation. Even without optimizing for speed, the analysis time for the twelve compounds is within four minutes, showing great potential for the development of a fast μGC. It is emphasized that while the overloading effect occurred with the nonpolar analytes in Fig. 4.11, it does not obscure the advantages of our system. In fact, the ability to demonstrate the tandem-column separation even in the presence of broader overloaded peaks further validates the robustness of this new technique. Table 4.1 lists the retention time from each separation and peak width (full width at half maximum, FWHM) measured by the first detector for the twelve analytes separated by the Rtx-1/OFRR μGC system. A polarity index, defined here as the retention time differences from the two detection channels, which is correlated to the analyte volatility and polarity, divided by the retention time of the first detection channel, which is correlated to the analyte volatility, is also calculated for each analyte.

Co-elution

By providing more than one retention time, this tandem-column μGC system can overcome the co-elution problem, a key limitation in single-column separation and tandem-column separation. The co-elution can occur either immediately after the first column separation, caused by limited separation power usually seen in μGC system with a shorter GC column, as shown in Fig. 4.10, or from tandem-column ensembles, in which the adequately separated analytes from the first column co-elute after the second column

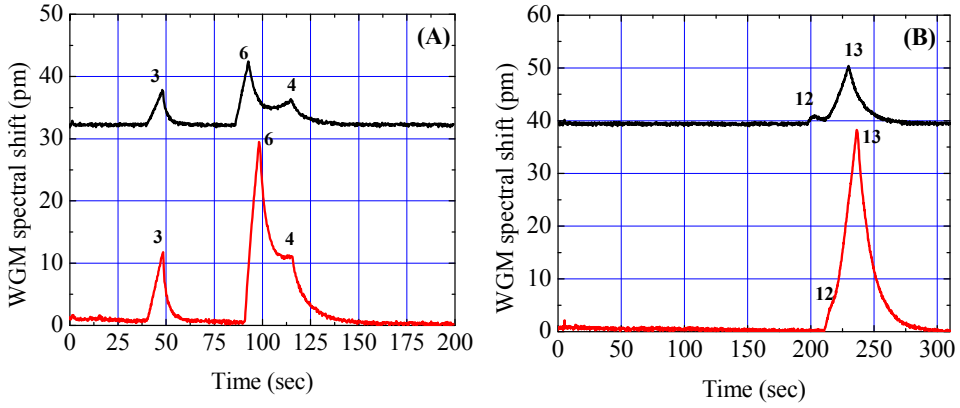

Fig. 4.12 Chromatograms from the two detection channels. The upper trace shows the separation from the 180 cm Rtx-5 GC column (50 °C). The lower trace shows the retention time from the Rtx-5/OFRR column ensembles. (A) Partial co-elution of Analyte #6 and #4 after the second separation due to added retention of Analyte #6 compared to Analyte #4 in the OFRR. (B) Co-elution of Analyte #12 and #13 after the second separation. Curves are vertically shifted for clarity. Reprinted from Ref. [38] with permission.

[151, 162]. For the first case, we have demonstrated that adding another column with different stationary phase will further separate the co-eluted analytes, which improves the separation capability. The latter scenario is demonstrated in Fig. 4.12 when Rtx-5 and the OFRR are used as the tandem separation columns. In Fig. 4.12(A), since the Rtx-5 column is slightly polar, octanol elutes right before the undecane peak. The OFRR column provides further retention for octanol, resulting in co-elution of the two analytes at the terminal end of the second separation. The same situation happens with DMNB and methyl salicylate, as shown in Fig. 4.12(B). Previously, modulation at the junction of tandem columns is needed to avoid co-elution at the end of the second column. For example, a pressure control valve has been employed to program and control the release of analytes at the end of first column so that separated analytes will not co-elute at the end of the column ensemble.[151, 162] However, owing to the unique multi-point on-column detection capability of the OFRR μGC system, we are able to avoid the necessity

of complicated modulation procedures. Since the two detectors are independent, they provide complementary information regarding the retention time for each analyte at different locations along the OFRR column. Therefore, as demonstrated in Fig. 4.12, the chromatogram from the first detector can be used to identify the two analytes instead of using the co-eluted chromatogram from the second detector. Additional detection locations can be readily added along the OFRR column, either before or after the current second detection location to track the separation of analytes along the OFRR column.

Monitoring the target analyte separation process

One of the powerful and versatile features of the OFRR-based tandem-column μGC is its capability of performing multi-point detection along the OFRR column. As discussed earlier, the detection channel can be moved along the OFRR column or additional detection channels can be added to form a sensor array to monitor the analytes separation process. Such capability is highly desirable in addressing co-elution problems and for enhanced selectivity. In Fig. 4.13 we demonstrate the monitoring of separation process of a target analyte (octanol) in a vapor mixture as it travels along the OFRR. This is accomplished by placing the second channel at two different locations along the OFRR column, illustrated by the insets of Fig. 4.13. Specifically, the first tapered fiber is kept at the OFRR inlet. The second tapered fiber is 3.5 cm downstream. The chromatogram from these two channels is recorded as Chromatogram #1. Then, the second taper is moved additional 4.5 cm downstream and Chromatogram #2 is taken. In Chromatogram #1 and #2, we can clearly see how octanol is separated by the Rtx-1 column and co-eluted with undecane in the middle part of the OFRR column, and then re-separated by the rest part

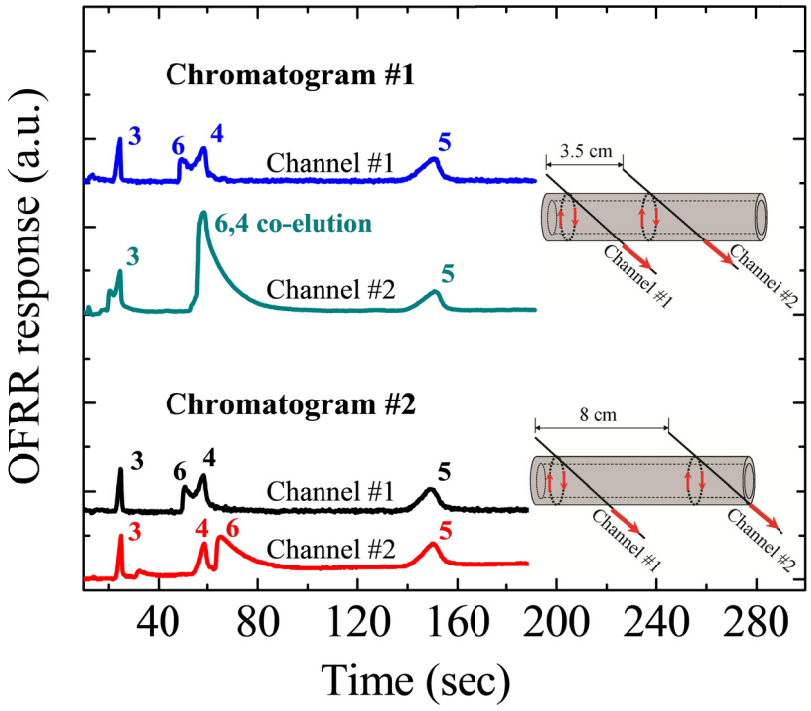

Fig. 4.13 Monitoring the separation process of the target analyte (Analyte #6: octanol) by acquiring three chromatograms at three different locations along the OFRR column. The top trace in Chromatogram #1 and #2 are recorded from the tapered fiber (Channel #1) located at the OFRR column inlet. The bottom trace in Chromatogram #1 and #2 are recorded from another tapered fiber (Channel #2) located 3.5 cm and 8 cm downstream from Channel #1, respectively. A 180 cm Rtx-1 column heated at 150 ^{o}C isothermal is used as the first separation column. The OFRR column is kept at room temperature. Curves are vertically shifted for clarity. Reprinted from Ref. [38] with permission.

of the OFRR column.

4.5 Conclusion

In this chapter, we combine ring resonator sensing technology and GC separation technology and develope OFRR-based μGC system. OFRR can either be used as a multi-dimensional on-column micro-detector to rapidly detect the separation from regular GC

columns, or be independently worked as an integrated separation column and on-column detector to separate and detector the vapor mixture simultaneously.

We have studied and demonstrated rapid detection of DNT at room temperature out of a volatile background using the OFRR μGC. The LOD of DNT is approximately 200-300 pg, which corresponds to an SPME extraction time of only one second at room temperature from equilibrium headspace. As compared to other optical vapor sensors, the OFRR vapor sensor has a similar sensitivity and detection limit, but a much more rapid sensor response time owing to the efficient gas fluidics, small sensor dimension, and on-column detection capability. Furthermore, the selectivity is greatly improved due to the incorporation of GC technology with the OFRR vapor sensor. Analyte of interest can be separated efficiently and detected rapidly from background analytes, which is especially useful for the detection of explosives buried in more volatile chemical compounds, thus significantly reducing the occurrence of false positives and negatives.

We further demonstrated rapid tandem-column separation and detection of vapor compounds using an OFRR-based μGC system, in which a nonpolar or slightly polar conventional GC column is used in conjunction with a short polar phase coated OFRR column so that the entire set of analytes can simultaneously be separated according to their respective vapor pressure and polarity in one single analysis. A vapor mixture of twelve analytes of different volatilities and polarities are separated and detected within four minutes using the tandem-column OFRR-μGC system.

Table 4.1 Properties of analytes used in experiments and OFRR μGC response parameters obtained from Fig. 4.11 and Fig. 4.12

No.	Compound (abbreviation)	Vapor pressure at 25 °C (Torr)	Retention index	Polarity	Retention time (sec)		FWHM peak width at Detector 1 (sec)	Polarity index (%) [a]
					Detector 1	Detector 2		
1	Heptane	45.56	700	Nonpolar	4.3	4.3	1.0	0
2	Octane	14.04	800	Nonpolar	8.4	8.4	1.6	0
3	Decane	1.43	1000	Nonpolar	39.8	39.8	5.6	0
4	Undecane	0.41	1100	Nonpolar	91.6	91.6	9.8	0
5	Dodecane	0.14	1200	Nonpolar	230.4	230.4	26.2	0
6	1-octanol	1.18	1050	Polar	59.5	65.7	3.2	10.4
7	Dimethyl methyl phosphonate (DMMP)	1.20	840	Polar	10.6	14.5	2.0	36.8
8	Diethyl methyl phosphonate (DEMP)	0.36	1000	Polar	34.7	44.7	4.1	28.8
9	2-nitrotoluene (2-NT)	0.18	1116	Polar	88.0	94.8	1.9	7.7
10	3-nitrotoluene (3-NT)	0.21	1141	Polar	113.7	122.9	5.4	8.1
11	4-nitrotoluene (4-NT)	0.12	1155	Polar	131.6	143.6	6.0	9.1
12	Dimethyl dinitro butane (DMNB)	0.00207	1122	Polar	91.2	107.3	1.4	17.7
13	Methyl salicylate [b]	0.03	1170	Polar	229.6	236.4	16.3	3.0

[a] Polarity index defined here as the retention time differences from the two detection channels divided by the retention time of the first detection channel.
[b] Data for Analyte #13 is obtained from Fig. 4.12.

Chapter 5

Bio-Inspired Optofluidic Lasers

In the previous chapters, we have studied chemical vapor sensing where the OFRR is used as a passive microcavity. However, when the gain medium is introduced into a passive cavity, the passive cavity can be turned into an active one under electrical or optical pumping. If the gain medium is pumped above its lasing threshold, stimulated emission supercedes spontaneous emission and leads to laser oscillation in the cavity and hence laser emission. Similar to a passive cavity sensor, an active cavity (or laser) can also be employed in bio/chemical sensing. Previous studies have suggested that a better LOD can be achieved by laser sensors than their passive cavity counterparts , due to the improved resonator parameter Q/V, the ratio of cavity quality factor Q and mode volume V [173-176]. However, in the laser sensing schemes developed to date, bio/chemical analytes are not part of the gain medium, that is, analytes are external to the laser cavity. This type of detection scheme is usually termed as *external cavity detection*. External cavity detection provides limited improvement in detection sensitivity and selectivity over its passive cavity counterpart, because bio/chemical analytes and gain medium are physically separated, Any small perturbations caused by the analyte lead only to a small response from the cavity sensor. In the following chapters, we will study a novel laser sensing mechanism, termed as *intra-cavity detection*, where bio/chemical analytes and gain medium become one entity. A small bio/chemical change in the analyte (hence the gain medium) is significantly amplified by the laser oscillation process in a cavity. In Chapter 5, we will develop a bio-inspired OFRR microlaser that is capable of

incorporating single-stranded DNA (ssDNA) as the gain medium. DNA-scaffold-controlled fluorescence resonance energy transfer (FRET) process is studied in the OFRR microlaser. Based on the laser system developed in Chapter 5, we will explore the optofluidic microlaser intra-cavity sensing. As a model system, the detection of DNA single-nucleotide polymorphism (SNP) with the OFRR laser sensor is demonstrated and exceptional detection selectivity is achieved as compared to the passive cavity sensing.

5.1 Optofluidic lasers

5.1.1 Existing optofluidic lasers

Optofluidic lasers have recently been under intensive investigation for lab-on-a-chip and compact on-chip light sources [11, 13, 14, 16, 19, 177-188]. They belong to an important emerging field of optofluidics [14, 16], in which photonics and microfluidics are integrated to achieve new functionalities. As compared to traditional liquid lasers (such as dye lasers), optofluidic lasers are much smaller in size, much safer to operate, and consume much less samples, owing to the easy liquid manipulation provided by microfluidics technology [19]. Additionally, optofluidic lasers inherit the desirable features of traditional dye lasers, *i.e.*, dynamic wavelength tunability and broad spectral coverage [14, 16, 19]. In the past few years, optofluidic lasers have been demonstrated using embedded distributed feedback (DFB) gratings [13, 19, 177, 178, 183, 185, 187, 188], circular Bragg gratings [189], and Fabry-Pérot-type resonators [179, 180, 182, 184, 186, 190]. However, all of those designs have relatively low Q-factors (on the order of 10^3), which leads to a high lasing threshold on the order of 10 $\mu J/mm^2$.

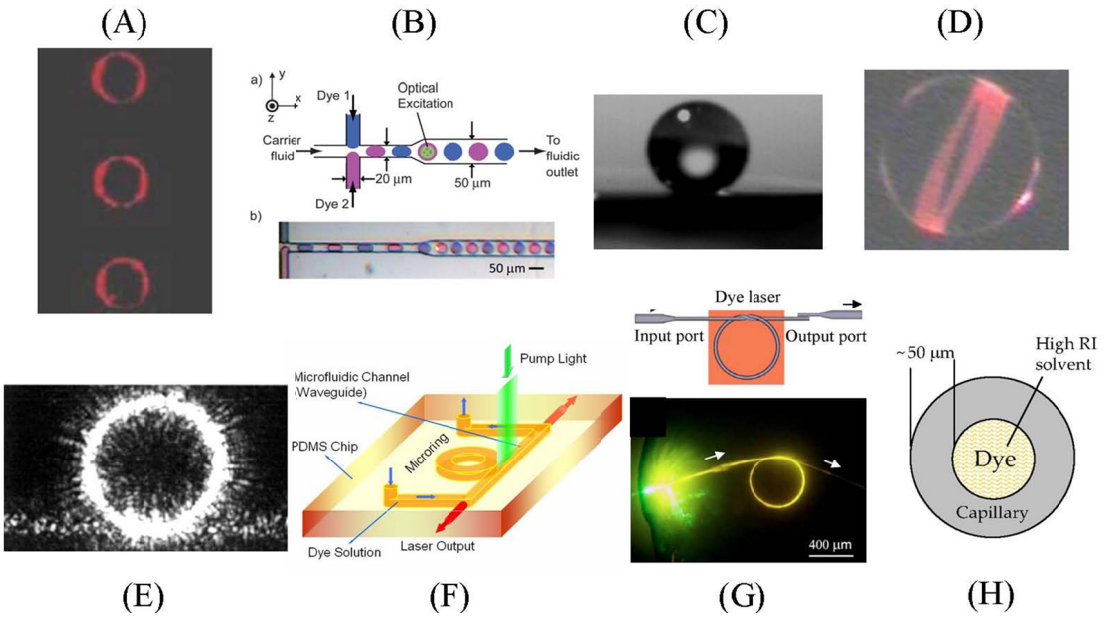

Fig. 5.1: Various ring resonator configurations for optofluidic lasers. (A) Free falling liquid droplets generated by an orifice; (B) Liquid droplets generated by microchannels; (C) Liquid droplet formed on an ultra-hydrophobic surface; (D) Fused silica microsphere immersed in gain medium; (E) Ring shaped waveguide formed on a chip; (F) Ring shaped liquid waveguide formed on a chip; (G) Ring resonator formed by a microfiber knot; (H) Liquid cylindrical resonator formed with a capillary. Reprinted from Ref. [11, 79, 183, 197, 202, 259] with permission.

Optical ring resonators have also been employed for optofluidic laser development. In a ring resonator, the WGMs form at the boundary of high and low RI media [94, 138]. The WGMs circulate along the ring resonator and interact with the surrounding gain medium and usually has much higher Q-factors than other types of optical cavities, thus providing an excellent optical feedback to achieve low lasing threshold [11, 41, 43, 44, 138, 191-201]. Fig. 5.1 shows various ring resonator configurations that have been or can be used for optofluidic lasers. Traditional microdroplets (Fig. 5.1(A) and (C)) have high Q-factors (~10^8) and have been extensively studied in the past decades [11, 41, 43, 44, 138, 191-201]. However, they suffer from evaporation and/or are difficult to manipulate and to integrate with other components into

a laser system. Recently, microdroplets generated with on-chip microfluidic system are developed, as shown in Fig. 5.1(B). However, due to the surrounded oil, lasing can only be achieved from high RI microdroplets. Moreover, in all droplets configurations, the laser emission is collected through scattering, making light delivery very challenging. Solid microspheres (Fig. 5.1(D)) are difficult to mass-produce. While solid or liquid ring-shaped waveguides (Fig. 5.1(E) and (F)) can be mass fabricated, they usually have much lower Q-factors (10^3-10^5). Microfiber knot based ring resonators (Fig. 5.1(G)) are too delicate to integrate with other components. Fig. 5.1(H) shows another ring resonator configuration, in which a regular glass capillary with a wall thickness over 30 micrometers is used [202-204]. However, this system requires the liquid RI in the core be higher than that of glass (RI=1.45). Unfortunately, bio-detection, i.e., DNA analysis, must be conducted in aqueous environment (RI=1.33) and the high RI requirement cannot be met.

5.1.2 OFRR microlasers

To address the problems in the existing optofluidic lasers mentioned above, we have recently developed OFRR microlaser technology that can operate with cavity in any liquid RI, and therefore be able to accommodate the low RI liquid such as water or buffer for biomolecular analysis. The reason that OFRR microlaser can uniquely operate with any liquid RI lies in the capillary wall thickness is sufficiently small. Detailed theoretical analysis on WGM intensity distribution in the radial direction is given in Chapter 2, proving that regardless of liquid RI (gain medium solvent) inside the OFRR, there is sufficient amount of light evanescently interacting with the gain medium for light

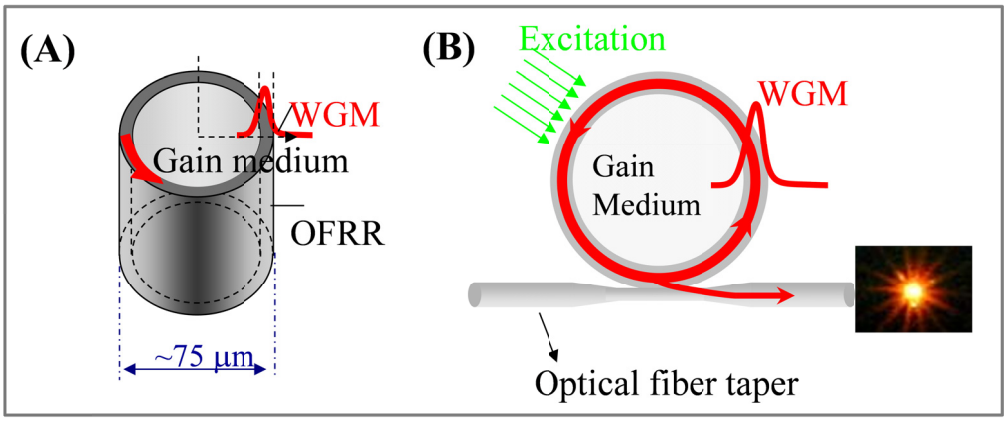

Fig. 5.2 Conceptual illustration of OFRR lasers: (A) side view and (B) top view. The capillary OD is 75 μm and wall thickness is less than 4 μm. Dye solution is filled into capillary as the gain medium. OFRR capillary cross section forms the high Q-factor ring resonator supporting WGMs that evanescently interacted with gain solution for light amplification. Laser emission can be collected in free space or with an optical fiber taper in contact with capillary wall for easy light delivery.

amplification. As illustrated in Fig. 5.2, the OFRR employs a piece of thin-walled fused silica capillary with an outer diameter of 30-200 μm. The circular cross section of the capillary forms the ring resonator that supports the WGMs of high Q-factors (>10^7). Therefore, a much lower lasing threshold can be achieved compared to other optofluidic lasers [92]. The capillary wall thickness is made less than 4 μm so that the WGMs are exposed to and interacting with the gain medium (*i.e.*, liquid dye solution) inside of the capillary (penetration depth ~ 100 nm), and provide the excellent optical feedback for low-threshold lasing. Additionally, the laser emission can easily and highly efficiently be coupled out via an optical fiber [86, 205], a fiber prism [48, 206] or a waveguide in contact with the OFRR. Through such evanescent coupling, only lasing emission will be collected [12, 92]. The unwanted emission such as fluorescence background or ambient noise cannot enter the WGM (a rejection ratio of about 10^5) and thus will not be transmitted through the optical fiber. As a result, the signal to noise ratio (SNR) is greatly

increased. Furthermore, the OFRR integrates naturally with the excellent fluidics inherent to capillaries, thus exhibiting superb fluid handling capability and allowing for approximately 1000 times reduction in sample effective detection volume (~ 1-10 nL). Finally, the OFRR can be fabricated easily and cost-effectively using a capillary pulling station or a fiber draw tower.

5.2 OFRR FRET microlaser through DNA self-assembly

5.2.1 Motivation

Since their invention 50 years ago, lasers have been realized with various artificial or engineered optical gain materials, such as doped crystals, synthetic dyes, gases, and semiconductors. However, biological materials were never pursued as gain medium or as part of the gain medium. Similarly, optofluidic lasers reported to date can only operate with synthetic dyes dissolved in organic solvent, *i.e.*, ethanol, quinolone, and tetraethylene glycol (TEG), as the gain medium. Such organic solvent environment is not bio-amenable, which makes it impossible to use optofluidic lasers in any biosensing applications. So far, no optofluidic lasers are demonstrated with water or biological buffers as gain medium solvent. Two major contributing factors for this challenge are (1) many ring resonator configurations are unable to operate in water/buffer due to the RI requirement, and (2) the quantum yield of organic dyes are almost two magnitudes lower in water/buffer than they are in organic solvents, which may significantly increase the lasing threshold or even fail to generate lasing.

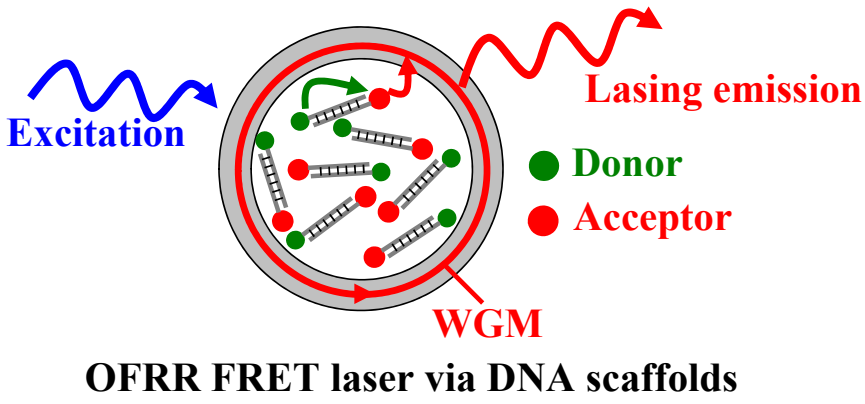

Fig. 5.3 Conceptual illustration of OFRR FRET lasers via DNA scaffolds. The donor transfers energy to the acceptor through FRET that is precisely controlled by DNA scaffolds. Note that the donor and the acceptor are labeled on complementary ssDNAs. Reprinted from Ref. [255] with permission.

In this chapter, we use OFRR as an optical cavity and show optofluidic lasers can be realized in a bio-amenable environment. This bio-compatible optofluidic laser is comprised of dye molecule labeled single-stranded DNA (ssDNA) dissolved in water/buffer as the gain medium. Since FRET is a widely used technique in biological and biomedical research, it is important to study this energy transfer process in the microcavity, which will provide valuable information when the optofluidic lasers are used in biosensing in the future. Therefore, we study lasing through FRET controlled by DNA scaffolds (see Fig. 5.3), in which the donor and acceptor are conjugated with DNA sequences with the pre-determined donor-to-acceptor distance, ratio, and spatial configuration [207-211]. Since the donor and the acceptor are maintained within the Förster distance by DNA scaffolds, high energy transfer efficiency can be obtained regardless of the donor/acceptor concentration. We will use various DNA scaffolds to exemplify vast possibilities in optofluidic laser designs and their biocompatibility.

5.2.2 Experimental methods

Fabrication of the OFRR capillary

The details of OFRR fabrication have been presented in previous chapters. In order to expose more evanescent field of the WGM to the gain medium, in optofluidic laser experiments, we first etch the fused silica capillary pre-form (Polymicro Technologies TSP700850) with diluted HF (3% v/v) for 17 hours at room temperature. The capillary pre-form wall thickness is reduced to 25-30 μm after etching. Then the capillary pre-form is fabricated by CO_2 lasers as detailed in Chapter 2. The resulting

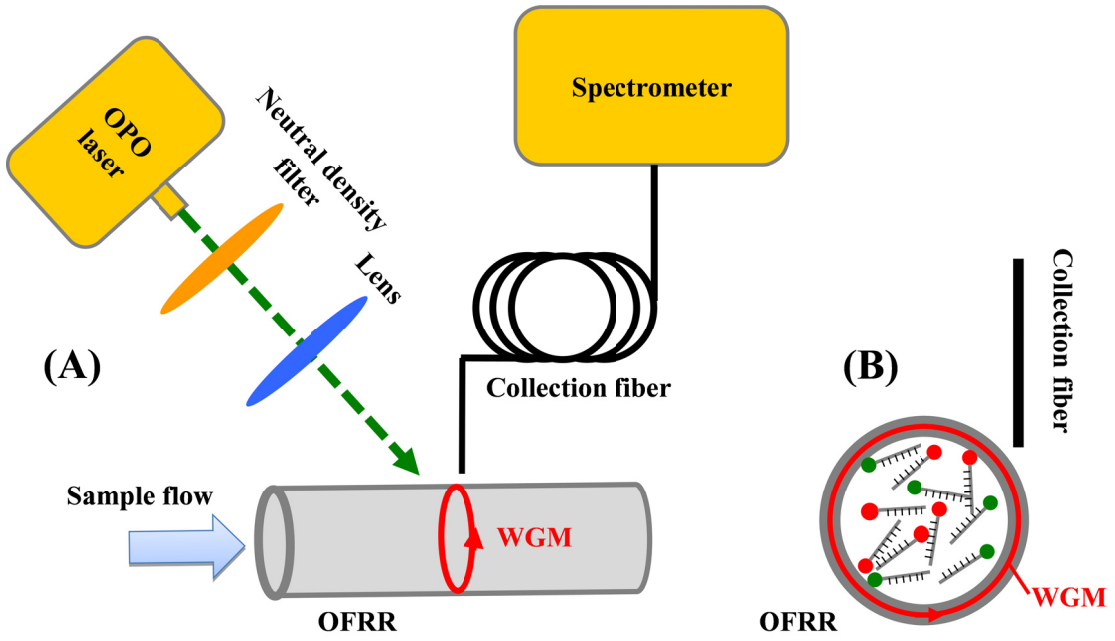

Fig. 5.4 (a) Schematic illustration of experimental setup. Pump light from an OPO laser is loosely focused to illuminate a small segment of the OFRR capillary. Organic dye labeled DNA samples are flowed through the capillary by a syringe pump. A multimode fiber is placed near the capillary edge to collect the lasing emission with the other end sent to a spectrometer for analysis. (b) Relative position of the collection fiber with respect to the OFRR. All dimensions are not to scale. Reprinted from Ref. [255] with permission.

OFRR capillary has a diameter of 75 μm with a wall thickness around 2–3 μm [12]. The Q-factor is approximately 10^7 [12].

Experimental setup

The experimental setup is illustrated in Fig. 5.4. A pulsed laser (Continuum Surelite OPO, approximately 5 ns pulse width, 20 Hz repetition rate) is loosely focused through a cylindrical lens to excite 1 mm portion of the OFRR capillary. The pump laser power is adjusted by a neutral density filter. The dye emission is collected in free space through a multimode fiber and then sent to a spectrometer (Triax 550i, Horiba Jobin Yvon, spectral resolution = 0.12 nm).

DNA preparation

ssDNA samples labeled with dyes are purchased from Integrated DNA Technology. Details on the DNA sequence are listed in Table 5.1. All the DNA sequences are designed using mfold software to minimize possible secondary structure formation [212]. The DNA samples are first dissolved in hybridization buffer (PerfectHyb™ Plus, Sigma-Aldrich) to a concentration of 90 μM and then diluted to the desired concentration with TRIS acetate-EDTA buffer (pH = 8.3) (Sigma-Aldrich). DNA hybridization is carried out by heating the samples to 45 ^{o}C for 3 minutes, followed by 20 minutes of cooling at room temperature. Finally, the hybridized sample is flowed through the OFRR with a peristaltic pump at a flow rate of 5 μL/min.

Table 5.1. Single-stranded DNA sequences used in the experiments

Sample name	Sequence
1D1A-Cy3	5'-TTC TCC TTG TCT A-Cy3-3'
1D1A-Cy5	5'-TAG ACA AGG AGA A-Cy5-3'
2D1A-Cy3(3')	5'-TTC TCC TTG TCT A-Cy3-3'
2D1A-Cy3(5')	5'-Cy3-TTC ACT CAG TCT-3'
2D1A-Cy5	5'-TAG ACA AGG AGA A-Cy5-AG ACT GAG TGA A-3'
Cascade-Cy3	5'-AAC CAG AGA CCC GA-Cy3-3'
Cascade-Cy5	5'-TCG GGT CTC TGG TT-Cy5-T GGC GTT GGG TTG-3'
Cascade-Cy5.5	5'-Cy5.5-CAA CCC AAC GCC A-3'
Control-Cy5	5'-TTT TTT TTT TTT T-Cy5-3'

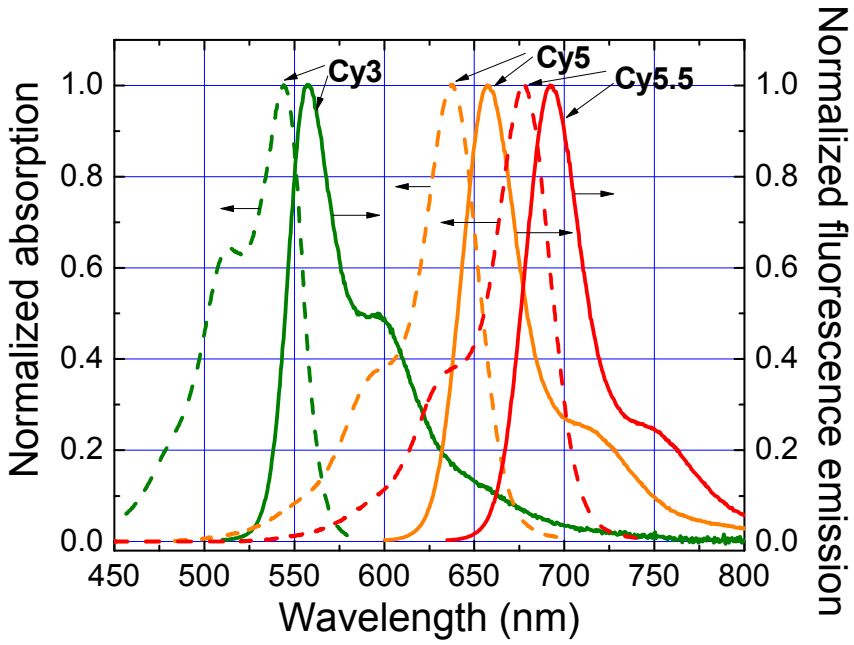

Fig. 5.5 Normalized absorption and emission spectra of the dyes used in the experiments. Reprinted from Ref. [255] with permission.

5.2.3 Experimental results

A simple OFRR FRET laser can be achieved through a one-donor-one-acceptor (1D1A) scaffold by using complementary ssDNAs, 1D1A-Cy3 and 1D1A-Cy5, with the donor (Cy3) and the acceptor (Cy5) conjugated to the 3' end of each ssDNAs (see sample name and corresponding DNA sequence in Table 5.1). During the experiment the excitation laser wavelength is 518.3 nm, which is within the donor absorption band (see Fig. 5.5). Fig. 5.6(A) shows the lasing emission spectrum after DNA hybridization at a concentration of 30 μM for both the donor and the acceptor. A number of quasi-periodic lasing peaks emerge around 720 nm first. With the increased pump intensity, this group of lasing emission gradually becomes leveled-off and meanwhile the lasing emission at shorter wavelengths (around 690 nm) starts to occur, as expected [213]. Both wavelength ranges are within the Cy5 emission band. No lasing emission is observed for Cy3 in the wavelength range of 570 – 650 nm, *i.e.*, the Cy3 emission band. As a negative control, we perform the same experiment with 30 μM of 1D1A-Cy5 alone (Fig. 5.7(A)). No lasing emission from Cy5 is observed when pumped at 518.3 nm, suggesting that Cy5 cannot be directly excited to achieve lasing at this pump wavelength and that the lasing emission from Cy5 in Fig. 5.6(A) indeed result from the energy transferred from Cy3. Fig. 5.6(B) plots the total laser emission around 690 nm and around 720 nm as a function of the pump energy density. The respective lasing threshold is 6.8 $\mu J/mm^2$ and 4.2 $\mu J/mm^2$.

An additional control experiment presented in Fig. 5.7(B) allows us to understand the energy transfer mechanism. In this experiment, Cy3 lasing occurs when 30 μM of 1D1A-Cy3 sample alone is pumped under exactly the same conditions as in Fig. 5.6(A). However, when 1D1A-Cy5 is added the Cy3 lasing is quenched with concomitant

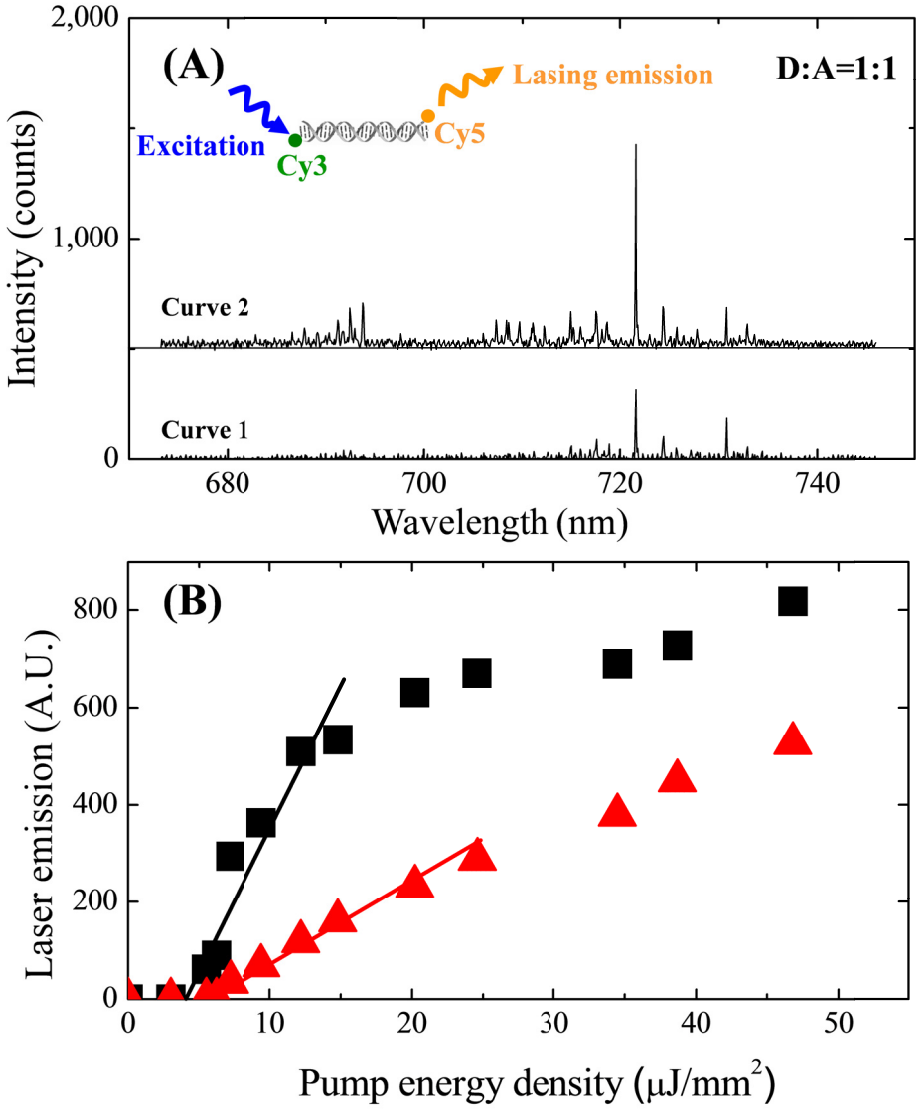

Fig. 5.6 (A) OFRR FRET lasing emission spectra for the donor-to-acceptor ratio of 1:1 achieved through hybridization of 1D1A-Cy3 and 1D1A-Cy5. The concentration of both ssDNA samples is 30 μM. Laser excitation wavelength is 518.3 nm. Curve 1 and 2 are the spectrum slightly and well above the lasing threshold, respectively. Curves are vertically shifted for clarity. Inset: the corresponding DNA scaffolds. (B) Laser emission as a function of pump energy density per pulse. Triangles: laser emission integrated between 680 nm and 700 nm. Squares: laser emission integrated between 700 nm and 740 nm. Solid curves are the linear fit of the linear part of the integrated laser emission. Lasing threshold is 6.8 μJ/mm^2 and 4.2 μJ/mm^2 for the laser emission centered at 690 nm and 720 nm, respectively. Reprinted from Ref. [255] with permission.

appearance of Cy5 lasing emission (see Fig. 5.6(A)), suggesting that the non-radiative FRET plays a dominant role in energy transfer [214, 215]. Through a DNA scaffold, the distance between Cy3 and Cy5 and hence the FRET efficiency can be determined by the hybridized DNA length. Given the Förster distance for Cy3 and Cy5 of 6 nm (see Table 5.2) and the Cy3-Cy5 distance of 4.08 nm (assuming 0.34 nm per DNA base pair), the FRET efficiency from Cy3 to Cy5 is calculated to be 91%.

Table 5.2. Förster distance of the donor-acceptor pairs used in the experiments

Donor-acceptor pair	Förster distance [208]
Cy3-Cy5	6 nm
Cy3-Cy5.5	5.9 nm
Cy5-Cy5.5	7.3 nm

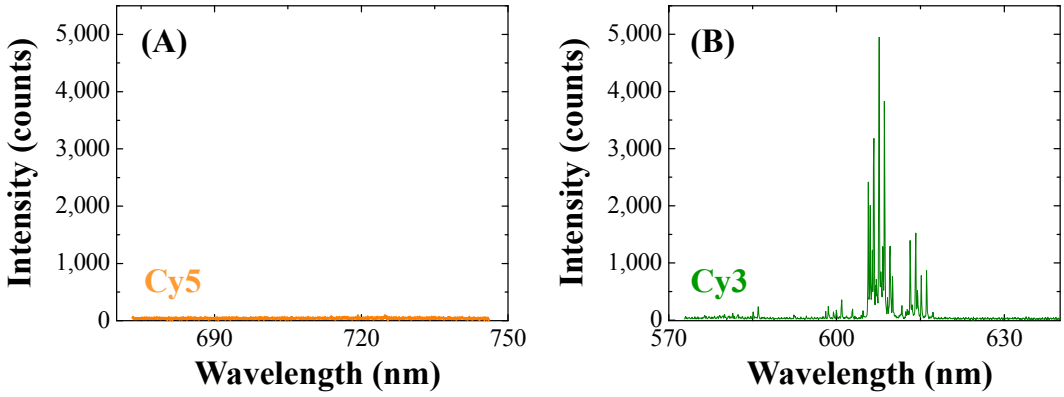

Fig. 5.7 Control experiments on Cy3-Cy5 FRET lasing. (a) When pumped at 518.3 nm, 30 μM Cy5 labeled ssDNA (1D1A-Cy5) alone shows no lasing emission, suggesting that Cy5 cannot be directly excited to achieve lasing at this pump wavelength. (b) When pumped at 518.3 nm, 30 μM Cy3 labeled ssDNA (1D1A-Cy3) alone has strong lasing emission around 610 nm, which is within the Cy3 emission band. Reprinted from Ref. [255] with permission.

The OFRR laser can be controlled not only by the donor-acceptor distance, but also by the DNA scaffold that changes the donor-to-acceptor ratio. With the increased donor-to-acceptor ratio, more pump energy can be absorbed by the laser system, resulting in a lower lasing threshold and a higher pump efficiency [216]. As illustrated in the inset of Fig. 5.8(A) we construct a DNA scaffold consisting of two-donor-one-acceptor (2D1A) by self-assembly of three ssDNAs. In this 2D1A system the donor (Cy3) is attached to the 3' and 5' end of a ssDNA sequence, respectively (2D1A-Cy3(3') and 2D1A-Cy3(5'), see Table 5.1). The acceptor (Cy5) is labeled on the adenine base in the middle of the ssDNA sequence (2D1A-Cy5), which serves as a DNA backbone for hybridization with 2D1A-Cy3(3') and 2D1A-Cy3(5').

After hybridization, the distance between each Cy3 and Cy5 pair is 4.08 nm, the same as that in the 1D1A case discussed previously. Thus the donor-to-acceptor ratio is doubled while the donor-acceptor distance remains unchanged. The corresponding lasing emission spectrum is present in Fig. 5.8(A), which has quasi-periodic lasing peaks similar to Fig. 5.6(A). At the same pump intensity, the FRET lasing intensity in the 2D1A system is stronger than that in the 1D1A system and more lasing peaks emerge. The corresponding lasing threshold curve in Fig. 5.8(B) shows a lasing threshold of approximately 4.4 $\mu J/mm^2$ and 2.3 $\mu J/mm^2$ for the laser emission centered at 690 nm and 720 nm, respectively, which are approximately half of their corresponding threshold for the 1D1A system. Additionally, the lasing differential efficiency, *i.e.*, the slope of the curve in Fig. 5.8, is nearly doubled in the 2D1A system in comparison with the 1D1A system for both 690 nm and 720 nm bands.

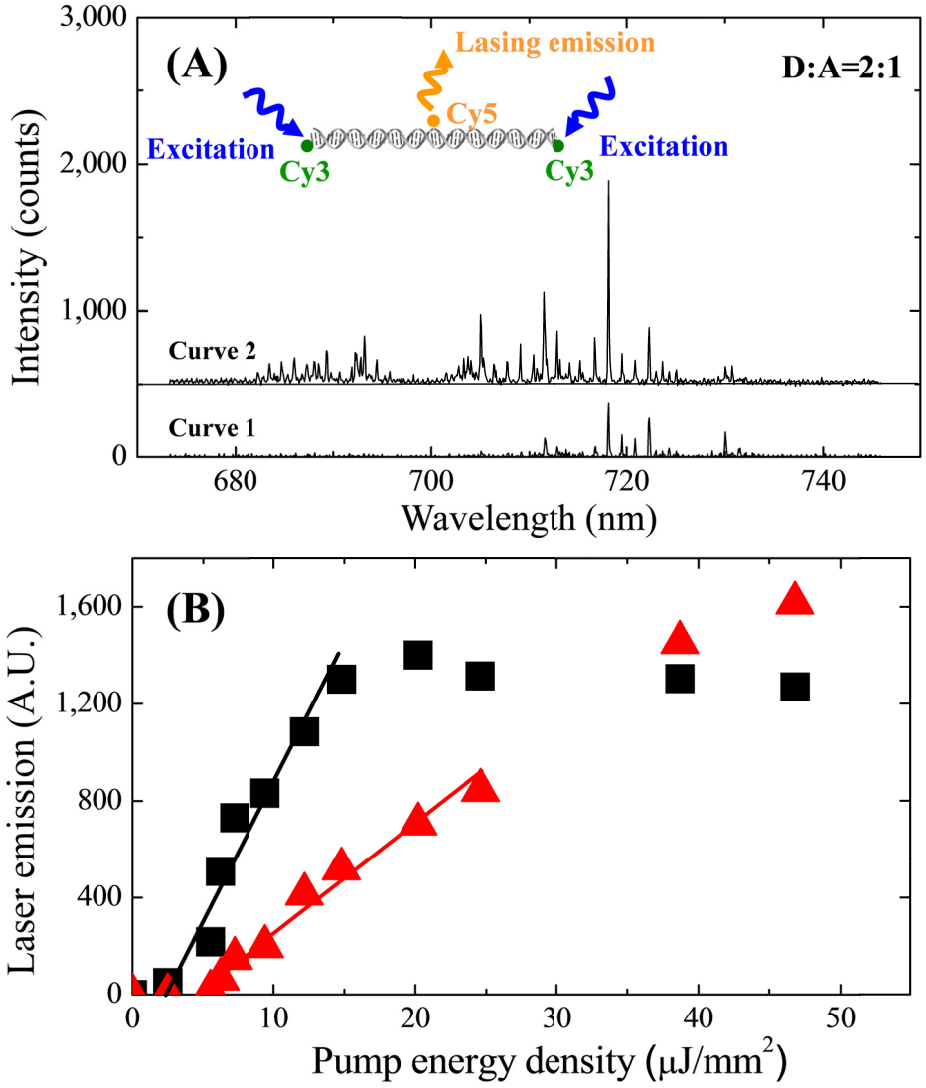

Fig. 5.8 (A) OFRR FRET lasing emission spectrum for the donor-to-acceptor ratio of 2:1 achieved through hybridization of 2D1A-Cy3(3'), 2D1A-Cy3(5'), and 2D1A-Cy5. The concentration of all ssDNA samples is 30 μM. Laser excitation wavelength is 518.3 nm. Curve 1 and 2 are the spectrum slightly and well above the lasing threshold, respectively. Curves are vertically shifted for clarity. Inset: the corresponding DNA scaffolds. (B) Laser emission as a function of pump energy density per pulse. Triangles: laser emission integrated between 680 nm and 700 nm. Squares: laser emission integrated between 700 nm and 740 nm. Solid curves are the linear fit of the linear part of the integrated laser emission. Lasing threshold is 4.4 μJ/mm^2 and 2.3 μJ/mm^2 for the laser emission centered at 690 nm and 720 nm, respectively. Reprinted from Ref. [255] with permission.

As discussed earlier, through a DNA scaffold the high energy transfer efficiency can be maintained regardless of the donor or acceptor concentration. In Fig. 5.9, we explore the minimum gain medium concentration that can achieve lasing via FRET using 2D1A samples of 30 μM, 15 μM, 5 μM, and 2.5 μM, respectively. It is shown that the laser emission persists even at an unprecedented concentration of 2.5 μM with a lasing threshold well below 50 μJ/mm^2, nearly 1000 times lower than the dye concentration used in other types of optofluidic lasers. Considering that the WGM interacts with only a

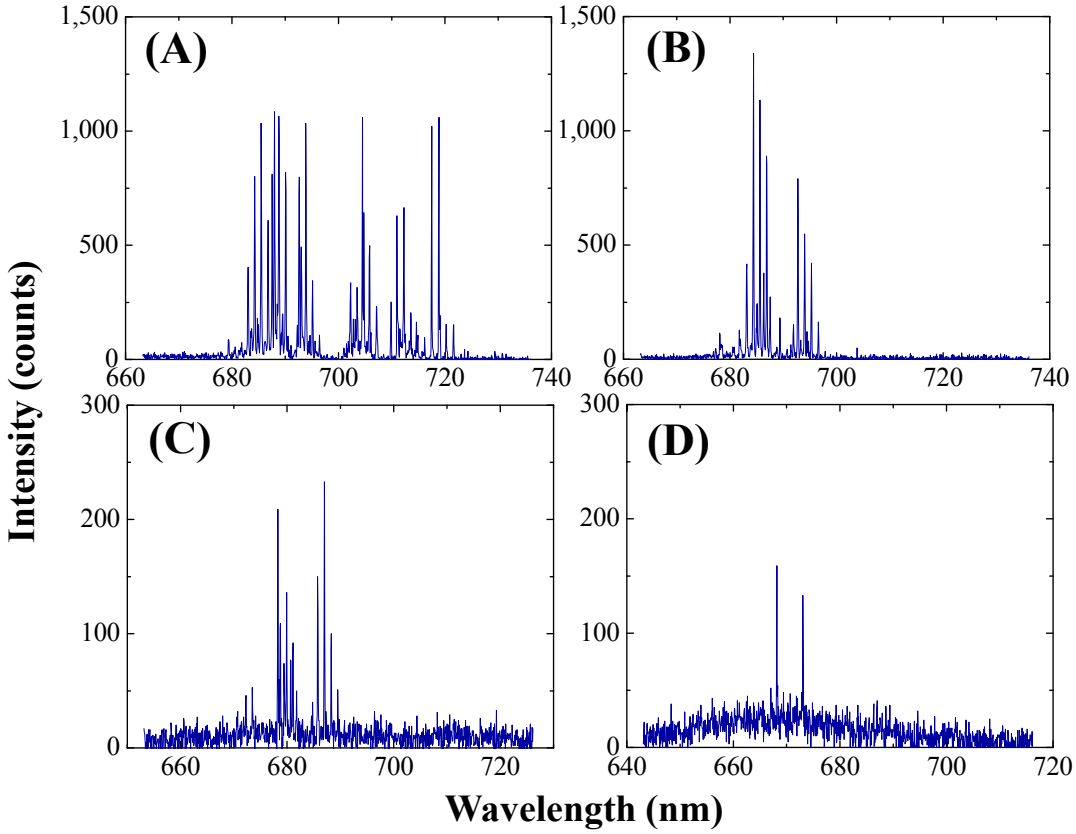

Fig. 5.9 Emission spectrum of 2-donor-1-acceptor FRET lasers at various ssDNA concentrations. (A) 30 μM. (B) 15 μM (C) 5 μM, and (D) 2.5 μM. The pump energy density per pulse is fixed at 54 μJ/mm^2. Reprinted from Ref. [255] with permission.

few pico-liters of dye solution near the OFRR inner surface, the total number of dye molecules contributing to the laser emission is estimated to be on the order of 10^7.

The same DNA scaffold design principles can further be applied to develop cascade FRET lasers to extend the lasing emission wavelength range. Similar to the 2D1A structure, we now hybridize three ssDNA sequences, Cascade-Cy3, Cascade-Cy5, and Cascade-Cy5.5 (see Table 5.1). After hybridization, the distance from Cy3 to Cy5 and from Cy5 to Cy5.5 is 4.42 nm, corresponding to a transfer efficiency of 86% (Cy3-Cy5), 95% (Cy5-Cy5.5), and 8% (Cy3-Cy5.5), respectively. Therefore, the majority of energy is transferred from Cy3 to Cy5.5 via Cy5. Cascade FRET lasing emission from Cy5.5 is shown in Fig. 5.10(A) at the pump wavelength of 518.3 nm. No lasing emission is observed from Cy3 or Cy5. Control experiments (see Fig. 5.11) confirm that Cy5 and Cy5.5 cannot be directly excited to achieve lasing at this pump wavelength. Lasing

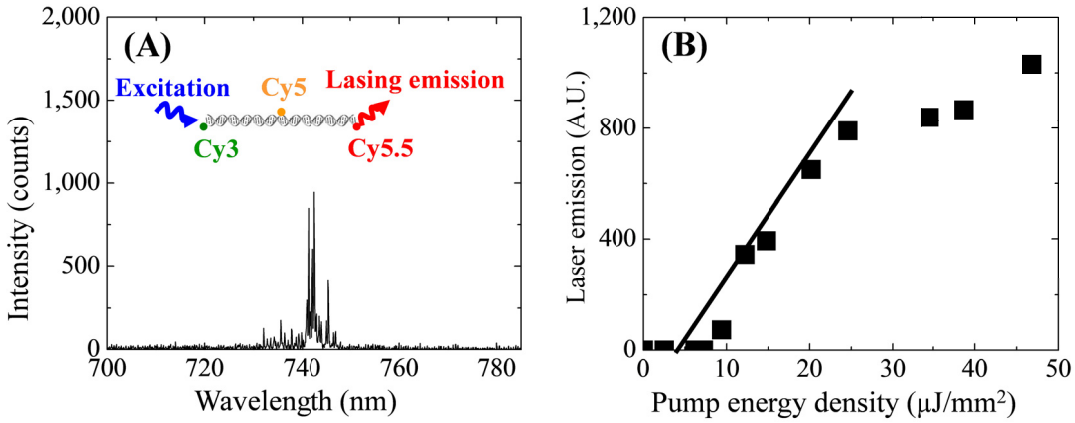

Fig. 5.10 Cascade OFRR FRET laser. (A) Lasing emission spectrum. Laser excitation wavelength is 518.3 nm. The concentration of all ssDNAs is 30 μM. Inset: the DNA scaffold structure that bridges Cy3, Cy5, and Cy5.5. (B) Lasing emission integrated between 720 nm and 760 nm versus pump energy density per pulse. Solid curve is the linear fit of the linear part of the integrated laser emission. Lasing threshold is 6 μJ/mm^2. Reprinted from Ref. [255] with permission.

threshold in Fig. 5.10(B) is measured to be approximately 6 μJ/mm^2.

5.2.4 Energy transfer in an optical cavity

Generally, there are two transfer mechanisms between the donor and the acceptor in an optical cavity: non-radiative FRET [214, 216-218], in which the transfer is mediated by short-ranged resonant dipole-dipole interaction (as shown in Fig. 5.3), and cavity-assisted radiative transfer [219-221], in which the emission from the donor is first coupled into the cavity, which stores photons for extended amount of time before they are re-absorbed by the acceptor (as shown in Fig. 5.12). The FRET efficiency between a donor and acceptor pair is $R_0^6/(R_0^6+r^6)$, where R_0 and r are the Förster distance and the donor-acceptor distance, respectively. The cavity-assisted transfer efficiency is determined by the fraction of donor emission into cavity modes and the probability of acceptor re-absorption [219, 220]. Unfortunately, to date only a handful of energy transfer based optofluidic lasers have been demonstrated [214, 218]. In those lasers, the

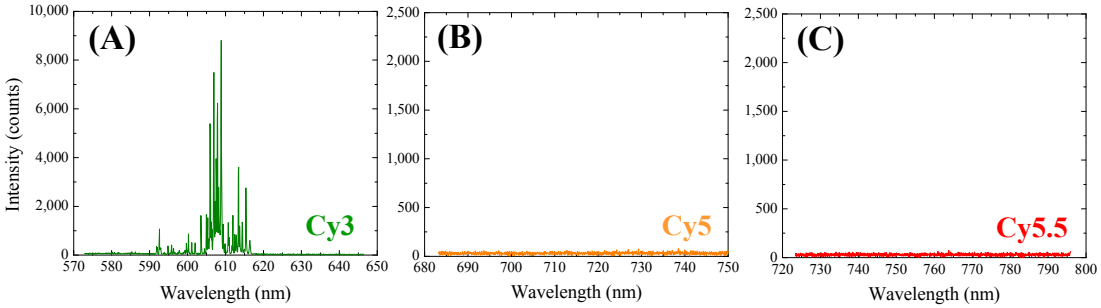

Fig. 5.11 Control experiments on cascade FRET lasing. When pumped at 518.3 nm, Cy3 alone has lasing emission around 610 nm, while Cy5 alone or Cy5.5 along shows no lasing at their respective emission wavelength range, suggesting that neither Cy5 nor Cy5.5 can be directly excited to achieve lasing at this pump wavelength. Reprinted from Ref. [255] with permission.

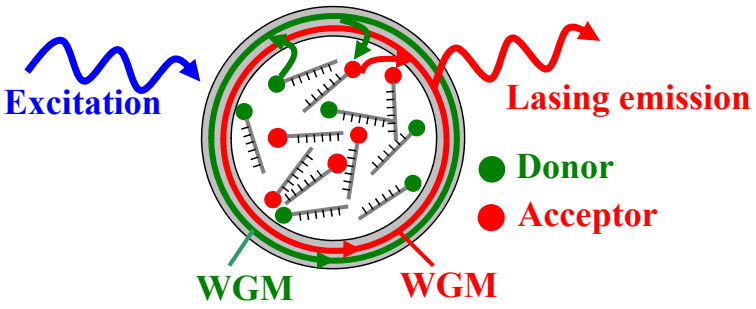

Fig. 5.12 Conceptual illustration of OFRR-assisted energy transfer lasers, in which donor emission coupled into cavity modes is used to excite the acceptor. Note that the donor and the acceptor are labeled on non-complementary ssDNAs. Reprinted from Ref. [255] with permission.

donor and the acceptor are distributed homogeneously in solution. Therefore, the transfer efficiency can only be estimated from the donor/acceptor concentration (*i.e.*, the averaged donor-acceptor distance), which diminishes rapidly at decreased donor/acceptor concentrations. Additionally, although vastly different, the respective contribution of FRET and the cavity-assisted transfer in optofluidic lasers has not been well elucidated [214], due in part to the lack of an approach to precisely control the donor-acceptor distance in the gain medium. How to better understand and control the energy transfer processes, and how to maintain high transfer efficiency at low donor/acceptor concentrations are particularly important for the development of novel optofluidic lasers, and for their applications in bio/chemical sensing and biophysics. Here, with DNA scaffold, we are able to, for the first time, study the two energy transfer mechanisms in the cavity separately. As shown in previous experiments, with complementary ssDNA scaffold, donor and acceptor are kept within Förster distance, and thus efficient FRET is the dominant transfer mechanism. On the contrary, if donor and acceptor are labeled on non-complementary ssDNA scaffold, this equivalent to donor and acceptor are in free

solution. At low concentration, the distance between donor and acceptor on average will fall out of the Förster distance so that cavity assisted energy transfer will dominate. Below, we will use the non-complementary ssDNA scaffold to study the cavity-assisted energy transfer lasing, which will also act as the control experiment for FRET lasing shown previously. Additionally, we will perform a theoretical analysis on different energy transfer processes at last.

Control experiments on OFRR-assisted energy transfer lasing

It should be noted that in the absence of highly efficient FRET, cavity-assisted energy transfer can be employed to excite the dye laser. To investigate the contribution from the cavity-assisted transfer, we further carry out a control experiment by using the non-complementary ssDNAs. In this case, the average distance between donor and acceptor is approximately 24 nm, making FRET negligible. Fig. 5.13 shows the typical WGM-assisted acceptor lasing spectrum and the relationship between pump energy density and lasing intensity, respectively. The lasing threshold is approximately 10 $\mu J/mm^2$, much higher than the FRET lasing threshold at the same concentration. This difference becomes even larger at lower DNA (or dye) concentrations, as shown in Fig. 5.13 where the cavity-assisted energy transfer efficiency drops rapidly with the decreased gain medium concentration. As a result, no laser emission can be observed through cavity-assisted energy transfer (or direct excitation) when the dye concentration is below 10 μM, regardless of the pump energy density available with our OPO laser (> 200 $\mu J/mm^2$), in sharp contrast to Fig. 5.8. Note that the lasing in Fig. 5.13 is obtained in the absence of FRET. In the presence of competitive and highly efficient FRET through a

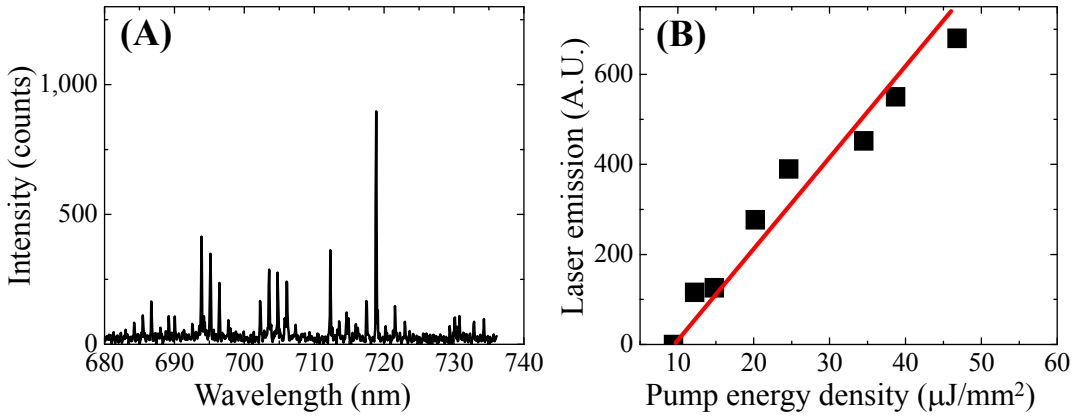

Fig. 5.13 (A) Cavity-assisted lasing emission spectrum in the OFRR using non-complementary ssDNA samples: 1D1A-Cy3 and Control-Cy5 (both at 30 μM, see Table 5.1). (B) Laser emission integrated between 700 nm and 740 nm versus pump energy density per pulse. The excitation wavelength is 518.3 nm. Reprinted from Ref. [255] with permission.

DNA scaffold, the cavity-assisted energy transfer based lasing would not occur, as reflected by the disappearance of the donor (Cy3) lasing emission when complementary DNA labeled with the acceptor (Cy5) is added.

Theoretical analysis

A. Donor and acceptor pair linked by complementary ssDNA

When the donor and acceptor are linked through a DNA scaffold, the high FRET efficiency can be maintained regardless of the donor or acceptor concentration. The FRET efficiency between the donor and acceptor pair is:

$$E_{FRET} = \frac{R_0^{\,6}}{R_0^{\,6} + r^6}, \tag{5.1}$$

where R_0 is the Förster distance and r is the distance between the donor and acceptor. Curve a in Fig. 5.14 plots the FRET efficiency between Cy3 and Cy5 using R_0 = 6 nm and r = 4.08 nm (a 13-base DNA pair).

B. Donor and acceptor distributed homogenously in solution

The FRET efficiency can be calculated by [217]:

$$E_F = 1 - \exp(-1.42 \cdot C / C_0), \tag{5.2}$$

where C is the acceptor concentration in units of molar. C_0 is related to the Förster distance R_0 by:

$$C_0 = (\frac{3}{4000 \cdot \pi \cdot N_A R_0^{\ 3}}), \tag{5.3}$$

where N_A is Avogadro constant. Curve b in Fig. 5.13 shows the FRET efficiency as a function of the acceptor concentration.

C. OFRR-assisted energy transfer

Cavity-assisted energy transfer takes advantage of the fact that a donor's emission rate is in proportion to the local density of photon states (weak coupling), and the states in a cavity are heavily modified from those in an extended medium [219, 220, 222, 223]. In particular, WGMs have huge spectral densities due to their narrow line-widths, which allows emission to be channeled into these long-lived cavity states where acceptors are visited many times [220, 222, 223]. The overall OFRR-assisted transfer efficiency can be calculated by [219, 220]:

$$E_{OFRR} = E_{donor} \times [\frac{\eta Q_0}{\eta Q_0 + Q_a}], \tag{5.4}$$

where the first term, E_{donor}, is the fraction of donor emission into absorption dominated WGMs compared to all modes within the mode volume. The second term represents the

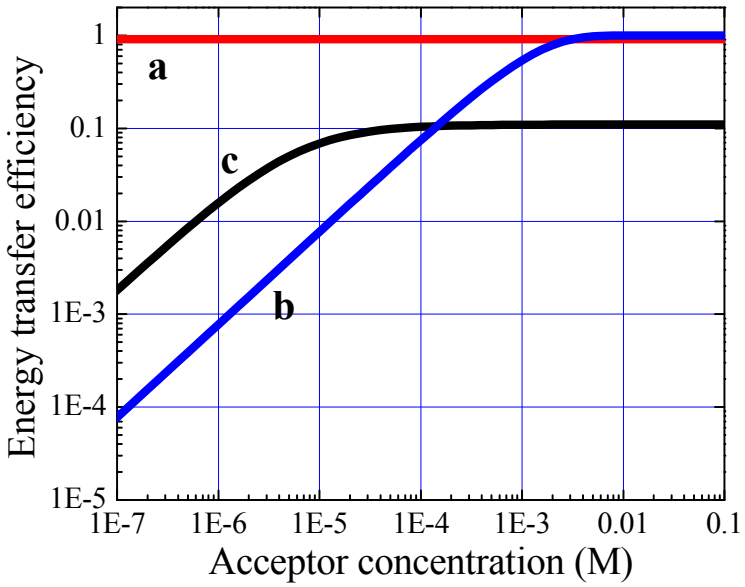

Fig. 5.13 (a) FRET efficiency between Cy3 and Cy5 through a 13-base-pair DNA scaffold. Calculation is based on equation (5.1). (b) Energy transfer efficiency for FRET between Cy3 and Cy5 in free solution. Calculation is based on equations (5.2) and (5.3). (c) OFRR-assisted energy transfer efficiency between Cy3 and Cy5. Calculation is based on equations (5.4) and (5.5), where E_{donor} = 11%, α = 5.75×10^5 cm^{-1} M^{-1}, λ = 630 nm, n = 1.45, and $\eta Q_0 = 4 \times 10^4$. Reprinted from Ref. [255] with permission.

transfer efficiency of the light in the WGMs to the acceptor. $Q_0 = \omega/\gamma$, is the OFRR Q-factor in the absence of the acceptor. ω is the angular frequency of the light and γ is the photon loss rate of the resonant mode. $Q_a = 2\pi n/\alpha\lambda$, is the absorption related Q-factor. n is the refractive index of the OFRR, α is the acceptor absorption coefficient, and λ is the wavelength. Since the WGMs in the OFRR interact with the acceptor via their respective evanescent field, η represents the fraction of the WGM energy in the OFRR core [12].

E_{donor} can be obtained by comparing the number of energy transfer dominated states within a cavity with the number of states in a bulk medium of the same volume V and refractive n, which leads to [223]:

$$E_{donor} = \frac{DS_{ad} f c^3}{8\pi n^3 < \nu^2 > V}, \tag{5.5}$$

where D is WGM degeneracy. S_{ad}, f, and c are the average spectral density of absorption dominated modes, the ratio of the widths of the overlap spectrum to the emission spectrum, respectively. $<\nu^2>$ is the average of the frequency squared over the donor-acceptor overlap region.

For the OFRR, although it may be difficult to obtain exact S_{ad}, f, and V, simple estimation will still provide very useful insight into this system. The OFRR develops a larger spectral density of two fold degenerate WGMs (D = 2). Our measurements in Fig. 5.14 show 11 modes in 38 pm with Q's greater than $5x10^5$ (absorption dominated modes), which leads to $S_{ad} = 5.4x10^{-10}$ Hz^{-1}. From the spectra in Fig. 5.5, the spectral overlap factor $f \approx 1$. The mode volume V as scaled from Ref. [224] is found to be $V \approx 2.3x10^{-8}$

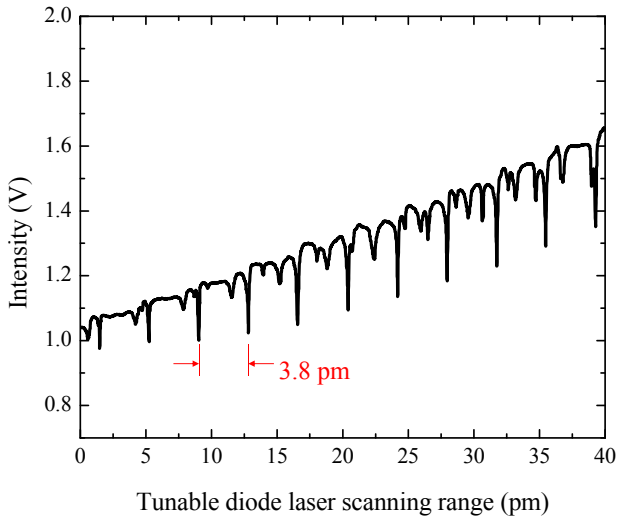

Fig. 5.15 WGMs obtained with a high resolution Toptica tunable diode laser at 785 nm. The mode spacing is approximately 3.8 pm. Reprinted from Ref. [255] with permission.

cm^3. By evaluating $<\nu^2>$ from the frequency at the center of the overlap region, $2.1x10^{29}$ Hz^2, and using the refractive index n as that of water, 1.33, we find E_{donor} = 11%.

Curve c in Fig. 5.13 shows the OFRR-assisted energy transfer efficiency as a function of the acceptor concentration based on Eq. (5.5). E_{donor} = 11%, $\alpha = 5.75x10^5$ cm^{-1} M^{-1} for Cy5, λ = 630 nm, n = 1.45, and $\eta Q_0 = 4x10^4$ for the lasing modes [12].

5.3 Conclusion

We have demonstrated the first bio-compatible optofluidic dye lasers based on OFRR. The FRET lasing via various DNA scaffolds are presented. High transfer efficiency can be maintained in an extremely large concentration range (from a single donor/acceptor pair up to approximately 1 mM). FRET lasing at 2.5 μM has been achieved. With further improvement in the excitation scheme (*e.g.*, tapered fiber excitation at a WGM resonant wavelength), Q-factors, and DNA scaffold designs, and using donors with larger absorption cross sections (such as quantum dots [218] and DNA binding fluorescent conjugated polymers [225]), lasing at nM range is possible.

We envision that our work will lead to the research in the following areas. First, through DNA self-assembly technologies [226-228] and other biotechnologies such as enzymatic cleavage [229], metal chelation [229], peptide design, and DNA binding fluorescent conjugated polymers [225], various types of biostructures (such as Holliday junctions [226], 2D or 3D supermolecular structures [226-228], DNA packing motors [230]) can be employed to provide great flexibility in designing optofluidic lasers as well as other bioinspired optofluidic devices such as bio-controlled photonic switches. Second,

instead of using the optical excitation external to the laser system and non-biological donors (such as dyes), it certainly is possible to develop bio-optofluidic lasers that rely on biomolecules such as green fluorescent protein and luciferase to harvest bio- or chemical energy through highly efficient bioluminescence resonance energy transfer (BRET) processes [231]. Third, FRET is a widely used technology in biology and chemistry [229, 232]. Combination of FRET with highly non-linear optofluidic lasers can be exploited for highly sensitive intra-cavity biological and chemical detection [176, 233], which may not be achievable in the linear fluorescence based detection. Finally, our system may provide a model system for fundamental physics such as lasers at the level of single or a few molecules.

Chapter 6

Intra-Cavity Optofluidic Laser Sensor

6.1 Motivation

Based on the bio-compatible optofluidic laser system developed in Chapter 5, we will explore its biosensing capabilities. As an immediate application, we will study highly-selective intra-cavity DNA detection in this chapter.

A DNA sequence may have a single-base change resulting from biological processes such as single-point mutation and cytosine methylation [234, 235]. Distinguishing the target DNA from its single-base altered counterpart provides critical information for disease diagnosis, personalized medicine, and basic biochemical research [236-240]. In traditional fluorescence-base detection, samples are placed in a cuvette external to an excitation source (such as a laser), and a DNA probe is used to hybridize with the target DNA and generate the corresponding fluorescence as the sensing signal. However, due to the small difference in the binding affinity for the DNA probe, the resulting fluorescence difference between the target and single-base altered DNA is very small. Typically, the discrimination ratio between these two DNA sequences is almost unity (~1-3) [241-245], making it difficult to selectively detect the target DNA from a pool of altered DNA molecules directly [246, 247].

In contrast, the intra-cavity detection involves placing samples inside a laser cavity, thus generating a feedback that may significantly affect the laser characteristics.

Historically, passive intra-cavity detection, in which the sample is part of a laser cavity, but not of the gain medium, has long been employed in sensitive vapor absorption detection due to the extended effective absorption length [248]. Active intra-cavity detection, in which the sample becomes part of the laser gain medium, relies on the nonlinear behavior of the laser output in response to perturbations to the laser cavity and/or gain medium caused by the sample. While the active intra-cavity detection was recently used in a solid-state laser for enhanced vapor sensing [176], its capability in biomolecular detection remains largely unexplored.

The optofluidic laser – the synergistic integration of a dye laser and microfluidics – is an emerging technology that takes advantage of compact light source, easy sample delivery, and extremely small sample volumes for the development of micro-total analysis systems [19, 21, 249]. Here, by capitalizing on the recent advance in optofluidic lasers, we propose and develop a paradigm-changing, highly specific intra-cavity DNA detection scheme, in which DNA samples and probes are flowed through the optofluidic laser and thus become an integral part of the laser. Stimulated lasing emission, rather than fluorescence (*i.e.*, spontaneous emission), is employed as the sensing signal to achieve analog-to-digital type conversion that significantly amplifies the small intrinsic difference between the target and its single-base altered counterpart. In this chapter, we use SNP and molecular beacon (MB) probe as a model system. We first perform the theoretical analysis to elucidate the underlying intra-cavity detection principle. Then, we show experimentally that a discrimination ratio of 240 was achieved between the target and the single-base mismatched DNA, which represents over two orders of magnitude increase over the conventional fluorescence-based method. Selective detection of the target DNA

from a pool of single-base mismatched DNA of 50 times higher concentration and quantitative measurement of the target DNA are presented. Finally, we extend our scheme to detect a more complicated DNA sequence, breast cancer related gene - BRCA1, in both buffer and serum.

6.2 Conventional fluorescence-based DNA SNP detection using MB

An MB is a stem-loop structured DNA probe with a fluorophore and a quencher attached to each end of the sequence (see the inset of Fig. 6.3) [247, 250-253]. In the absence of the target DNA (*i.e.*, perfectly matched DNA), the fluorophore and the quencher are in close proximity, and the fluorescence is quenched. In the presence of the target DNA, the MB opens, which results in fluorescence restoration. Though less strongly, the single-base mismatched DNA can also hybridize with the MB. Consequently, a fraction of MBs open and generate fluorescence. This type of detection can be regarded as "analog" detection, in which small difference between target and the single-base mismatched DNA results in small difference in the fluorescence signal. The discrimination ratio (*i.e.*, $R=I_{target}/I_{mismatch}$, where I_{target} and $I_{mismatch}$ are the fluorescence intensity from the target DNA and single-base mismatched DNA, respectively) is usually only ~1-3 [241-243, 245], with the best result of 25 achieved at the optimal target concentrations using gold nanoparticles as the quencher [247].

The hybridization process of DNA with the MB can be described as:

$$MB_{close} \overset{K_b}{\Leftrightarrow} MB_{open}, \tag{6.1}$$

$$MB_{open} + DNA \overset{K_d}{\Leftrightarrow} MB_{open} - DNA, \tag{6.2}$$

where MB_{close} and MB_{open} represent the MB in the close and free open state, respectively. "DNA" represents either target or single-base mismatched DNA. MB_{open}-DNA is the duplex formed through MB and DNA hybridization. K_b and K_d are the dissociation constant and are given by

$$K_b = [MB_{open}]/[MB_{close}], \tag{6.3}$$

$$K_d = [MB_{open}] \cdot [DNA]/[MB_{open} - DNA], \tag{6.4}$$

where [.] denotes the corresponding concentration. K_b and K_d can be calculated from

$$K = \exp(\frac{-\Delta G}{RT}), \tag{6.5}$$

where ΔG is the free energy change associated with the process described in Eqs. (6.1) and (6.2). R is the universal gas constant, and T is temperature.

The fluorescence signal from the MB, F, can be written as:

$$F \propto [MB_{open}] + [MB_{open} - DNA] + \delta[MB_{close}] = \frac{[MB_{open}]^2 + (s_0 + K_d) \cdot [MB_{open}]}{[MB_{open}] + K_d} + \delta[MB_{open}]/K_b, \tag{6.6}$$

where s_0 is the original DNA concentration added to the MB solution. δ is the residual fluorescence from the MB in the close state. $[MB_{open}] = -\frac{P}{2} + \frac{1}{2}\sqrt{P^2 + 4Q}$, where $P = K_d + \frac{s_0 - n_T}{1 + 1/K_b}$ and $Q = \frac{K_d n_T}{1 + 1/K_b}$. n_T is the total MB (or dye) concentration. Fig. 6.1 illustrates the fluorescence (normalized to the highest signal when all MBs are open) for different target and single-base mismatched DNA concentrations.

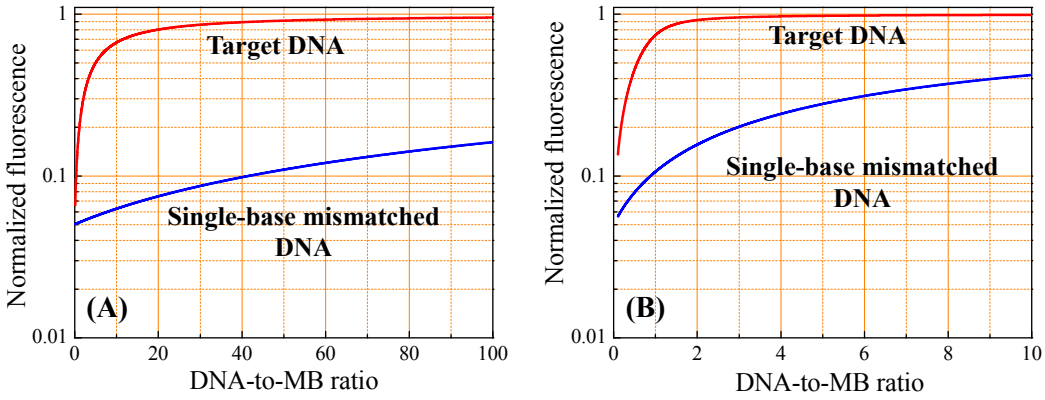

Fig. 6.1 Normalized fluorescence from the MB for different DNA-to-MB ratios. (A) n_T=1 μM. (B) n_T=50 μM. K_b=4x10^{-4} M. K_d=2x10^{-9} M (for the target DNA) and 3x10^{-7} M (for the single-base mismatched DNA). δ=0.05. MB and DNA sequences are listed in Table 6.1.

Table 6.1. MB and DNA sequences used in the experiments

Sample name	Sequence
Molecular beacon (MB)	5'-/**6-FAM**/ CGCTC-TTTTTTTTTTTTTTT-GAGCG /**DABCYL**/-3'
Target DNA	5'-AAAAAAAAAAAAAAG-3'
Single-base mismatched DNA	5'-AAAAAAA**C**AAAAAAG-3'

The theoretical simulation results from Fig. 6.1 show that typically the discrimination ratio in fluorescence between target DNA and SNP is around 20. However, in experiment, the discrimination ratio is usually far less than the theoretical value. We use a poly-A sequence and its single-point mutation for example (see Table 6.1 for sample details), and measure the fluorescence intensity from the target sequence and its SNP, which is presented in Fig. 6.2. Hybridization of the MB with the target DNA or single-base mismatched DNA took place in a micro-quartz cuvette by mixing 35 μL MB with 35 μL DNA sample to the desired final concentrations at room temperature (~27 ^{o}C).

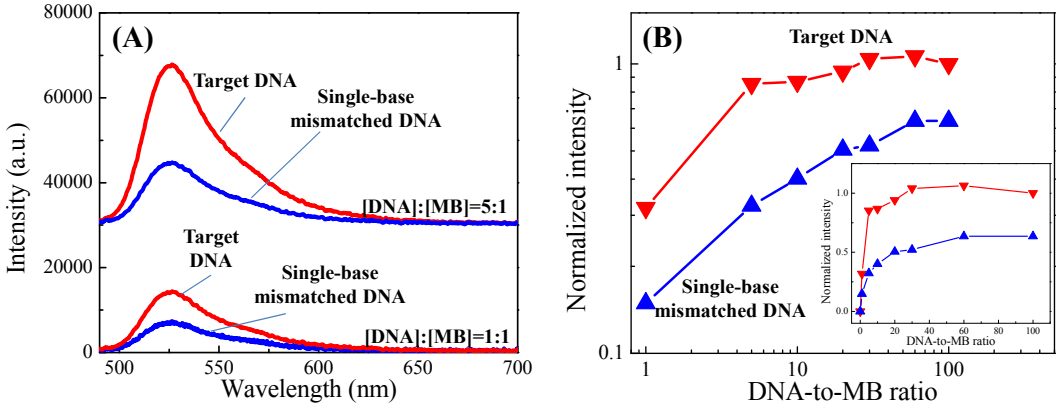

Fig. 6.2 MB fluorescence from the target and the single-base mismatched DNA. (A) Fluorescence spectra for two different [DNA]:[MB] ratios. Curves are vertically shifted for clarity. (B) MB fluorescence signal vs. DNA-to-MB ratio. The signal is normalized to that for [Target DNA]:[MB]=100:1. Inset, the corresponding curves in the linear-linear scale. In all experiments, [MB]=1 μM. MB background is subtracted from all spectra. MB and DNA sequences are listed in Table 6.1.

A laser at 480 nm was used for MB excitation. The fluorescence spectra were recorded by a USB 4000 Miniature Fiber Optic spectrometer (Ocean Optics, FL) for post-analysis. In the experiment, MB concentration is fixed at 1 μM, while DNA-to-MB ratio is varied from 1 to 100. From Fig. 6.2(B) we can see the best discrimination ratio is 2.5 between the target and single-base-mismatched DNA. Such a low discrimination ratio makes it less confident to detect the target DNA from the single-base mismatched DNA. Moreover, it is impossible to directly identify target DNA out of a mixture of DNA of unknown sequences.

6.3 OFRR laser intra-cavity DNA detection

In our intra-cavity SNP detection scheme, we employed the OFRR as the laser cavity, as illustrated in Fig. 6.3. The OFRR is a unique bio-compatible laser, the lasing

properties of which have been studied in Chapter 5. When placed in the OFRR, the MB becomes the gain medium of the OFRR laser, which is modulated by the MB conformational state determined by the hybridization with DNA molecules. Although small hybridization affinity difference between the target and single-base mismatched DNA causes only a small change in the laser gain coefficient, it is this small change that is nonlinearly amplified into orders of magnitude difference in the emission intensity due to the optical feedback provided by the laser cavity. Therefore, utilizing lasing emission

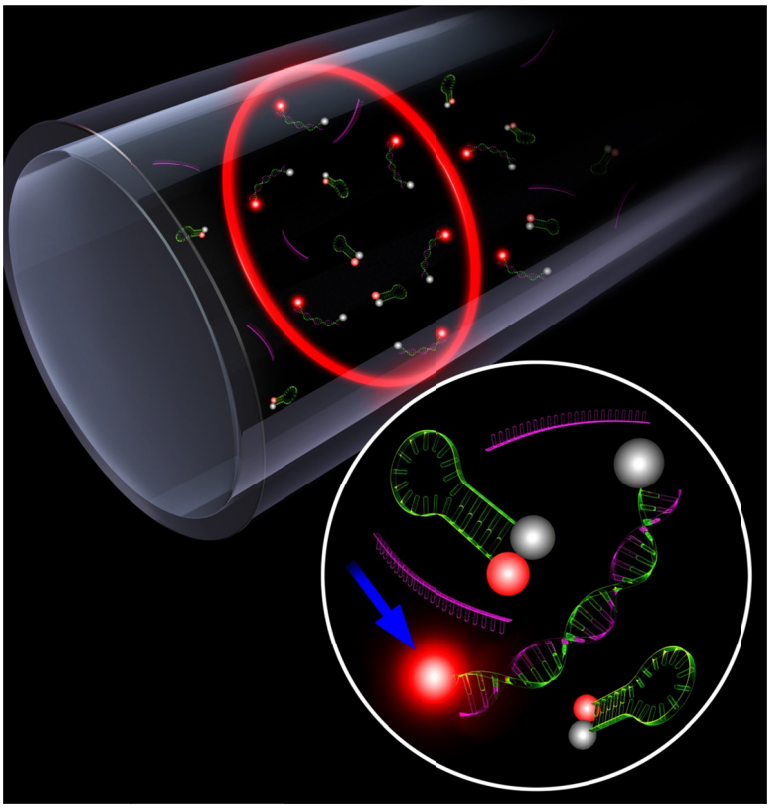

Fig. 6.3 Intra-cavity SNP detection with the OFRR laser. The OFRR cross-section forms the ring resonator. It supports the circulating optical resonant mode of high Q-factor, which interacts evanescently with the MB flowing through the OFRR and provides the optical feedback for MB to lase. Inset, MB fluorescence is quenched when it is in the closed state in which the fluorophore and quencher are in close proximity. MB fluorescence is restored upon hybridization with the target DNA. Blue arrow indicates the external laser pump.

(*i.e.*, stimulated emission) as the sensing signal, the target and single-base mismatched DNA can be easily differentiated with the intra-cavity detection scheme.

6.3.1 Theoretical analysis

For the dye attached to a MB, it can be in one of the following states:

1. MB open, dye in the excited state

2. MB open, dye in the ground state

3. MB closed, dye in the excited state

4. MB closed, dye in the ground state

For the dye molecule in State #3, due to static quenching or rapid non-radiative recombination, we can assume that it does not participate in the lasing process. The MB in the open states (#1 and #2) can be in the free open state (*i.e.*, MB_{open}) or in the hybridized form (*i.e.*, MB_{open}-DNA). For the lasing analysis, they both contribute to the lasing action.

When placed in the OFRR, the MB (or more precisely, the dye labeled on the MB) becomes the gain medium of the OFRR laser and has evanescent-wave coupling with the OFRR resonant modes (details see Chapter 5). The corresponding population inversion condition for such a four-energy-level laser system can be written as[19, 92, 213]:

$$\eta n_1 \sigma_{dye,e}(\lambda_e) \geq \eta(n_T - n_1)\sigma_{dye,a}(\lambda_e) + \eta n_T \sigma_{quencher,a}(\lambda_e) + \frac{2\pi m}{\lambda_e Q_0}, \qquad (6.7)$$

where n_T is the total concentration of the dye (*i.e.*, summation of State #1-#4). n_1 is the concentration of the dye in State #1. $\sigma_{dye,e}$ ($\sigma_{dye,a}$ and $\sigma_{quencher,a}$) is the dye emission cross section (dye absorption cross section and quencher absorption cross section) at the lasing

wavelength (λ_e). η is the fraction of the light in the evanescent field. Q_0 is the OFRR empty-cavity Q-factor. m is the effective refractive index of the circulating optical mode. Here we assume that each MB has only one dye and one quencher attached. At the threshold, Eq. (6.7) becomes:

$$\gamma \approx \frac{\sigma_{dye,a}(\lambda_e) + \sigma_{quencher,a}(\lambda_e)}{\sigma_{dye,e}(\lambda_e)} \cdot [1 + \frac{Q_{abs}}{\eta Q_0}], \tag{6.8}$$

where $\gamma = n_1/n_T$ and

$$Q_{abs} = \frac{2\pi m}{\lambda_e n_T [\sigma_{dye,a}(\lambda_e) + \sigma_{quencher,a}(\lambda_e)]} \tag{6.9}$$

is the Q-factor related to the dye and quencher absorption.

Note that γ depends on the dye concentration as well as the emission/absorption cross sections of the dye and the quencher. For our OFRR system (n_T=50 μM, m=1.40), $Q_{abs} >> \eta Q_0$. Therefore, Eq. (6.8) can be simplified as:

$$\gamma \approx \frac{1}{\sigma_{dye,e}(\lambda_e)} \cdot [\frac{2\pi m}{\lambda_e n_T} \frac{1}{\eta Q_0}]. \tag{6.10}$$

With $\eta Q_0 = 10^5$ and $\sigma_{dye,e} = 4 \times 10^{-16}$ cm^2 that are typically obtained with the OFRR and the dye [92, 254, 255], γ of approximately 10% is obtained, which is similar to that obtained with other dye laser systems (~1-10%) [92, 213]. In the subsequent simulation, we used γ=10%.

Using the rate equations for a four-energy-level system, n_1 can be estimated by[254]:

$$\frac{n_1}{n_{open}} = \frac{I}{I+1}, \tag{6.11}$$

where

$$n_{open} = [MB_{open}] + [MB_{open} - DNA] \tag{6.12}$$

is the concentration of the dye molecules on the open MB (*i.e.*, the summation of State #1 and #2). Here we assume that the dye attached to the closed MB does not contribute to the population of the emissive excited states (*i.e.*, n_1) due to the strong quenching effect. I is dimensionless and is linearly proportional to the pump intensity [254]. Rewriting Eq. (6.11), we arrive at an important lasing threshold condition, which is related to γ:

$$I_{th} = \frac{\gamma}{\Gamma - \gamma}, \tag{6.13}$$

where

$$\Gamma = \frac{n_{open}}{n_T} \tag{6.14}$$

is the fraction of the MBs that are in the open state. Fig. 6.4 shows the normalized lasing threshold for the target and single-base mismatched DNA based on Eqs. (6.12-6.14).

During the laser operation, the lasing emission is a few orders of magnitude stronger than the spontaneous emission [254]. The laser output power is linearly proportional to the pump intensity, I_{pump}, above the lasing threshold [254]:

$$I_{output} \propto (\frac{I_{pump}}{I_{th}} - 1). \tag{6.15}$$

Considering Eqs. (6.13) and (6.15), we arrive at

$$I_{output} \propto I_{pump}(\frac{\Gamma}{\gamma} - 1) - 1. \tag{6.16}$$

Eq. (6.16) enables quantitative measurement of the target DNA concentration. At the fixed pump intensity, the laser output is proportional to Γ and hence the DNA concentration.

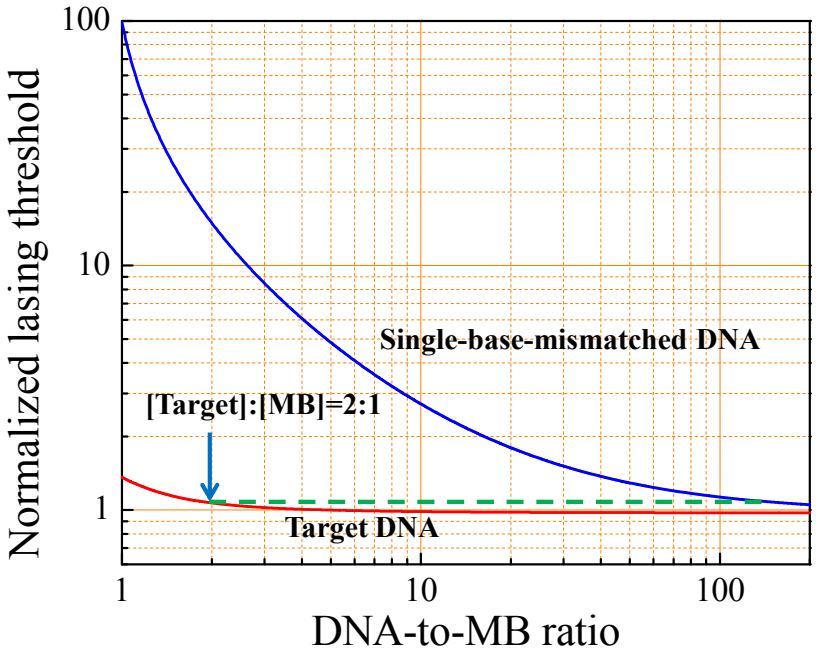

Fig. 6.4 Lasing threshold for various concentrations of the target DNA and single-base mismatched DNA based on Eqs. (6.12-14). The lasing threshold is normalized to the threshold for [target DNA]:[MB]=5:1 (for the purpose of comparison with the experimental results). The dashed horizontal line illustrates that the lasing threshold can be achieved with [Target DNA]:[MB]=2:1, but not until when [Single-base mismatched DNA]:[MB] is larger than 100:1. γ=10%. Other related parameters are the same as in Fig. 6.1(B).

From the theoretical analysis presented above, we can obtain some useful information for laser intra-cavity sensing. Equation (6.13) plays a central role in SNP detection using the MB laser. First, it requires that a minimal fraction of MBs must be open (*i.e.*, $\Gamma=\gamma$) to achieve lasing. Second, it shows that the small difference in Γ between the target and single-base mismatched DNA can be significantly enlarged in the lasing threshold. For example, for Γ=22% (11%) for the target (single-base mismatched) DNA, the conventional MB measurement would yield a discrimination ratio of only 2 in fluorescence. However, for a MB laser with γ=10%, the lasing threshold could be 12

times different. Such large difference in the lasing threshold, particularly at low DNA-to-MB ratios, as clearly exhibited in Figure 6.4, allows for us to easily set the external pump intensity to be above the threshold for the target DNA, but below that for the single-base mismatched DNA. Consequently, the target DNA leads to extremely strong lasing emission (*i.e.*, stimulated emission) whereas the single-base mismatched DNA results only in virtually negligible fluorescence background (*i.e.*, spontaneous emission). Theoretically, a discrimination ratio high as 10^5 can be achieved [254]. Such deep noise (*i.e.*, fluorescence background) suppression mimics the analog-to-digital conversion in electronics, which eliminates the contribution from the mismatched DNA and generates high signal fidelity for us to detect the presence of the target DNA.

6.3.2 Experimental study

To demonstrate the SNP detection with the MB-OFRR laser, we first used simple DNA sequences of poly-A and its single-point mutation [247]. The corresponding MB was labeled with FAM and DABCYL as the fluorophore and quencher (see Table 6.1 for sample details). The experiments were performed isothermally at room temperature (~27 ^{o}C). Figure 6.5 compares the MB emission in the presence of the target DNA and of the single-base mismatched DNA under otherwise the same experimental conditions. With the target DNA, multiple strong lasing peaks occurred at the longer wavelength side of the FAM emission spectrum, which is typical for a multi-mode dye laser like OFRR [213, 255]. In sharp contrast, only weak, featureless fluorescence was observed with the single-base mismatched DNA. If we use the spectrally integrated emission intensity as the sensing signal, a discrimination ratio of 240 is obtained between the target and

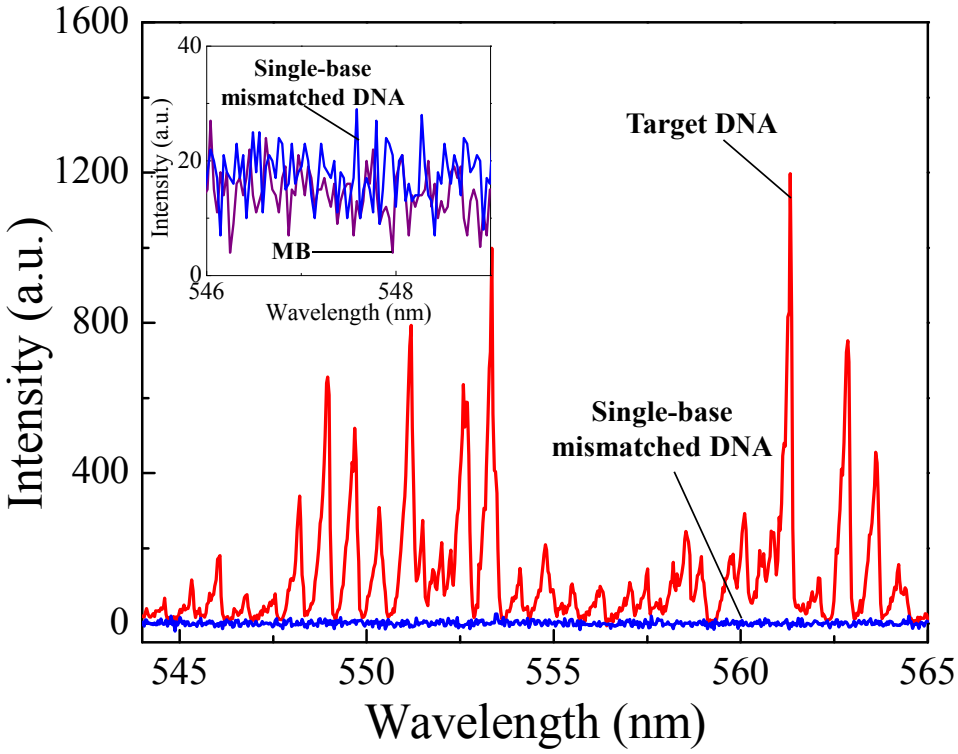

Fig. 6.5 Comparison of the MB emission spectrum in the presence of the target DNA and of the single-base mismatched DNA. The DNA-to-MB molar ratio is 1:1. MB concentration was fixed at 50 μM. The pump energy density was 25.6 μJ/mm^2 at 490.7 nm. The background fluorescence from MB alone is subtracted. Inset shows part of the fluorescence spectra for the MB alone and in the presence of the single-base mismatched DNA, respectively.

mismatched DNA, which represents more than two orders of magnitude improvement over the conventional fluorescence-based SNP detection using the same MB (see Fig. 6.2). Note that, in the OFRR laser, only the MB within the evanescent field of the circulating optical mode (*i.e.*, approximately100 nm region near the inner surface of the OFRR) participated in the lasing emission, whereas all the MBs in the whole OFRR cross section contributed to the fluorescence observed for the mismatched DNA. Therefore, the

actual discrimination ratio could be as high as 10^5, which is typically expected from a laser system [254].

In addition to the MB emission intensity, the lasing threshold can be used to differentiate the target and single-base mismatched DNA. Figure 6.6(A) shows the output intensities extracted from the MB emission spectra as a function of the pump energy density. For the target DNA, the lasing threshold of approximately 1 $\mu J/mm^2$ was achieved (see the inset of Fig. 6.6(A)). When the pump energy density was above 10 $\mu J/mm^2$, the laser output started to saturate. In contrast, no lasing emission was observed for the mismatched DNA, even with the highest possible energy density from the pump laser (100 $\mu J/mm^2$). Such huge difference in the lasing threshold is due to the inability of the mismatched DNA to open adequate MBs to satisfy the requirement of $\Gamma>\gamma$ in equation (6.13). With the increased DNA concentrations while keeping MB concentration unchanged, the laser can be achieved for both target and mismatched DNA, as shown in Fig. 6.6(B)-(D), with the progressively decreased lasing threshold. The inset of Fig. 6.6(B) plots the normalized thresholds obtained from the experiments and calculated from equations (6.12-6.14). Although many details are omitted (such as multi-mode lasing), our theoretical model agrees qualitatively with the experimental results, suggesting that it reflects the essence of the MB-OFRR laser system and provides an insight into the corresponding SNP detection scheme.

Direct and specific detection of the target DNA from a pool of single-base mismatched DNA molecules provides an excellent test-bed to examine the SNP detection selectivity. Unfortunately, to date, nearly all conventional MB SNP detection schemes can only detect the pure target or mismatched DNA individually and then theoretically

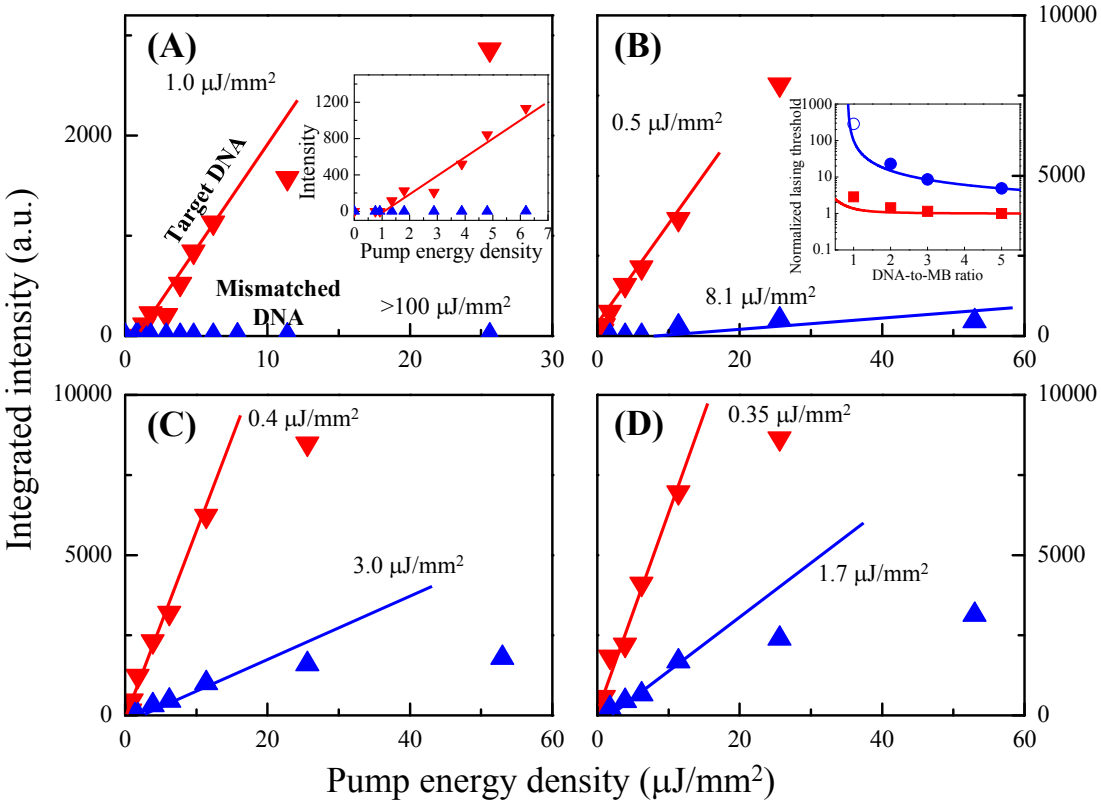

Fig. 6.6 Spectrally integrated MB emission intensity vs. the pump energy density for various concentrations of the target and single-base mismatched DNA. (A)-(D), [DNA]:[MB]=1:1, 2:1, 3:1, and 5:1, respectively. Upper and bottom data points in each figure are for the target and single-base mismatched DNA, respectively. Upper and bottom solid lines are the linear fit for the pump energy density above the lasing threshold. The lasing threshold is labeled near the corresponding curves. No lasing emission was achieved with the single-based mismatched DNA in (A), even with the highest possible pump energy density (~100 μJ/mm^2). The MB concentration was fixed at 50 μM. Spectral integration takes place from 544 nm to 565 nm. Inset in (A) shows the magnified part of (A). Inset in (B) shows the normalized lasing thresholds for various concentrations of the target and single-base mismatched DNA presented in (A)-(D). Upper and bottom data points are for the target and single-base mismatched DNA, respectively. The open circle at DNA-to-MB ratio of 1 is obtained using the estimated threshold (100 μJ/mm^2), since no lasing was achieved. Solid lines are the magnified part of Fig. 6.4. Both experimental and theoretical results are normalized to the threshold corresponding to [Target DNA]:[MB]=5:1.

estimate the fractional target DNA can be detected [241, 242, 246, 247], since the signal from a DNA mixture becomes very difficult to de-convolve due to the small fluorescence difference between the target and the mismatched DNA. In contrast, as the intra-cavity detection provides the "clear-cut" analog-to-digital type conversion, the signal generated by the mismatched DNA is completely suppressed and thus does not interfere with the positive identification of the target DNA. To verify this, in Fig. 6.7, we set the pump intensity slightly higher than the threshold for the target DNA at 2:1 molar ratio with respect to the MB, but lower than that for the mismatched DNA (see Fig. 6.4 for illustration). As a negative control, in Fig. 6.7(a)-(e) no lasing emission was observed for the single-base mismatched DNA even at an extremely high concentration ([Single-base mismatched DNA]:[MB]=100:1). However, strong lasing emission emerged when small amount of the target DNA was added, thus allowing us to positively identify the presence of 1 target DNA out of 50 single-base mismatched DNA molecules.

The OFRR laser can further be used to quantify the target DNA concentration. Based on equations (6.15) and (6.16), the output power is linearly proportional to the pump energy density above the threshold or to the fractional MB that is open (Γ) above the minimal fractional MB required for lasing (γ). Figure 6.8 plots the lasing emission spectra for different concentrations of the target DNA for fixed MB concentration at fixed pump energy density, and clearly verifies the relationship predicted by equation (6.16).

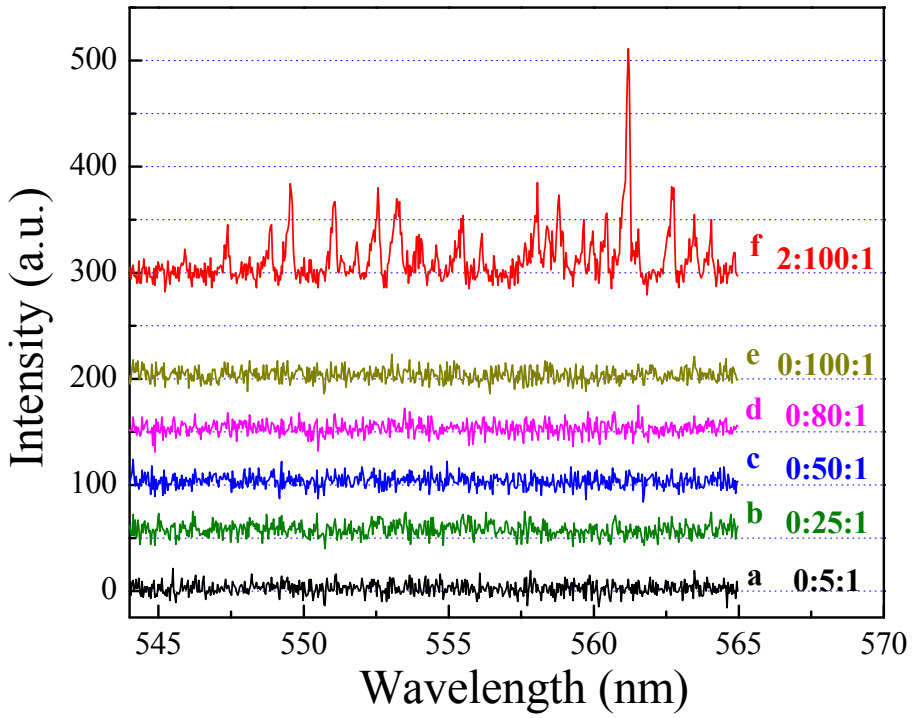

Fig. 6.7 Selective detection of the target DNA from high concentrations of the single-base mismatched DNA. a-e, negative controls. No lasing emission observed from a wide range of concentrations of single-base mismatched DNA samples in the absence of the target DNA. The molar ratio of the target DNA, single-base mismatched DNA, and the MB, *i.e.,* [Target DNA]:[Single-base mismatch DNA]:[MB], is labeled on the right side of the corresponding curves. f, Positive control. Lasing emission emerged when small quantity of target DNA was added in the high concentration of single-base mismatched DNA. During the experiments, the MB concentration was fixed at 50 μM and the pump energy density was 0.8 μJ/mm^2, slightly higher than the lasing threshold for the target DNA given in Figure 6.6(B). Curves are vertically shifted for clarity.

Table 6.2 MB and DNA sequences used in the experiments for cancer marker detection

Sample name	Sequence
Molecular beacon (MB-BRCA1)	5'-/**6-FAM**/ CCTAGCC-CCTATGTATGC TCTTTGTTGT-GGCTAGG /**DABCYL**/-3'
Target-BRCA1	5'-TAAC-ACAACAAAGAGCATACATAGG-GTTT-3'
SNP-M	5'-TAAC-ACAACAAAGA**A**CATACATAGG-GTTT-3'
SNP-E	5'-TAAC-ACAACAAAGAGCATACAT**G**GG-GTTT-3'

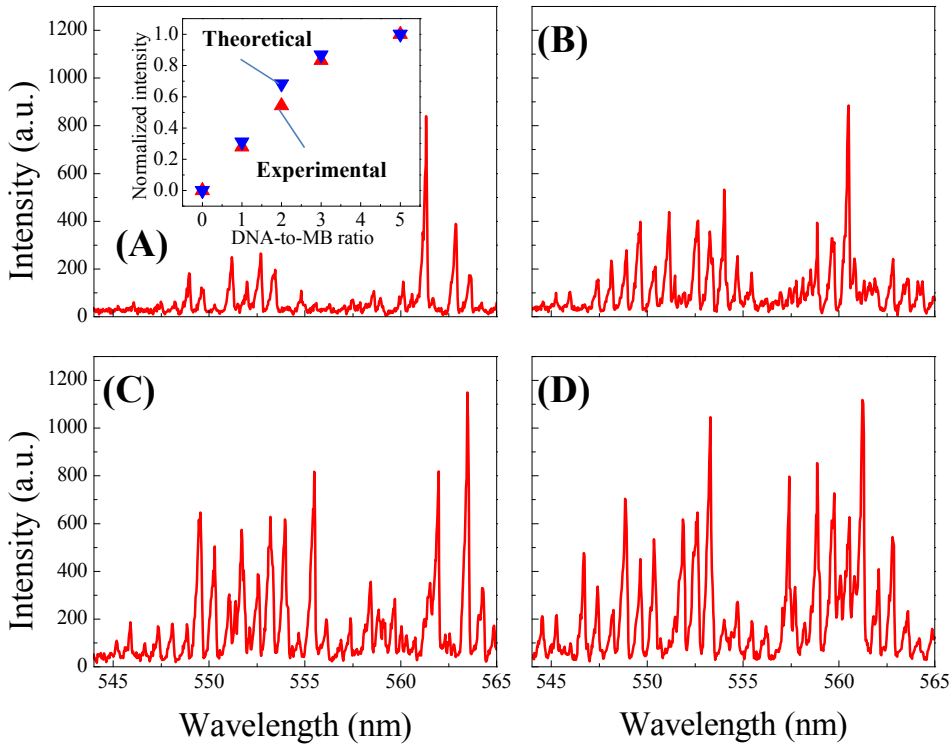

Fig. 6.8 Lasing emission spectrum of the MB hybridized with various concentrations of the target DNA. (A)-(D), [Target DNA]:[MB]=1:1, 2:1, 3:1, and 5:1, respectively. The MB concentration was fixed at 50 μM and the pump energy density was 6.2 μJ/mm^2 at 490.7 nm. Inset shows the spectrally integrated intensity from 544 nm to 565 nm (normalized to the highest output) obtained from (A)-(D), along with the normalized theoretical results based on equation (6.16).

To further validate our method, we used more complicated DNA sequences, breast cancer and ovarian cancer gene, BRCA1, and its single-point mutations. The sequences for the MB, target DNA, and single-base mismatched DNA are given in Table 6.2. In particular, for the single-base mismatched sequences, the mutation occurred in the middle (SNP-M) and at the end (SNP-E) of the sequence, respectively. For comparison purposes, all the sequences are the same as those in Ref. [243], in which the conventional MB method was used and showed a very small discrimination ratio of 1.5 (1.2) between

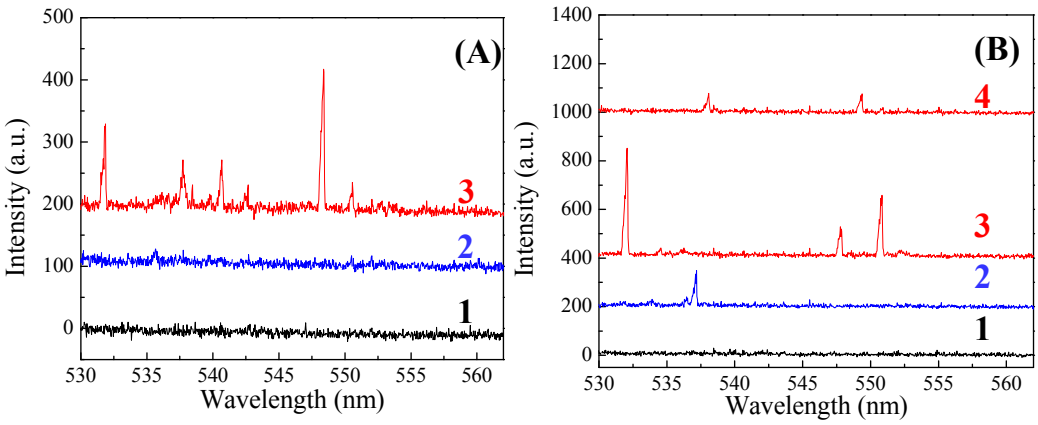

Fig. 6.9 Comparison of the MB emission spectrum in the presence of the target DNA and of the single-base mismatched DNA. (A), [DNA]:[MB]=1:1. Pump energy density was 3 μJ/mm^2 for Curves 1-3. (B), [DNA]:[MB]=5:1. Pump energy density was 1 μJ/mm^2 for Curves 1-3 and 3.2 μJ/mm^2 for Curve 4. In both (A) and (B), Curve 1: SNP-M in buffer. Curve 2: SNP-E in buffer. Curve 3: target DNA in buffer. Curve 4: target DNA in 50% serum. MB concentration was fixed at 50 μM. Curves are vertically shifted for clarity.

the target and SNP-M (SNP-E). Figure 6.9(A) plots the spectra for [DNA]:[MB]=1:1 and clearly shows that our method is capable of differentiating the target and the mismatched DNA (discrimination ratio > 100), regardless of the mismatch position. With the increased DNA concentration (Fig. 6.9(B)), the lasing emission can also be achieved for SNP-E, but not for SNP-M. Such difference between SNP-E and SNP-M is due to the higher affinity of SNP-E for the MB, which is consistent with the lower discrimination ratio observed in SNP-E using the conventional MB method [243]. Note that although both target and SNP-E can lase at high concentrations, the difference in the corresponding lasing threshold still allows us to differentiate the target from the mismatched DNA (SNP-E and SNP-M), as shown in Fig. 6.10. For a given DNA concentration, the target has the lowest lasing threshold, whereas SNP-M has the highest.

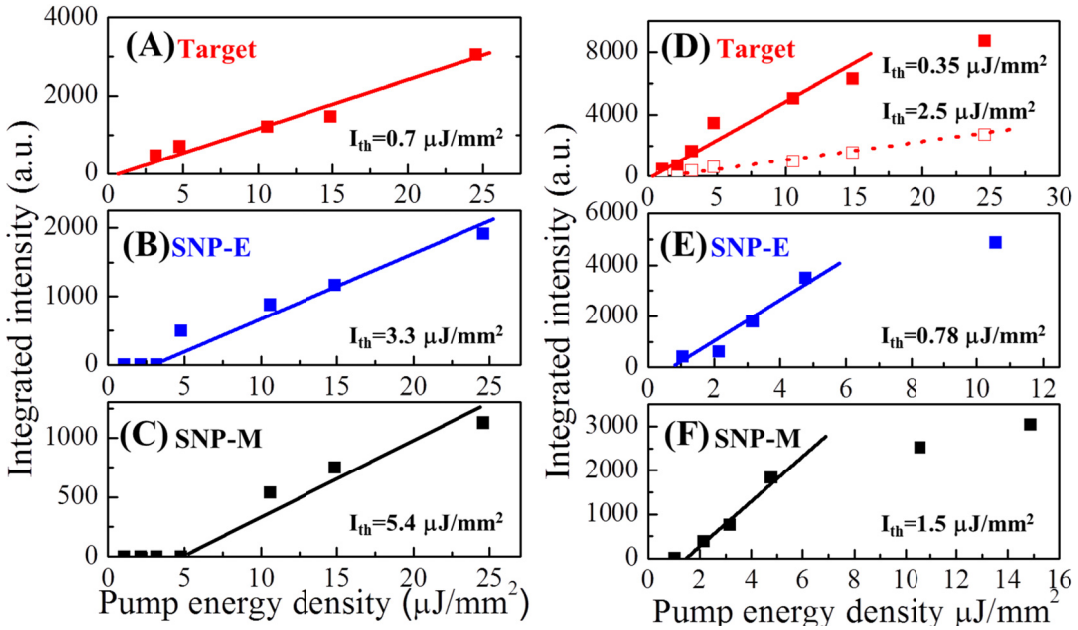

Fig. 6.10 Spectrally integrated MB emission intensity vs. the pump energy density for various concentrations of the target and single-base mismatched DNA. (A)-(C), [DNA]:[MB]=1:1. (D)-(F), [DNA]:[MB]=5:1. Solid lines are the linear fit for the pump energy density above the lasing threshold. The lasing threshold is labeled near the corresponding curves. Hollow squares in d are the spectrally integrated intensity obtained when the target and MB ([DNA]:[MB]=5:1) were dissolved in 50% serum. Dotted line is the corresponding linear fit.

So far, all the experiments were performed in buffer solution. When samples are in other media such as serum, the value of Γ and/or γ may change. For example, when serum is used, γ may increase due to the additional loss introduced by serum absorption. Nevertheless, the detection principle discussed in this paper should still be valid. As shown by Curve 4 in Fig. 6.9(B), the lasing emission can be obtained even when the DNA samples were in 50% serum. The corresponding lasing threshold curve plotted in Fig. 6.10(D) shows that the lasing threshold is approximately 2.5 μJ/mm^2, which, as expected, is much higher than that when the sample is in buffer solution. Using equation (6.13) and assuming that serum does not affect the affinity between DNA and the MB *(i.e.*, $\Gamma_{serum}=\Gamma_{buffer}$, where $\Gamma_{serum\ (buffer)}$ is the fraction of the open MBs when samples are in

serum (buffer)), we estimate that $\gamma_{serum}=2.76\gamma_{buffer}$. Because of this increased γ, the necessary condition, $\Gamma_{serum}>\gamma_{serum}$, can no longer be satisfied for SNP-E and SNP-M in serum for both [DNA]:[MB]=1:1 and 5:1. Consequently, no lasing emission can be achieved for SNP-E and SNP-M in serum, thus allowing us to differentiate the target DNA from the single-base mismatched ones.

6.4 Conclusion

The significance of this work lies in both optofluidics and biotechnology. From the optofluidics perspective, our work marks, to the best of our knowledge, the first application of active intra-cavity biomolecular detection using optofluidic lasers. It proves the tremendous capability of the optofluidic laser in biochemical analysis. The same detection scheme can readily be adapted for all different types of optofluidic lasers [19] for highly sensitive and selective intra-cavity bio-analysis, thus opening a door to a number of research areas in optofluidics.

From the biotechnology perspective, our method provides a new detection paradigm that is potentially capable of distinguishing two DNA sequences with small thermodynamic differences and even directly measuring the target DNA from mixed samples with unprecedented selectivity. Although the detection method was demonstrated with SNP and MB probes, the same concept can be applied in differentiating other small differences in DNA sequences, such as DNA methylation [244], where DNA sequences are differed by only one or a few methylated cytosines, and in the situation where linear DNA probes are used.

Likewise, future research will involve studies on both photonic side and biological side. On the photonic side, we will increase the effective Q-factor (*i.e.*, ηQ_0 in equation (6.8)) to further improve the OFRR detection performance. With a thinner wall thickness, stronger interaction between the optical mode and the MB can be obtained. In fact, lasing emission with a dye concentration of 1 μM was recently achieved using an OFRR with 600 nm wall thickness [256]. Other types of high-Q optical cavities can also be explored [19, 257, 258] that may result in lower MB/DNA concentrations and reduced sample volumes. Microfluidics to generate droplets on-demand will be built for more efficient and rapid sample delivery (>3,000 droplets per second) with 0.1-1 nL sample volume [243, 259]. Such a low sample volume, accompanied by low sample concentration (<1 μM), suggests that only fewer than 10^7 DNA molecules are needed for selective detection [260]. Additionally, an optical fiber taper will also be used to exclusively couple the lasing emission out into the detector [92], thus the theoretical discrimination ratio (~10^5) may become approachable. Moreover, different fluorophores (such as dyes and quantum dots) and quenchers (such as organic quencher and metallic nanoparticles) will be explored for possible multiplexed detection. Finally, temperature ramping can be implemented to further optimize the detection [246]. On the biological side, our work will be extended to differentiation of DNA methylation [244], detection of microRNA [261], high resolution DNA melting analysis [244, 262], and even monitoring of the biological processes occurring inside a cell [263].

Chapter 7

Summary and Future Work

In the preceding chapters I have presented the background and motivation of developing the OFRR platform. Fabrication, characterization, and fundamental working principles of the OFRR were described in particular detail. Based on this platform, two applications of the OFRR were extensively studied, chemical vapor detection and microfluidic laser intra-cavity DNA detection.

In the chemical vapor detection project, the OFRR gas sensing platform was first built and tested with representative gas analytes at different concentrations. The OFRR features rapid response to chemical vapors, owing to its efficient fluidics. The WGM spectral shift is linearly proportional to the vapor concentrations. Additionally, the theoretical analysis was performed on the OFRR gas sensing using a four-layer Mie model, which provides guidelines to the sensor design. To improve the gas sensing specificity, the OFRR sensing technique was integrated with GC separation technology, and the OFRR-based μGC system was developed. The dual use of the OFRR capillary as a separation column and an optical detector renders the OFRR-based μGC system unique multi-point on column detection capability. Rapid detection of DNT vapors out of interfering analytes was demonstrated using the OFRR-μGC. A tandem-column setting of OFRR-μGC was further studied to enhance the chromatographic resolution. A vapor mixture of twelve analytes of different volatilities and polarities are separated and detected within four minutes using the tandem-column OFRR-μGC system.

The second project investigated the active sensing based on the OFRR microlaser. Compared to the passive cavity sensing, the active cavity sensing offers potentially high selectivity and sensitivity. However, this area remains largely yet unexplored. Based on the OFRR, we have developed, for the first time, bio-compatible optofluidic lasers. DNA molecules can be incorporated into the laser gain medium and control the lasing emission properties through efficient FRET. This platform was further employed to explore the highly selective intra-cavity bimolecular detection. Two orders of magnitude improvement in detection selectivity was achieved over the conventional fluorescence detection method in differentiating the target and single-base mismatched DNA sequences.

The future research work will focus on the following aspects. First and foremost, continuous improvement in the OFRR cavity parameter, Q/V, will be the key to improving the LOD in OFRR gas sensing and to lowering the lasing threshold (or lowering gain medium concentration) in OFRR microlasers. While the OFRR already has an ultra-high Q-factor ($>10^7$), the lack of optical confinement in the capillary axial direction causes a relative large mode volume for the WGM. To solve this problem while preserving the efficient capillary microfluidics, a bubble shaped OFRR structure is proposed and currently under investigation [256, 264]. The WGM of this structure is under true three-dimensional confinement, which will further increase the Q-factor and dramatically decrease the mode volume compared to the straight capillary based OFRR. The efficient capillary microfluidics can also be preserved in the bubble shaped OFRR.

Second, for the OFRR-μGC system, efforts will be placed on system integration and field deployment. Pre-concentrators and pumps will be used to replace the gas

injector used in the current configuration to make the entire OFRR-μGC system fit into a portable briefcase. We envision that a broad range of field applications can be carried out with the future version of OFRR-μGC system.

Third, my work on the optofluidic laser intra-cavity detection has opened a door to a variety of highly sensitive and highly selective biosensing applications. An immediate step will be to utilize the bubble-shaped OFRR mentioned above to achieve DNA detection in the nano-molar range. If successful, the sensing platform developed in this thesis will be very useful in differentiating DNA sequences with very small difference (such as in the case of DNA methylation detection and microRNA detection), which is significant not only in fundamental biochemical research, but also in clinical applications.

Bibliography

1. A. Serpenguzel, and S. Arnold, "Excitation of resonances of microspheres on an optical fiber," Opt. Lett. **20**, 654-656 (1995).
2. F. Vollmer, D. Braun, A. Libchaber, M. Khoshsima, I. Teraoka, and S. Arnold, "Protein detection by optical shift of a resonant microcavity," Appl. Phys. Lett. **80**, 4057-4059 (2002).
3. A. Ksendzov, and Y. Lin, "Integrated optics ring-resonator sensors for protein detection," Opt. Lett. **30**, 3344-3346 (2005).
4. Y. Sun, and X. Fan, "Optical ring resonators for biochemical and chemical sensing," Anal. Bioanal. Chem. **399**, 205-211 (2011).
5. T. J. Kippenberg, and K. J. Vahala, "Cavity Optomechanics: Back-Action at the Mesoscale," Science **321** (2007).
6. K. J. Vahala, "Optical microcavities," Nature **424**, 839-846 (2003).
7. T. J. Kippenberg, J. Kalkman, A. Polman, and K. J. Vahala, "Demonstration of an erbium-doped microdisk laser on a silicon chip," Phys. Rev. A **74**, 051802 (2006).
8. M. Cai, O. Painter, and K. J. Vahala, "Fiber-coupled microsphere laser," Opt. Lett. **25**, 1430-1432 (2000).
9. S. M. Spillane, T. J. Kippenberg, and K. J. Vahala, "Ultralow-threshold Raman laser using a spherical dielectric microcavity," Nature **415**, 621-623 (2002).
10. H.-B. Lin, J. D. Eversole, and A. J. Campillo, "Spectral properties of lasing microdroplets," J. Opt. Soc. Am. B **9**, 43-50 (1992).
11. S.-X. Qian, J. B. Snow, H.-M. Tzeng, and R. K. Chang, "Lasing Droplets: Highlighting the Liquid-Air Interface by Laser Emission," Science **231**, 486-488 (1986).
12. S. I. Shopova, H. Zhu, X. Fan, and P. Zhang, "Optofluidic ring resonator based dye laser," Appl. Phys. Lett. **90**, 221101 (2007).
13. M. Gersborg-Hansen, and A. Kristensen, "Tunability of optofluidic distributed feedback dye lasers," Opt. Express **15**, 137-142 (2007).
14. C. Monat, P. Domachuk, and B. J. Eggleton, "Integrated optofluidics: A new river of light," Nature Photon. **1**, 106-114 (2007).
15. C. Monat, P. Domachuk, C. Grillet, M. Collins, B. Eggleton, M. Cronin-Golomb, S. Mutzenich, T. Mahmud, G. Rosengarten, and A. Mitchell, "Optofluidics: a novel generation of reconfigurable and adaptive compact architectures," Microfluid. Nanofluid. **4**, 81-95 (2008).
16. D. Psaltis, S. R. Quake, and C. Yang, "Developing optofluidic technology through the fusion of microfluidics and optics," Nature **442**, 381-386 (2006).
17. V. R. Horowitz, D. D. Awschalom, and S. Pennathur, "Optofluidics: field or technique?," Lab Chip **8**, 1856-1863 (2008).
18. U. Levy, and R. Shamai, "Tunable optofluidic devices," Microfluid. Nanofluid. **4**, 97-105 (2008).
19. Z. Li, and D. Psaltis, "Optofluidic dye lasers," Microfluid. Nanofluid. **4**, 145–158 (2008).
20. H. Schmidt, and A. R. Hawkins, "The photonic integration of non-solid media using optofluidics," Nature Photon., doi: 10.1038/nphoton.2011.1163 (2011).

21. X. Fan, and I. M. White, "Optofluidic Microsystems for Chemical and Biological Analysis," Nature Photon., doi: 10.1038/nphoton.2011.1206 (2011).
22. E. Krioukov, D. J. W. Klunder, A. Driessen, J. Greve, and C. Otto, "Integrated optical microcavities for enhanced evanescent-wave spectroscopy," Opt. Lett. **27**, 1504-1506 (2002).
23. F. Vollmer, S. Arnold, D. Braun, I. Teraoka, and A. Libchaber, "Multiplexed DNA Quantification by Spectroscopic Shift of Two Microsphere Cavities," Biophys. J. **85**, 1974-1979 (2003).
24. A. Ksendzov, M. L. Homer, and A. M. Manfreda, "Integrated optics ring-resonator chemical sensor with polymer transduction layer," Electron. Lett. **40**, 63-65 (2004).
25. N. M. Hanumegowda, I. M. White, and X. Fan, "Aqueous mercuric ion detection with microsphere optical ring resonator sensors," Sens. Actuators B **120**, 207-212 (2006).
26. H.-C. Ren, F. Vollmer, S. Arnold, and A. Libchaber, "High-Q microsphere biosensor - analysis for adsorption of rodlike bacteria," Opt. Express **15**, 17410-17423 (2007).
27. H. Zhu, I. M. White, J. D. Suter, M. Zourob, and X. Fan, "Integrated Refractive Index Optical Ring Resonator Detector for Capillary Electrophoresis," Anal. Chem. **79**, 930-937 (2007).
28. H. Zhu, I. H. White, J. D. Suter, M. Zourob, and X. Fan, "Opto-fluidic micro-ring resonator for sensitive label-free viral detection," Analyst **133**, 356-360 (2008).
29. F. Vollmer, S. Arnold, and D. Keng, "Single virus detection from the reactive shift of a whispering-gallery mode," Proc. Natl. Acad. Sci. USA **105**, 20701-20704 (2008).
30. G. Yang, I. M. White, and X. Fan, "An opto-fluidic ring resonator biosensor for the detection of organophosphorus pesticides," Sens. Actuators B **133**, 105-112 (2008).
31. H. Zhu, P. S. Dale, C. W. Caldwell, and X. Fan, "Rapid, label-free detection of breast cancer biomarker CA15-3 in clinical human serum samples with opto-fluidic ring resonator sensors," Anal. Chem. **81**, 9858-9865 (2009).
32. A. L. Washburn, L. C. Gunn, and R. C. Bailey, "Label-free quantitation of a cancer biomarker in complex media using silicon photonic microring resonators," Anal. Chem. **81**, 9499-9506 (2009).
33. M. Iqbal, M. A. Gleeson, B. Spaugh, F. Tybor, W. G. Gunn, M. Hochberg, T. Baehr-Jones, R. C. Bailey, and L. C. Gunn, "Label-free biosensor arrays based on silicon ring resonators and high-speed optical scanning instrumentation," IEEE J. Sel. Top. Quant. Electron. **16**, 654-661 (2010).
34. M. S. Luchansky, and R. C. Bailey, "Silicon Photonic Microring Resonators for Quantitative Cytokine Detection and T-Cell Secretion Analysis," Anal. Chem. **82**, 1975–1981 (2010).
35. A. J. Qavi, and R. C. Bailey, "Multiplexed Detection and Label-Free Quantitation of MicroRNAs Using Arrays of Silicon Photonic Microring Resonators," Angew. Chem. Int. Ed. **49**, 4608 –4611 (2010).

36. A. L. Washburn, M. S. Luchansky, A. L. Bowman, and R. C. Bailey, "Quantitative, label-free detection of five protein biomarkers using multiplexed arrays of silicon photonic microring resonators," Anal. Chem. **82**, 69-72 (2010).
37. J. G. Zhu, S. K. Ozdemir, Y. F. Xiao, L. Li, L. N. He, D. R. Chen, and L. Yang, "On-chip single nanoparticle detection and sizing by mode splitting in an ultrahigh-Q microresonator," Nature Photon. **4**, 46-49 (2010).
38. Y. Sun, J. Liu, D. J. Howard, X. Fan, G. Frye-Mason, Shiou-jyh Ja, and A. K. Thompson, "Rapid tandem-column micro-gas chromatography based on optofluidic ring resonators with multi-point on column detection," Analyst **135**, 165-171 (2010).
39. J. D. Suter, D. J. Howard, H. Shi, C. W. Caldwell, and X. Fan, "Label-free DNA methylation analysis using opto-fluidic ring resonators " Biosens. Bioelectron. **26**, 1016-1020 (2010).
40. V. E. Roman, J. Popp, M. H. Fields, and W. Kiefer, "Species identification of multicomponent microdroplets by seeding stimulated Raman scattering," J. Opt. Soc. Am. B **16**, 370-375 (1999).
41. J. B. Snow, S.-X. Qian, and R. K. Chang, "Stimulated Raman scattering from individual water and ethanol droplets at morphology-dependent resonances," Opt. Lett. **10**, 37-39 (1985).
42. M. Saito, H. Shimatani, and H. Naruhashi, "Tunable whispering gallery mode emission from a microdroplet in elastomer," Opt. Express **16**, 11915-11919 (2008).
43. M. Tanyeri, R. Perron, and I. M. Kennedy, "Lasing droplets in a microfabricated channel," Opt. Lett. **32**, 2529-2531 (2007).
44. M. Hossein-Zadeh, and K. J. Vahala, "Fiber-taper coupling to Whispering-Gallery modes of fluidic resonators embedded in a liquid medium," Opt. Express **14**, 10800-10810 (2006).
45. M. L. Gorodetsky, and V. S. Ilchenko, "Optical microsphere resonators: optimal coupling to high-Q whispering-gallery modes," J. Opt. Soc. Am. B **16**, 147-154 (1999).
46. N. M. Hanumegowda, I. M. White, H. Oveys, and X. Fan, "Label-free protease sensors based on optical microsphere resonators," Sens. Lett. **3**, 1-5 (2005).
47. I. Teraoka, S. Arnold, and F. Vollmer, "Perturbation approach to resonance shifts of whispering-gallery modes in a dielectric microsphere as a probe of a surrounding medium," J. Opt. Soc. Am. B **20**, 1937-1946 (2003).
48. N. M. Hanumegowda, C. J. Stica, B. C. Patel, I. White, and X. Fan, "Refractometric sensors based on microsphere resonators," Appl. Phys. Lett. **87**, 201107 (2005).
49. S. Arnold, M. Khoshsima, I. Teraoka, S. Holler, and F. Vollmer, "Shift of whispering-gallery modes in microspheres by protein adsorption," Opt. Lett. **28**, 272-274 (2003).
50. M. Charlebois, A. Paquet, L. S. Verret, K. Boissinot, M. Boissinot, M. G. Bergeron, and C. N. Allen, "Toward Automatic Label-Free Whispering Gallery Modes Biodetection with a Quantum Dot-Coated Microsphere Population," Nanoscale Res. Lett. **5**, 524-532 (2010).

51. G. Schweiger, R. Nett, and T. Weigel, "Microresonator array for high-resolution spectroscopy," Opt. Lett. **32**, 2644-2646 (2007).
52. J. Lutti, W. Langbein, and P. Borri, "A monolithic optical sensor based on whispering-gallery modes in polystyrene microspheres," Appl. Phys. Lett. **93**, 151103 (2008).
53. X. Ma, J. Q. Lu, R. S. Brock, K. M. Jacobs, P. Yang, and X.-H. Hu, "Determination of complex refractive index of polystyrene microspheres from 370 to 1610 nm," Phys. Med. Biol. **48**, 4165-4172 (2003).
54. P. Zijlstra, K. L. van der Molen, and A. P. Mosk, "Spatial refractive index sensor using whispering gallery modes in an optically trapped microsphere," Appl. Phys. Lett. **90**, 161101 (2007).
55. Q. Xu, V. R. Almeida, R. R. Panepucci, and M. Lipson, "Experimental demonstration of guiding and confining light in nanometer-size low-refractive-index material," Opt. Lett. **29**, 1626-1628 (2004).
56. A. Yalcin, K. C. Popat, J. C. Aldridge, T. A. Desai, J. V. Hryniewicz, N. Chbouki, B. E. Little, O. King, V. Van, S. Chu, D. Gill, M. Anthes-Washburn, M. S. Unlu, and B. B. Goldberg, "Optical Sensing of Biomolecules Using Microring Resonators," IEEE J. Sel. Top. Quant. Electron. **12**, 148-155 (2006).
57. A. M. Armani, and K. J. Vahala, "Heavy water detection using ultra-high-Q microcavities," Opt Lett **31**, 1896-1898 (2006).
58. A. Ramachandran, S. Wang, J. Clarke, S. J. Ja, D. Goad, L. Wald, E. M. Flood, E. Knobbe, J. V. Hryniewicz, S. T. Chu, D. Gill, W. Chen, O. King, and B. E. Little, "A universal biosensinig platform based on optical micro-ring resonators," Biosens. Bioelectron. **23**, 939-944 (2008).
59. C. A. Barrios, M. J. Banuls, V. Gonzalez-Pedro, K. B. Gylfason, B. Sanchez, A. Griol, A. Maquieira, H. Sohlstrom, M. Holgado, and R. Casquel, "Label-free optical biosensing with slot-waveguides," Opt. Lett. **33**, 708-710 (2008).
60. C. F. Carlborg, K. B. Gylfason, A. Kaźmierczak, F. Dortu, M. J. B. Polo, A. M. Catala, G. M. Kresbach, H. Sohlström, T. Moh, L. Vivien, J. Popplewell, G. Ronan, C. A. Barrios, G. Stemme, and W. v. d. Wijngaart, "A packaged optical slot-waveguide ring resonator sensor array for multiplex label-free assays in labs-on-chips," Lab Chip **10**, 281–290 (2010).
61. D.-X. Xu, M. Vachon, A. Densmore, R. Ma, A. Delâge, S. Janz, J. Lapointe, Y. Li, G. Lopinski, D. Zhang, Q. Y. Liu, P. Cheben, and J. H. Schmid, "Label-free biosensor array based on SOI ring resonators addressed using the WDM approach," Opt. Lett. **35**, 2771-2773 (2010).
62. N. A. Yebo, P. Lommens, Z. Hens, and R. Baets, "An integrated optic ethanol vapor sensor based on a silicon-on-insulator microring resonator coated with a porous ZnO film," Opt. Express **18**, 11859-11866 (2010).
63. C.-Y. Chao, W. Fung, and L. J. Guo, "Polymer microring resonators for biochemical sensing applications," IEEE J. Sel. Top. Quant. Electron. **12**, 134-142 (2006).
64. C.-Y. Chao, and L. J. Guo, "Polymer microring resonators fabricated by nanoimprint technique," J. Vac. Sci. Technol. B **20**, 2862-2866 (2002).

65. K. D. Vos, I. Bartolozzi, E. Schacht, P. Bienstman, and R. Baets, "Silicon-on-Insulator microring resonator for sensitive and label-free biosensing," Opt. Express **15**, 7610-7615 (2007).
66. I. M. White, H. Oveys, and X. Fan, "Liquid Core Optical Ring Resonator Sensors," Opt. Lett. **31**, 1319-1321 (2006).
67. V. Zamora, A. Diez, M. V. Andres, and B. Gimeno, "Refractometric sensor based on whispering-gallery modes of thin capillaries," Opt. Express **15**, 12011-12016 (2007).
68. A. Bernardi, S. Kiravittaya, A. Rastelli, R. Songmuang, D. J. Thurmer, M. Benyoucef, and O. G. Schmidt, "On-chip Si/SiO_x microtube refractometer," Appl. Phys. Lett. **93**, 094106 (2008).
69. O. G. Schmidt, and K. Eberl, "Thin solid films roll up into nanotubes," Nature **410**, 168 (2001).
70. V. Y. Prinz, V. A. Seleznev, A. K. Gutakovsky, A. V. Chehovskiy, V. V. Preobrazhenskii, M. A. Putyato, and T. A. Gavrilova, "Free-standing and overgrown InGaAs/GaAs nanotubes, nanohelices and their arrays," Physica E **6**, 828-831 (2000).
71. R. Songmuang, C. Deneke, and O. G. Schmidt, "Rolled-up micro- and nanotubes from single-material thin films," Appl. Phys. Lett. **89**, 223109 (2006).
72. S. Mendach, R. Songmuang, S. Kiravittaya, A. Rastelli, M. Benyoucef, and O. G. Schmidt, "Light emission and wave guiding of quantum dots in a tube," Appl. Phys. Lett. **88**, 111120 (2006).
73. R. Songmuang, A. Rastelli, S. Mendach, C. Deneke, and O. G. Schmidt, "From rolled-up Si microtubes to SiO_x/Si optical ring resonators," Microelectron. Eng. **84**, 1427-1430 (2007).
74. T. Kipp, H. Welsch, C. Strelow, C. Heyn, and D. Heitmann, "Optical Modes in Semiconductor Microtube Ring Resonators," Phys. Rev. Lett. **96**, 077403 (2006).
75. F. Xu, V. Pruneri, V. Finazzi, and G. Brambilla, "An embedded optical nanowire loop resonator refractometric sensor," Opt. Express **16**, 1062-1067 (2008).
76. L. Tong, R. R. Gattass, J. B. Ashcom, S. He, J. Lou, M. Shen, I. Maxwell, and E. Mazur, "Subwavelength-diameter silica wires for low-loss optical wave guiding," Nature **426**, 816-819 (2003).
77. F. Xu, and G. Brambilla, "Demonstration of a refractometric sensor based on optical microfiber coil resonator," Appl. Phys. Lett. **92**, 101126 (2008).
78. M. Sumetsky, Y. Dulashko, J. M. Fini, A. Hale, and D. J. DiGiovanni, "The microfiber loop resonator: theory, experiment, and application," J. Lightwave Technol. **24**, 242-250 (2006).
79. X. Jiang, Q. Song, L. Xu, J. Fu, and L. Tong, "Microfiber knot dye laser based on the evanescent-wave-coupled gain," Appl. Phys. Lett. **90**, 233501 (2007).
80. M. Sumetsky, Y. Dulashko, J. M. Fini, and A. Hale, "Optical microfiber loop resonator," Appl. Phys. Lett. **86**, 161108 (2005).
81. F. Xu, and G. Brambilla, "Manufacture of 3-D Microfiber Coil Resonators," IEEE Photon. Technol. Lett. **19**, 1481-1483 (2007).
82. F. Xu, P. Horak, and G. Brambilla, "Optical microfiber coil resonator refractometric sensor," Opt. Express **15**, 7888-7893 (2007).

83. F. Xu, and G. Brambilla, "Embedding optical microfiber coil resonators in teflon," Opt. Lett. **32**, 2164-2166 (2007).
84. G. Vienne, Y. Li, and L. Tong, "Effect of Host Polymer on Microfiber Resonator," IEEE Photon. Technol. Lett. **19**, 1386-1388 (2007).
85. G. Vienne, P. Grelu, X. Pan, Y. Li, and L. Tong, "Theoretical study of microfiber resonator devices exploiting a phase shift," J. Opt. A **10**, 025303 (2008).
86. M. Sumetsky, "Optical fiber microcoil resonator," Opt. Express **12**, 2303-2316 (2004).
87. D. W. Vernooy, V. S. Ilchenko, H. Mabuchi, E. W. Streed, and H. J. Kimble, "High-Q measurements of fused-silica microspheres in the near infrared," Opt. Lett. **23**, 247-249 (1998).
88. M. L. Gorodetsky, A. A. Savchenkov, and V. S. Ilchenko, "Ultimate Q of optical microsphere resonators," Opt. Lett. **21**, 453-455 (1996).
89. J. Stone, "Measurements of the Absorption of Light in Low-Loss Liquids," J. Opt. Soc. Am. **62**, 327-333 (1972).
90. H. Cabrera, A. Marcano, and Y. Castellanos, "Absorption coefficient of nearly transparent liquids measured using thermal lens spectrometry," Condens. Mat. Phys. **9**, 385–389 (2006).
91. R. M. Pope, and E. S. Fry, "Absorption spectrum (380–700 nm) of pure water. II. Integrating cavity measurements," Appl. Opt. **36**, 8710–8723 (1997).
92. S. Lacey, I. M. White, Y. Sun, S. I. Shopova, J. M. Cupps, P. Zhang, and X. Fan, "Versatile opto-fluidic ring resonator lasers with ultra-low threshold," Opt. Express **15**, 15523-15530 (2007).
93. D. K. Armani, T. J. Kippenberg, S. M. Spillane, and K. J. Vahala, "Ultra-high-Q toroid microcavity on a chip," Nature **421**, 925-928 (2003).
94. C. F. Bohren, and D. R. Huffman, *Absorption and Scattering of Light by Small Particles* (John Wiley & Sons, New York, 1998).
95. I. M. White, J. Gohring, Y. Sun, G. Yang, S. Lacey, and X. Fan, "Versatile waveguide-coupled opto-fluidic devices based on liquid core optical ring resonators," Appl. Phys. Lett. **91**, 241104 (2007).
96. I. Teraoka, and S. Arnold, "Coupled whispering gallery modes in a multilayer-coated microsphere," Opt. Lett. **32**, 1147-1149 (2007).
97. H. Kudo, Y. Suzuki, T. Gessei, D. Takahashi, T. Arakawa, and K. Mitsubayashi, "Biochemical gas sensor (bio-sniffer) for ultrahigh-sensitive gaseous formaldehyde monitoring," Biosens. Bioelectron. **26**, 854-858 (2010).
98. J. T. Robinson, L. Chen, and M. Lipson, "On-chip gas detection in silicon optical microcavities," Opt. Express **16**, 4296-4301 (2008).
99. A. M. Ruminski, B. H. King, J. Salonen, J. L. Snyder, and M. J. Sailor, "Porous Silicon-Based Optical Microsensors for Volatile Organic Analytes: Effect of Surface Chemistry on Stability and Specificity," Adv. Funct. Mater. **20**, 2874-2883 (2010).
100. I. Sayago, M. J. Fernández, J. L. Fontecha, M. C. Horrillo, C. Vera, I. Obieta, and I. Bustero, "Surface acoustic wave gas sensors based on polyisobutylene and carbon nanotube composites," Sens. Actuators B **156**, 1-5 (2011).

101. Y. Peng, A.-J. Zhang, M. Dong, and Y.-W. Wang, "A colorimetric and fluorescent chemosensor for the detection of an explosive-2,4,6-trinitrophenol (TNP)," Chem. Commun. **47**, 4505-4507 (2011).
102. J. Jaworski, K. Yokoyama, C. Zueger, W.-J. Chung, S.-W. Lee, and A. Majumdar, "Polydiacetylene Incorporated with Peptide Receptors for the Detection of Trinitrotoluene Explosives," Langmuir **27**, 3180-3187 (2011).
103. F. Warken, E. Vetsch, D. Meschede, M. Sokolowski, and A. Rauschenbeutel, "Ultra-sensitive surface absorption spectroscopy using sub-wavelength diameter optical fibers," Opt. Express **15**, 11952-11958 (2007).
104. V. Joel, and D. Monzón-Hernández, "Fast detection of hydrogen with nano fiber tapers coated with ultra thin palladium layers," Opt. Express **13**, 5087-5092 (2005).
105. W.-C. Lai, S. Chakravarty, X. Wang, C. Lin, and R. T. Chen, "On-chip methane sensing by near-IR absorption signatures in a photonic crystal slot waveguide," Opt. Lett. **36**, 984-986 (2011).
106. L. Kyung Shik, L. Yoon Kyu, and J. Si Hyun, "A Novel Grating Modulation Technique for Photonic Bandgap Fiber Gas Sensors," IEEE Photon. Technol. Lett. **23**, 624-626 (2011).
107. R. C. Carlson, A. F. Hayden, and W. B. Telfair, "Remote observations of effluents from small building smokestacks using FTIR spectroscopy," Appl. Opt. **27**, 4952-4959 (1988).
108. A. Schliesser, M. Brehm, F. Keilmann, and D. van der Weide, "Frequency-comb infrared spectrometer for rapid, remote chemical sensing," Opt. Express **13**, 9029-9038 (2005).
109. M. B. Pushkarsky, I. G. Dunayevskiy, M. Prasanna, A. G. Tsekoun, R. Go, and C. K. N. Patel, "High-sensitivity detection of TNT," Proc. Natl. Acad. Sci. USA **103**, 19630-19634 (2006).
110. C. Ramos, and P. J. Dagdigian, "Detection of vapors of explosives and explosive-related compounds by ultraviolet cavity ringdown spectroscopy," Appl. Opt. **46**, 620-627 (2007).
111. S. Content, W. C. Trogler, and M. J. Sailor, "Detection of Nitrobenzene, DNT, and TNT Vapors by Quenching of Porous Silicon Photoluminescence," Chem. Eur. J. **6**, 2205-2213 (2000).
112. E. D. Lipp, and R. L. Grosse, "On-Line Monitoring of Chlorosilane Streams by Raman Spectroscopy," Appl. Spectrosc. **52**, 42-46 (1998).
113. E. Roth, and W. Kiefer, "Surface-Enhanced Raman Spectroscopy as a Detection Method in Gas Chromatography," Appl. Spectrosc. **48**, 1193-1195 (1994).
114. N. Skivesen, R. Horvath, and H. C. Pedersen, "Multimode reverse-symmetry waveguide sensor for broad-range refractometry," Opt. Lett. **28**, 2473-2475 (2003).
115. Y. L. Hoo, W. Jin, H. L. Ho, D. N. Wang, and R. S. Windeler, "Evanescent-wave gas sensing using microstructure fiber," **41**, 8-9 (2002).
116. C. Elosua, I. Matias, C. Bariain, and F. Arregui, "Volatile Organic Compound Optical Fiber Sensors: A Review," Sensors **6**, 1440-1465 (2006).

117. T. L. Lowder, J. D. Gordon, S. M. Schultz, and R. H. Selfridge, "Volatile organic compound sensing using a surface-relief D-shaped fiber Bragg grating and a polydimethylsiloxane layer," Opt. Lett. **32**, 2523-2525 (2007).
118. T. M. Butler, E. Igata, S. J. Sheard, and N. Blackie, "Integrated optical Bragg-grating-based chemical sensor on a curved input edge waveguide structure," Opt. Lett. **24**, 525-527 (1999).
119. J. Zhang, X. Tang, J. Dong, T. Wei, and H. Xiao, "Zeolite thin film-coated long period fiber grating sensor for measuring trace chemical," Opt. Express **16**, 8317-8323 (2008).
120. A. Cusano, A. Iadicicco, P. Pilla, L. Contessa, S. Campopiano, A. Cutolo, M. Giordano, and G. Guerra, "Coated Long-Period Fiber Gratings as High-Sensitivity Optochemical Sensors," J. Lightwave Technol. **24**, 1776-1786 (2006).
121. T. Wei, Y. Han, Y. Li, H.-L. Tsai, and H. Xiao, "Temperature-insensitive miniaturized fiber inline Fabry-Perot interferometer for highly sensitive refractive index measurement," Opt. Express **16**, 5764-5769 (2008).
122. G. Z. Xiao, A. Adnet, Z. Zhang, F. G. Sun, and C. P. Grover, "Monitoring changes in the refractive index of gases by means of a fiber optic Fabry-Pérot interferometer sensor," Sens. Actuators A **118**, 177-182 (2005).
123. G. H. Cross, Y. Ren, and M. J. Swann, "Refractometric discrimination of void-space filling and swelling during vapour sorption in polymer films," Analyst **125**, 2173–2175 (2000).
124. D. Reichl, R. Krage, C. Krumme, and G. Gauglitz, "Sensing of Volatile Organic Compounds Using a Simplified Reflectometric Interference Spectroscopy Setup," Appl. Spectrosc. **54**, 583-586 (2000).
125. D. Monzón-Hernández, V. P. Minkovich, J. Villatoro, M. P. Kreuzer, and G. Badenes, "Photonic crystal fiber microtaper supporting two selective higher-order modes with high sensitivity to gas molecules," Appl. Phys. Lett. **93**, 081106 (2008).
126. J. Villatoro, M. P. Kreuzer, R. Jha, V. P. Minkovich, V. Finazzi, G. Badenes, and V. Pruneri, "Photonic crystal fiber interferometer for chemical vapor detection with high sensitivity," Opt. Express **17**, 1447-1453 (2009).
127. R. P. Podgorsek, and H. Franke, "Selective optical detection of aromatic vapors," Appl. Opt. **41**, 601-608 (2002).
128. J. M. Bingham, J. N. Anker, L. E. Kreno, and R. P. Van Duyne, "Gas Sensing with High-Resolution Localized Surface Plasmon Resonance Spectroscopy," J. Am. Chem. Soc. **132**, 17358-17359 (2010).
129. Y.-Q. Chen, and C.-J. Lu, "Surface modification on silver nanoparticles for enhancing vapor selectivity of localized surface plasmon resonance sensors," Sens. Actuators B **135**, 492-498 (2009).
130. C.-S. Cheng, Y.-Q. Chen, and C.-J. Lu, "Organic vapour sensing using localized surface plasmon resonance spectrum of metallic nanoparticles self assemble monolayer," Talanta **73**, 358-365 (2007).
131. V. M. N. Passaro, F. Dell'Olio, and F. D. Leonardis, "Ammonia Optical Sensing by Microring Resonators," Sensors **7**, 2741-2749 (2007).

132. S. I. Shopova, I. M. White, Y. Sun, H. Zhu, X. Fan, G. Frye-Mason, A. Thompson, and S.-j. Ja, "On-Column Micro Gas Chromatography Detection with Capillary-Based Optical Ring Resonators," Anal. Chem. **80**, 2232-2238 (2008).
133. Y. Sun, S. I. Shopova, G. Frye-Mason, and X. Fan, "Rapid chemical-vapor sensing using optofluidic ring resonators," Opt. Lett. **33**, 788-790 (2008).
134. Y. Sun, and X. Fan, "Analysis of ring resonators for chemical vapor sensor development," Opt. Express **16**, 10254-10268 (2008).
135. Q. Ma, L. Huang, Z. Guo, and T. Rossman, "Spectral shift response of optical whispering-gallery modes due to water vapor adsorption and desorption," Meas. Sci. Technol. **21**, 115206 (2010).
136. F. Pang, X. Han, F. Chu, J. Geng, H. Cai, R. Qu, and Z. Fang, "Sensitivity to alcohols of a planar waveguide ring resonator fabricated by a sol-gel method," Sens. Actuators B **120**, 610-614 (2007).
137. A. Chen, H. Sun, A. Pyayt, X. Zhang, J. Luo, A. Jen, P. A. Sullivan, S. Elangovan, L. R. Dalton, R. Dinu, D. Jin, and D. Huang, "Chromophore-Containing Polymers for Trace Explosive Sensors," J. Phys. Chem. C **112**, 8072–8078 (2008).
138. R. K. Chang, and A. J. Campillo, *Optical Processes in Microcavities* (World Scientific, Singapore, 1996).
139. J. D. Gordon, T. L. Lowder, R. H. Selfridge, and S. M. Schultz, "Optical D-fiber-based volatile organic compound sensor," Appl. Opt. **46**, 7805-7810 (2007).
140. S. Reidy, G. Lambertus, J. Geece, and R. Sacks, "High-performance, static-coated silicon microfabricated columns for gas chromatography " Anal. Chem. **78**, 2623-2630 (2006).
141. X. Fan, I. M. White, H. Zhu, J. D. Suter, and H. Oveys, "Overview of novel integrated optical ring resonator bio/chemical sensors," Proc. SPIE **6452**, 64520M (2007).
142. I. M. White, and X. Fan, "On the performance quantification of resonant refractive index sensors," Opt. Express **16**, 1020-1028 (2008).
143. N. A. Mortensen, S. Xiao, and J. Pedersen, "Liquid-infiltrated photonic crystals: enhanced light-matter interactions for lab-on-a-chip applications," Microfluid. Nanofluid. **4**, 117-127 (2008).
144. S. Chaure, B. Yang, A. K. Hassan, A. K. Ray, and A. Bolognesi, "Interaction behaviour of spun films of poly[3-(6-methoxyhexyl)thiophene] derivatives with ambient " J. Phys. D **37**, 1558-1562 (2004).
145. J. Jaczewska, I. Raptis, A. Budkowski, D. Goustouridis, J. Raczkowska, M. Sanopoulou, E. Pamula, A. Bernasik, and J. Rysz, "Swelling of poly(3-alkylthiophene) films exposed to solvent vapors and humidity: Evaluation of solubility parameters," Synthetic Met. **157**, 726-732 (2007).
146. H.-J. Moon, G.-W. Park, S.-B. Lee, K. An, and J.-H. Lee, "Waveguide mode lasing via evanescent-wave-coupled gain from a thin cylindrical shell resonator," Appl. Phys. Lett. **84**, 4547-4549 (2004).
147. R. A. Potyrailo, and T. M. Sivavec, "Boosting Sensitivity of Organic Vapor Detection with Silicone Block Polyimide Polymers," Anal. Chem. **76**, 7023-7027 (2004).

148. Z. Liron, N. Kaushansky, G. Frishman, D. Kaplan, and J. Greenblatt, "The Polymer-Coated SAW Sensor as a Gravimetric Sensor," Anal. Chem. **69**, 2848-2854 (1997).
149. H. M. McNair, and J. M. Miller, eds. *Gas chromatography* (Wiley, 2009).
150. G. Lambertus, A. Elstro, K. Sensening, J. Potkay, M. Agah, S. Scheuering, K. Wise, F. Dorman, and R. Sacks, "Design, Fabrication, and Evaluation of Microfabricated Columns for Gas Chromatography," Anal. Chem. **76**, 2629-2637 (2004).
151. C.-J. Lu, J. Whiting, R. D. Sacks, and E. T. Zellers, "Portable Gas Chromatograph with Tunable Retention and Sensor Array Detection for Determination of Complex Vapor Mixtures," Anal. Chem. **75**, 1400-1409 (2003).
152. C.-J. Lu, W. H. Steinecker, W.-C. Tian, M. C. Oborny, J. M. Nichols, M. Agah, J. A. Potkay, H. K. L. Chan, J. Driscoll, R. D. Sacks, K. D. Wise, S. W. Pangad, and E. T. Zellers, "First-generation hybrid MEMS gas chromatograph," Lab Chip **5**, 1123–1131 (2005).
153. Q. Zhong, W. H. Steinecker, and E. T. Zellers, "Characterization of a high-performance portable GC with a chemiresistor array detector," Analyst **134**, 283–293 (2009).
154. E. J. Houser, T. E. Mlsna, V. K. Nguyen, R. Chung, R. L. Mowery, and R. Andrew McGill, "Rational materials design of sorbent coatings for explosives: applications with chemical sensors," Talanta **54**, 469-485 (2001).
155. J. S. Yang, and T. M. Swager, "Fluorescent Porous Polymer Films as TNT Chemosensors: Electronic and Structural Effects," J. Am. Chem. Soc. **120**, 11864-11873 (1998).
156. G. K. Kannan, A. T. Nimal, U. Mittal, R. D. S. Yadava, and J. C. Kapoor, "Adsorption studies of carbowax coated surface acoustic wave (SAW) sensor for 2,4-dinitro toluene (DNT) vapour detection," Sens. Actuators B **101**, 328-334 (2004).
157. S. N. C. Torres, "Improved detection of TNT using SPME-TEEM-GC/MS mode immersion in water and soil," in *Chemistry* (University of Peurto Rico, MAYAGUEZ, 2005).
158. M. V. Putz, and A.-M. Lacrămă, "Introducing Spectral Structure Activity Relationship (S-SAR) Analysis. Application to Ecotoxicology," Int. J. Mol. Sci. **8**, 363-391 (2007).
159. D. R. Lide, *CRC Handbook of Chemistry and Physics* (CRC, Boca Raton, FL, 2008).
160. W. C. Tian, H. K. L. Chan, C.-J. Lu, S. W. Pang, and E. T. Zellers, "Multiple-stage microfabricated preconcentrator-focuser for micro gas chromatography system," J. Microelectromech. S. **14**, 498-507 (2005).
161. G. Lambertus, and R. Sacks, "Stop-Flow Programmable Selectivity with a Dual-Column Ensemble of Microfabricated Etched Silicon Columns and Air as Carrier Gas," Anal. Chem. **77**, 2078-2084 (2005).
162. J. Whiting, and R. Sacks, "Selectivity Enhancement for High-Speed GC Analysis of Volatile Organic Compounds with Portable Instruments Designed for Vacuum-Outlet and Atmospheric-Pressure Inlet Operation Using Air as the Carrier Gas," Anal. Chem. **74**, 246-252 (2002).

163. S. Reidy, D. George, M. Agah, and R. Sacks, "Temperature-Programmed GC Using Silicon Microfabricated Columns with Integrated Heaters and Temperature Sensors," Anal. Chem. **79**, 2911-2917 (2007).
164. S. C. Terry, J. H. Jerman, and J. B. Angell, "A gas chromatographic air analyzer fabricated on a silicon wafer," IEEE Trans. Electron Dev. **26**, 1880-1886 (1979).
165. D. Cruz, J. P. Chang, S. K. Showalter, F. Gelbard, R. P. Manginell, and M. G. Blain, "Microfabricated thermal conductivity detector for the micro-ChemLab(TM)," Sens. Actuators B **121**, 414-422 (2007).
166. P. R. Lewis, P. Manginell, D. R. Adkins, R. J. Kottenstette, D. R. Wheeler, S. S. Sokolowski, D. E. Trudell, J. E. Byrnes, M. Okandan, J. M. Bauer, R. G. Manley, and G. C. Frye-Mason, "Recent advancements in the gas-phase MicroChemLab," IEEE Sens. J. **6**, 784-795 (2006).
167. D. R. Deans, and I. Scott, "Gas chromatographic columns with adjustable separation characteristics," Anal. Chem. **45**, 1137-1141 (2002).
168. J. H. Purnell, and M. H. Wattan, "Separation of aliphatic hydrocarbon mixtures by gas chromatography using serial liquid-phase and solid-phase columns," Anal. Chem. **63**, 1261-1264 (1991).
169. J. R. Jones, and J. H. Purnell, "Prediction of retention times in serially linked open-tubular gas chromatographic columns and optimization of column lengths," Anal. Chem. **62**, 2300-2306 (1990).
170. M. Akard, and R. Sacks, "Pressure-Tunable Selectivity for High-Speed Gas Chromatography," Anal. Chem. **66**, 3036-3041 (2002).
171. T. Veriotti, and R. Sacks, "A Tandem Column Ensemble with an Atmospheric Pressure Junction-Point Vent for High-Speed GC with Selective Control of Peak-Pair Separation," Anal. Chem. **73**, 813-819 (2001).
172. Y. Sun, J. Liu, G. Frye-Mason, S.-j. Ja, A. K. Thompson, and X. Fan, "Optofluidic ring resonator sensors for rapid DNT vapor detection," Analyst **134**, 1386-1391 (2009).
173. M. Loncar, A. Scherer, and Y. Qiu, "Photonic crystal laser sources for chemical detection," Appl. Phys. Lett. **82**, 4648-4650 (2003).
174. Y. Jun, and L. J. Guo, "Optical sensors based on active microcavities," IEEE J. Sel. Top. Quant. Electron. **12**, 143-147 (2006).
175. L. He, S. K. Ozdemir, J. Zhu, W. Kim, and L. Yang, "Detecting single viruses and nanoparticles using whispering gallery microlasers," Nature Nanotechnol. **6**, 428-432 (2011).
176. A. Rose, Z. Zhu, C. F. Madigan, T. M. Swager, and V. Bulovi, "Sensitivity gains in chemosensing by lasing action in organic polymers," Nature **434**, 876-879 (2005).
177. S. Balslev, A. M. Jorgensen, B. Bilenberg, K. B. Mogensen, D. Snakenborg, O. Geschke, J. P. Kutter, and A. Kristensen, "Lab-on-a-chip with integrated optical transducers," Lab Chip **6**, 213-217 (2006).
178. S. Balslev, and A. Kristensen, "Microfluidic single-mode laser using high-order Bragg grating and antiguiding segments," Opt. Express **13**, 344-351 (2005).
179. B. Helbo, A. Kristensen, and A. Menon, "A micro-cavity fluidic dye laser," J. Micromech. Microeng. **13**, 307–311 (2003).

180. J. C. Galas, J. Torres, M. Belotti, Q. Kou, and Y. Chen, "Microfluidic tunable dye laser with integrated mixer and ring resonator," Appl. Phys. Lett. **86**, 264101 (2005).
181. D. V. Vezenov, B. T. Mayers, D. B. Wolfe, and G. M. Whitesidesa, "Integrated fluorescent light source for optofluidic applications," Appl. Phys. Lett. **86**, 041104 (2005).
182. D. V. Vezenov, B. T. Mayers, R. S. Conroy, G. M. Whitesides, P. T. Snee, Y. Chan, D. G. Nocera, and M. G. Bawendi, "A Low-Threshold, High-Efficiency Microfluidic Waveguide Laser " J. Am. Chem. Soc **127**, 8952-8953 (2005).
183. Z. Li, Z. Zhang, T. Emery, A. Scherer, and D. Psaltis, "Single mode optofluidic distributed feedback dye laser," Opt. Express **14**, 696-701 (2006).
184. Q. Kou, I. Yesilyurt, and Y. Chen, "Collinear dual-color laser emission from a microfluidic dye laser," Appl. Phys. Lett. **88**, 091101 (2006).
185. Z. Li, Z. Zhang, A. Scherer, and D. Psaltis, "Mechanically tunable optofluidic distributed feedback dye laser," Opt. Express **14**, 10494-10499 (2006).
186. Y. Cheng, K. Sugioka, and K. Midorikawa, "Microfluidic laser embedded in glass by three-dimensional femtosecond laser microprocessing," Opt. Lett. **29**, 2007-2009 (2004).
187. M. Gersborg-Hansen, and A. Kristensen, "Optofluidic third order distributed feedback dye laser," Appl. Phys. Lett. **89**, 103518 (2006).
188. Z. Li, and D. Psaltis, "Optofluidic Distributed Feedback Dye Lasers," IEEE J. Sel. Top. Quant. Electron. **13**, 185-193 (2007).
189. Y. Chen, Z. Li, Z. Zhang, D. Psaltis, and A. Scherer, "Nanoimprinted circular grating distributed feedback dye laser," Appl. Phys. Lett. **91**, 051109 (2007).
190. G. J. Pendock, H. S. MacKenzie, and F. P. Payne, "Dye lasers using tapered optical fibers," Appl. Opt. **32**, 5236-5242 (1993).
191. H.-M. Tzeng, K. F. Wall, M. B. Long, and R. K. Chang, "Laser emission from individual droplets at wavelengths corresponding to morphology-dependent resonances," Opt. Lett. **9**, 499 - 501 (1984).
192. M. D. Barnes, K. C. Ng, W. B. Whitten, and J. M. Ramsey, "Detection of Single Rhodamine 6G Molecules in Levitated Microdroplets," Anal. Chem. **65**, 2360-2365 (1993).
193. A. S. Kwok, A. Serpenguzel, W.-F. Hsieh, and R. K. Chang, "Two-photon-pumped lasing in microdroplets," Opt. Lett. **17**, 1435 - 1437 (1992).
194. A. S. Kwok, and R. K. Chang, "Stimulated resonance Raman scattering of Rhodamine 6G," Opt. Lett. **18**, 1703 - 1705 (1993).
195. H.-B. Lin, and A. J. Campillo, "cw Nonlinear Optics in Droplet Microcavities Displaying Enhanced Gain," Phys. Rev. Lett. **73**, 2440 - 2443 (1994).
196. J. Feng, G. Shan, B. D. Hammock, and I. M. Kennedy, "Fluorescence quenching competitive immunoassay in micro droplets," Biosens. Bioelectron. **18**, 1055-1063 (2003).
197. A. Sennaroglu, A. Kiraz, M. A. Dündar, A. Kurt, and A. L. Demirel, "Raman lasing near 630 nm from stationary glycerol-water microdroplets on a superhydrophobic surface," Opt. Lett. **32**, 2197-2199 (2007).
198. D. H. Leach, R. K. Chang, and W. P. Acker, "Stimulated anti-Stokes Raman scattering in microdroplets," Opt. Lett. **17**, 387-389 (1992).

199. S. Uetake, R. S. D. Sihombing, and K. Hakuta, "Stimulated Raman scattering of a high-Q liquid-hydrogen droplet in the ultraviolet region," Opt. Lett. **27**, 421-423 (2002).
200. H.-B. Lin, J. D. Eversole, and A. J. Campillo, "Continuous-wave stimulated Raman scattering in microdroplets," Opt. Lett. **17**, 828-830 (1992).
201. H.-B. Lin, A. L. Huston, B. L. Justus, and A. J. Campillo, "Some characteristics of a droplet whispering-gallery-mode laser," Opt. Lett. **11**, 614 - 616 (1986).
202. J. C. Knight, H. S. T. Driver, R. J. Hutcheon, and G. N. Robertson, "Core-resonance capillary-fiber whispering-gallery-mode laser," Opt. Lett. **17**, 1280-1282 (1992).
203. J. C. Knight, H. S. T. Driver, and G. N. Robertson, "Interference modulation of Q values in a cladded-fiber whispering-gallery-mode laser," Opt. Lett. **18**, 1296 - 1298 (1993).
204. H.-J. Moon, Y.-T. Chough, J. B. Kim, K. An, J. Yi, and J. Lee, "Cavity-Q-driven spectral shift in a cylindrical whispering-gallery-mode microcavity laser," Appl. Phys. Lett. **76**, 3679-3681 (2000).
205. M. Cai, O. Painter, and K. J. Vahala, "Observation of Critical Coupling in a Fiber Taper to a Silica-Microsphere Whispering-Gallery Mode System," Phys. Rev. Lett. **85**, 74-77 (2000).
206. V. S. Ilchenko, X. S. Yao, and L. Maleki, "Pigtailing the high-Q microsphere cavity: a simple fiber coupler for optical whispering-gallery modes," Opt. Lett. **24**, 723-725 (1999).
207. R. M. Clegg, A. I. H. Murchie, A. Zechel, and D. M. J. Lilley, "Observing the helical geometry of double-stranded DNA in solution by fluorescence resonance energy transfer " Proc. Natl. Acad. Sci. USA **90**, 2994-2998 (1993).
208. S. Hohng, C. Joo, and T. Ha, "Single-molecule three-color FRET," Biophys. J. **87**, 1328-1337 (2004).
209. E. A. Jares-Erijman, and T. M. Jovin, "Determination of DNA Helical Handedness by Fluorescence Resonance Energy Transfer," J. Mol. Biol. **257**, 597–617 (1996).
210. F. Kukolka, B. K. Müller, S. Paternoster, A. Arndt, C. M. Niemeyer, C. Bräuchle, and D. C. Lamb, "A Single-Molecule Förster Resonance Energy Transfer Analysis of Fluorescent DNA–Protein Conjugates for Nanobiotechnology," Small **2**, 1083-1089 (2006).
211. F. D. Lewis, L. Zhang, and X. Zuo, "Orientation Control of Fluorescence Resonance Energy Transfer Using DNA as a Helical Scaffold," J. Am. Chem. Soc. **127**, 10002-10003 (2005).
212. M. Zuker, "Mfold web server for nucleic acid folding and hybridization prediction," Nucl. Acids Res. **31**, 3406-3415 (2003).
213. H.-J. Moon, Y.-T. Chough, and K. An, "Cylindrical microcavity laser based on the evanescent-wave-coupled gain," Phys. Rev. Lett. **85**, 3161-3164 (2000).
214. R. L. Armstrong, J. G. Xie, T. E. Ruekgauer, and R. G. Pinnick, "Energy-transfer-assisted lasing from microdroplets seeded with fluorescent sol," Opt. Lett. **17**, 943-945 (1992).

215. M. A. Ali, B. Panoutsopoulos, and S. A. Ahmed, "Potential and limitations of energy-transfer processes in pulsed and cw dye laser mixtures: comparison of theory and experiments," Appl. Opt. **31**, 7100-7107 (1992).
216. M. Berggren, A. Dodabalapur, R. E. Slusher, and Z. Bao, "Light amplification in organic thin films using cascade energy transfer," Nature **389**, 466-469 (1997).
217. T. Förster, "Transfer mechanism of electronic excitation," Disc. Faraday Soc. **27**, 7-17 (1959).
218. S. I. Shopova, J. M. Cupps, P. Zhang, E. P. Henderson, S. Lacey, and X. Fan, "Opto-fluidic ring resonator lasers based on highly efficient resonant energy transfer," Opt. Express **15**, 12735-12742 (2007).
219. S. Arnold, and L. M. Folan, "Energy transfer and the photon lifetime within an aerosol particle," Opt. Lett. **14**, 387-389 (1989).
220. P. T. Leung, and K. Young, "Theory of enhanced energy transfer in an aerosol particle," J. Chem. Phys. **89**, 2894-2899 (1988).
221. S. Gotzinger, L. de S. Menezes, A. Mazzei, S. Kuhn, V. Sandoghdar, and O. Benson, "Controlled photon transfer between two individual nanoemitters via shared high-Q modes of a microsphere resonator," Nano Lett. **6**, 1151-1154 (2006).
222. S. Arnold, "Cavity-enhanced fluorescence decay rates from microdroplets," J. Chem. Phys. **106**, 8280-8282 (1997).
223. S. Arnold, S. Holler, and S. D. Druger, "Imaging enhanced energy transfer in a levitated aerosol particle," J. Chem. Phys. **104**, 7741-7748 (1996).
224. Y. Louyer, D. Meschede, and A. Rauschenbeute, "Tunable whispering-gallery-mode resonators for cavity quantum electrodynamics," Phys. Rev. A **72**, 031801(R) (2005).
225. C.-C. Pun, K. Lee, H.-J. Kim, and J. Kim, "Signal amplifying conjugated polymer-based solid-state DNA sensors," Macromolecules **39**, 7461-7463 (2006).
226. N. C. Seeman, "DNA in a material world," Nature **421**, 427-431 (2003).
227. J. Bath, and A. J. Turberfield, "DNA nanomachines," Nature Nanotechnol. **2**, 275-284 (2007).
228. R. P. Goodman, M. Heilemann, S. Doose, C. M. Erben, A. N. Kapanidis, and A. J. Turberfield, "Reconfigurable, braced, three dimensional DNA nanostructures," Nature Nanotechnol. **3**, 93-96 (2008).
229. J. Liu, and Y. Lu, "FRET study of a trifluorophore-labeled DNAzyme," J. Am. Chem. Soc. **124**, 15208-15216 (2002).
230. D. Shu, W.-D. Moll, Z. Deng, C. Mao, and P. Guo, "Bottom-up assembly of RNA arrays and superstructures as potential parts in nanotechnology," Nano Lett. **4**, 1717-1723 (2004).
231. Y. Xu, D. W. Piston, and C. H. Johnson, "A bioluminescence resonance energy transfer (BRET) system: Application to interacting circadian clock proteins," Proc. Natl. Acad. Sci. USA **96**, 151–156 (1999).
232. K. Wang, Z. Tang, C. J. Yang, Youngmi Kim, X. Fang, W. Li, Y. Wu, C. D. Medley, Z. Cao, J. Li, P. Colon, H. Lin, and W. Tan, "Molecular engineering of DNA: Molecular beacons," Angew. Chem. Int. Ed. **47**, 2-17 (2008).

233. A. W. Wun, P. T. Snee, Y. Chan, M. G. Bawendi, and D. G. Nocera, "Non-linear transduction strategies for chemo/biosensing on small length scales," J. Mater. Chem. **15**, 2697–2706 (2005).
234. D. G. Wang, J.-B. Fan, C.-J. Siao, A. Berno, P. Young, R. Sapolsky, G. Ghandour, N. Perkins, E. Winchester, J. Spencer, L. Kruglyak, L. Stein, L. Hsie, T. Topaloglou, E. Hubbell, E. Robinson, M. Mittmann, M. S. Morris, N. Shen, D. Kilburn, J. Rioux, C. Nusbaum, S. Rozen, T. J. Hudson, R. Lipshutz, M. Chee, and E. S. Lander, "Large-Scale Identification, Mapping, and Genotyping of Single-Nucleotide Polymorphisms in the Human Genome," Science **280**, 1077-1082 (1998).
235. P. A. Jones, and S. B. Baylin, "The fundamental role of epigenetic events in cancer," Nature Rev. Genet. **3**, 415-428 (2002).
236. T. K. Christopoulos, "Nucleic Acid Analysis," Anal. Chem. **71**, 425-438 (1999).
237. B. S. Shastry, "Pharmacogenetics and the concept of individualized medicine," Pharmacogenomics J. **6**, 16-21 (2006).
238. L. J. van ’t Veer, and R. Bernards, "Enabling personalized cancer medicine through analysis of gene-expression patterns," Nature **452**, 564-570 (2008).
239. R. D. Hawkins, G. C. Hon, and B. Ren, "Next-generation genomics: an integrative approach," Nature Rev. Genet. **11**, 476-486 (2010).
240. P. A. Jones, and S. B. Baylin, "The fundamental role of epigenetic events in cancer," Nat. Rev. Genet. **3**, 415-428 (2002).
241. X. Liu, W. Farmerie, S. Schuster, and W. Tan, "Molecular beacons for DNA biosensors with micrometer to submicrometer dimensions," Anal. Biochem. **283**, 56-63 (2000).
242. S. Song, Z. Liang, J. Zhang, L. Wang, G. Li, and C. Fan, "Gold-nanoparticle-based multicolor nanobeacons for sequence-specific DNA analysis," Angew. Chem. Int. Edit. **48**, 8670-8674 (2009).
243. A. Hsieh, P. Pan, and A. Lee, "Rapid label-free DNA analysis in picoliter microfluidic droplets using FRET probes," Microfluid. Nanofluid. **6**, 391-401 (2009).
244. C. M. R. López, B. G. Asenjo, A. J. Lloyd, and M. J. Wilkinson, "Direct Detection and Quantification of Methylation in Nucleic Acid Sequences Using High-Resolution Melting Analysis," Anal. Chem. **82**, 9100-9108 (2011).
245. K. Lee, L. K. Povlich, and J. Kim, "Label-free and self-signal amplifying molecular DNA sensors based on bioconjugated polyelectrolytes," Adv. Funct. Mater. **17**, 2580-2587 (2007).
246. G. Bonnet, and A. Libchaber, "Optimal sensitivity in molecular recognition," Physica A **263**, 68-77 (1999).
247. B. Dubertret, M. Calame, and A. J. Libchaber, "Single-mismatch detection using gold-quenched fluorescent oligonucleotides," Nature Biotechnol. **19**, 365-370 (2001).
248. V. M. Baev, T. Latz, and P. E. Toschek, "Laser intracavity absorption spectroscopy," Appl. Phys. B **69**, 171-202 (1999).
249. A. R. Hawkins, and H. Schmidt, eds. *Handbook of Optofluidics* (CRC Press, Boca Raton, 2010).

250. S. Tyagi, and F. R. Kramer, "Molecular beacons: probes that fluoresce upon hybridization," Nature Biotechnol. **14**, 303-308 (1996).
251. G. Bonnet, S. Tyagi, A. Libchaber, and F. R. Kramer, "Thermodynamic basis of the enhanced specificity of structured DNA probes," Proc. Natl Acad. Sci. USA **96**, 6171-6176 (1999).
252. A. Tsourkas, M. A. Behlke, Y. Xu, and G. Bao, "Spectroscopic features of dual fluorescence/luminescence resonance energy-transfer molecular beacons," Anal. Chem. **75**, 3697-3703 (2003).
253. W. Tan, K. Wang, and T. J. Drake, "Molecular beacons," Curr. Opin. Chem. Biol. **8**, 547-553 (2004).
254. A. E. Siegman, *Lasers* (University Science Books, Sausalito, CA, 1986).
255. Y. Sun, S. I. Shopova, C.-S. Wu, S. Arnold, and X. Fan, "Bioinspired optofluidic FRET lasers via DNA scaffolds," Proc. Natl. Acad. Sci. USA **107**, 16039-16042 (2010).
256. W. Lee, Y. Sun, H. Li, K. Reddy, M. Sumetsky, and X. Fan, "A quasi-droplet optofluidic ring resonator laser using a micro-bubble," Appl. Phys. Lett. **99**, 091102 (2011).
257. M. Trupke, E. A. Hinds, S. Eriksson, E. A. Curtis, Z. Moktadir, E. Kukharenka, and M. Kraft, "Microfabricated high-finesse optical cavity with open access and small volume," Appl. Phys. Lett. **87**, 211106 (2005).
258. P. R. Dolan, G. M. Hughes, F. Grazioso, B. R. Patton, and J. M. Smith, "Femtoliter tunable optical cavity arrays," Opt. Lett. **35**, 3556-3558 (2010).
259. S. K. Y. Tang, Z. Li, A. R. Abate, J. A. Agresti, D. Psaltis, D. A. Weitz, and G. M. Whitesides, "A multi-color fast-switching microfluidic droplet dye laser," Lab Chip **9**, 2767 - 2771 (2009).
260. I. M. White, H. Zhu, H. Oveys, and X. Fan, "Bio/chemical sensors based on liquid core optical ring resonator," Proc. SPIE **6223**, 62230F (2006).
261. W. J. Rhee, P. J. Santangelo, H. Jo, and G. Bao, "Target accessibility and signal specificity in live-cell detection of BMP-4 mRNA using molecular beacons," Nucleic Acids Res. **36**, e30 (2008).
262. G. H. Reed, and C. T. Wittwer, "Sensitivity and specificity of single-nucleotide polymorphism scanning by high-resolution melting analysis," Clin. Chem. **50**, 1748-1754 (2004).
263. M. C. Gather, and S. H. Yun, "Single-cell biological lasers," Nature Photon. **5**, 406-410 (2011).
264. M. Sumetsky, Y. Dulashko, and R. S. Windeler, "Optical microbubble resonator," Opt. Lett. **35**, 898-900 (2010).